THE UNIVERSITY OF QUEENSLAND
AUSTRALIA

CREATION AND APPLICATIONS OF LARGE TOROIDAL TIME-AVERAGED OPTICAL POTENTIALS FOR BECS

Jake Andrew Paul Glidden
PhB (Hons) [Science], ANU, 2013

A thesis submitted for the degree of Master of Philosophy at
The University of Queensland in 2017
School of Mathematics and Physics
ARC Centre of Excellence for Engineered Quantum Systems

Abstract

This thesis reports the final stages of construction and performance of a high atom number rubidium-87 Bose-Einstein condensate (BEC) apparatus, and the generation of time-averaged optical potentials geared towards interferometric applications. A detailed description of the hybrid trap used in our experiment is given, which comprises magnetic confinement from a quadrupole field, and optical trapping from a focussed $1064\,\mathrm{nm}$ laser beam. We present the typical temperatures of atom clouds at all stages of cooling, from the 3D magneto-optical trap, through to the onset of condensation in the hybrid trap. Our trap typically realises nearly-pure BECs of 1.5–2.0×10^6 atoms, at temperatures of $(217 \pm 6)\,\mathrm{nK}$, over duty cycles of 16–$25\,\mathrm{s}$.

The implementation of a time-averaged optical potential is also discussed, as a means of generating versatile, planar potentials for BECs. In this work, we focus on the generation of large, ring-shaped potentials, which have trapping frequencies in the ranges $2\pi \times (110$–$140,\, 35$–$55)\,\mathrm{Hz}$ vertically and radially, respectively. The details of a feedforward algorithm are presented, which allows for the realisation of smooth ring structures up to $150\,\mu\mathrm{m}$ in radius, which enclose areas ten times larger than optical ring traps created previously. These larger rings are promising candidates for interferometric measurements of the rotation-induced Sagnac phase, with the device sensitivity proportional to the enclosed area. We typically retain 2.5–3.0×10^6 atoms in these large traps, after evaporatively cooling to temperatures of $(44 \pm 9)\,\mathrm{nK}$. The measured lifetimes in the trap are on the order of $16\,\mathrm{s}$.

These ring condensates are expected to be fully phase coherent, despite their reduced dimensionality, as a result of high atom numbers, weak confinement, and low temperatures. We present preliminary data demonstrating these coherence properties, and outlay future plans for a comprehensive study of this coherence, probing both fully coherent rings, and those expected to fall within the phase-fluctuating regime.

The control afforded using our time-averaged optical potentials is demonstrated through the generation of acoustic waves propagating around the ring condensates. The dispersion is linear for low driving frequencies, and allows for a determination of the speed of

sound, and the chemical potential, found here to be $c_s = 1.34\,\mathrm{mm\,.\,s^{-1}}$, and $\mu = k_B \times 18\,\mathrm{nK}$ respectively.

Declaration by author

This thesis is composed of my original work, and contains no material previously published or written by another person except where due reference has been made in the text. I have clearly stated the contribution by others to jointly-authored works that I have included in my thesis.

I have clearly stated the contribution of others to my thesis as a whole, including statistical assistance, survey design, data analysis, significant technical procedures, professional editorial advice, and any other original research work used or reported in my thesis. The content of my thesis is the result of work I have carried out since the commencement of my research higher degree candidature and does not include a substantial part of work that has been submitted to qualify for the award of any other degree or diploma in any university or other tertiary institution. I have clearly stated which parts of my thesis, if any, have been submitted to qualify for another award.

I acknowledge that an electronic copy of my thesis must be lodged with the University Library and, subject to the policy and procedures of The University of Queensland, the thesis be made available for research and study in accordance with the Copyright Act 1968 unless a period of embargo has been approved by the Dean of the Graduate School.

I acknowledge that copyright of all material contained in my thesis resides with the copyright holder(s) of that material. Where appropriate I have obtained copyright permission from the copyright holder to reproduce material in this thesis.

Jake Andrew Paul Glidden

Publications during candidature

T. A. Bell, J. A. P. Glidden, L. Humbert, M. W. J. Bromley, S. A. Haine, M. J. Davis, T. W. Neely, M. A. Baker, and H. Rubinsztein-Dunlop. Bose-Einstein condensation in large time-averaged optical ring potentials. *New Journal of Physics*, 18(3):035003, 2016.

Publications included in this thesis

No publications included.

Contributions by others to this thesis

The experimental data presented in Figure 5.18 were collected and analysed by Thomas Bell. In addition, a number of CAD renderings of the apparatus shown in chapter 4 were also his work. Appropriate mention has been made in the captions of relevant figures.

Statement of parts of thesis submitted to qualify for the award of another degree

None.

Acknowledgements

There is a long list of people, without whose help I'd not be where I am today. First and foremost, I would like to thank my primary supervisor, Dr Mark Baker. Despite the extra grey hair we've undoubtedly both caused each other, without his knowledge and experience, I would not be submitting this thesis today. Mark, Dr Tyler Neely, and Prof Halina Rubinsztein-Dunlop have collectively been a very supportive and understanding team during my candidacy, in particular while writing up this thesis.

To the other experimentalists in the lab, both on my experiment, and on the other side: Guillaume Gauthier, and Nick McKay Parry - thanks for your input and advice along the way. To Tom Bell, who has spent many a late night fixing electronics, upgrading essential components of the experiment, as well as collecting data in the lab - an enormous thank you for your dedication. It has truly been a huge help in producing this work. I extend my thanks also to Séverin Charpignon, for assistance proofreading, and for making his house available on several occasions, sparing me many a long, late night drive to the outer suburbs.

To the admin staff in the department and in the EQuS office, both past and present, including Danette Peachey, Tara Massingham, Angie Bird, and Ruth Forrest, and the many others I couldn't hope to list in such a small space. You're all amazing! I owe an enormous debt of gratitude to Mr Murray Kane, who is the very definition of going above and beyond. To Dr Marianne Doyle-Pegg, thank you for always having an open door, and for the reminders that sleeping isn't an optional endeavour, but rather a necessity.

To friends both inside and outside physics, you are amazing. The support you've offered has been invaluable when things got tough, or didn't go to plan. In particular to the lovely young grad students in the psychology department - Michelle, Abbey, Ruby, and last, but by no means least, Ms Ashley York. Thanks for making your office mine, and for your moral support. You guys are rock stars, and I couldn't have asked for more supportive friends.

Lastly, to my family. Thank you for relieving the pressure when could over the last few months, and for supporting me throughout.

Keywords

Bose-Einstein condensate, rubidium, time-averaged optical potential, ring trap.

Australian and New Zealand Standard Research Classifications (ANZSRC)

ANZSRC code: 020601, Degenerate Quantum Gases and Atom Optics, 100%

Fields of Research (FoR) Classification

FoR code: 0206, Quantum Physics, 100%

Contents

Chapter 1

Introduction

Interferometry

With the advent of optical interferometric measurement techniques came a number of significant advances in physics. Utilising the coherence offered by photons, physicists have been able to gain insight into a range of phenomena through these highly sensitive techniques. One of the most famous examples is Michelson and Morley's 1887 experiment [2] demonstrating the lack of existence of the so-called luminiferous æther, with more modern examples including the detection schemes employed at the Laser Interferometer Gravitational-Wave Observatory (LIGO) [3], where through use of Michelson-Fabry-Perot interferometers the existence of gravitational waves was recently confirmed [4]. Of particular relevance to this thesis is the Sagnac interferometer first demonstrated by Sagnac himself in his 1913 paper [5], in which he demonstrated a shift in the position of the central maximum of an interference pattern induced by the rotation of the interferometer. Optical Sagnac devices have a sensitivity given by

$$\Delta\varphi = \frac{4\pi}{\lambda\, c}\left(\mathbf{\Omega}\cdot\mathbf{A}\right)\ , \tag{1.1}$$

where $\mathbf{\Omega}$ is the rotation rate, λ is the wavelength of the light used, c is the speed of light in the transport medium, and $\mathbf{A}$ is the area enclosed by the interferometer.

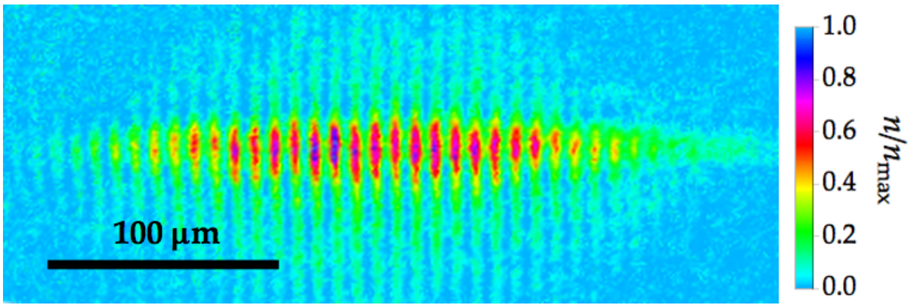

Figure 1.1: An example of matter-wave interference between two Bose-Einstein condensates of ^{87}Rb, created with the apparatus used in this work, in direct analogy with Young's double slit experiment. In the legend label, n denotes the column density (i.e. integrated density along the viewing direction), and n_{max} the peak density.

A renewed interest in interferometry came about in the late 1920s, with the rapid development of quantum mechanics, a significant part of which was de Broglie's theory of wave-particle duality [6]. De Broglie's theory assigns a wavelength $\lambda_{\text{dB}} = h/|\mathbf{p}|$ to a particle carrying momentum $\mathbf{p}$, with particles from electrons through cold atoms and small molecules exhibiting the predicted wave-like behaviour. Planck's constant is denoted here by h. The possibility of interfering cold atoms in particular, potentially offers orders of magnitude improvement in sensitivity over wholly optical devices [7]. This precision comes about from the reduced velocities of cold atoms, $\sim 1\,\text{mm.s}^{-1}$, in comparison with the speed of light, $c = 2.998 \times 10^8\,\text{m.s}^{-1}$. Increased interaction strengths between atoms and electromagnetic and gravitational fields, as opposed to light interacting with these fields, make atomic techniques even more attractive. Early experimental support for de Broglie's predictions of wave-like behaviour followed soon after his original publication, with Davisson and Germer's 1927 electron diffraction experiment [8]. Perhaps the first demonstration of interference due to atomic matter-waves is found in [9], and Figure 1.1 shows a realisation of such interference with our apparatus at The University of Queensland.

Matter-wave interferometers typically rely on free-space interference of freely-expanding

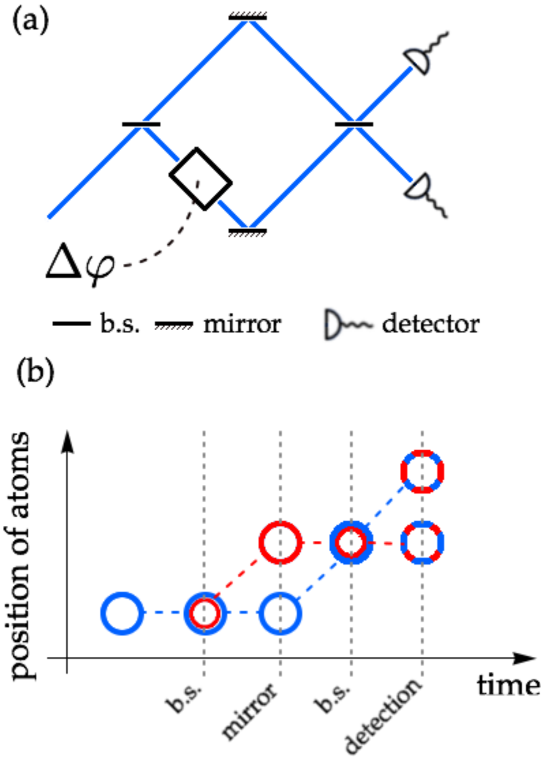

Figure 1.2: Schematic comparison of laser and atom interferometry. (a) Mach-Zehnder interferometer, showing a laser separated into two components using a beam splitter, which traverse the upper and lower arms respectively, before being recombined with another beam splitter. The intensities measured with the detectors at the right are sensitive to the phase difference $\Delta\varphi$ between the upper and lower arms. (b) Mach-Zehnder scheme represented in an atom interferometer. Beam-splitter and mirror operations are produced by interacting the atoms with optical lattices. The relative number of atoms in each of the final clouds (right) is sensitive to the phase difference between interferometer arms.

atom clouds. A classic scheme for these types of devices involves splitting and recombining atom clouds in direct analogy with optical beam-splitters and mirrors. A side-by-side comparison is shown in Figure 1.2, and further detail can be found in [10]. A wide range of matter-wave interferometers have already come into being, with measurements of physical constants including the fine structure constant [11, 12] and Newton's gravitational constant [13], as well as local gravitational and magnetic fields [14–20] having been made. Atomic beam-splitter analogues, namely the interaction of cold atom clouds with optical standing waves, have also been recently realised [21].

State-of-the-art atomic experiments extending Sagnac's 1913 rotation interferometer to matter waves are presently comparable in sensitivity to optical devices [22], but are yet to surpass them. Atomic Sagnac interferometers are realised in schemes similar to Figure 1.2, though the diamond-shaped path is not an essential feature. The sensitivity $\Delta\varphi$ of an atomic Sagnac interferometer is given by

$$\Delta\varphi = \frac{2m}{\hbar}\left(\mathbf{\Omega} \cdot \mathbf{A}\right) \,, \tag{1.2}$$

with m the atomic mass of the species used. The relevant geometrical parameter for Sagnac schemes is therefore the area enclosed between beam-splitter operations, to which the sensitivity is proportional. The state-of-the-art atomic Sagnac experiments see clouds of cold, thermal atoms traverse large rings ($r = 3.1\,\mathrm{mm}$) in opposite directions [22], with the propagation direction playing the role of the interferometer arm. Realising interference with cold, thermal clouds of atoms is no mean feat, but more sensitive atom interferometer measurements are achievable by exploiting the collective coherence of ultracold atomic gases. This is analagous to the use of a laser in place of an incandescent bulb for optical interference. While scalable approaches employing degenerate cold gases have been developed [23–25], these kinds of atom interferometer have been unable to successfully measure a rotation-induced phase, leaving the substantial improvement in sensitivity from Bose-condensed atoms as yet untapped for rotation measurements.

Bose-condensed gases

The coherence of ultra-cold atom clouds arises from the statistical distributions of individual atoms among energy states at low temperatures. The extension of single-particle quantum mechanics to multi-particle systems introduces an inherent division of matter into two classes of particles: bosons, with integer spin; and fermions, with half-integer spin. Bosons and fermions are subject to different distributions at low temperatures. While fermions, with antisymmetric quantum mechanical wavefunctions, are subject to the Pauli exclusion principle, bosons possess symmetric wavefunctions and may simultaneously exist in the same state. Consequently, as collections of bosons cool to near-absolute zero, they mesoscopically occupy the ground state in the formation of what is known as a Bose-Einstein condensate (BEC). The transition from cold gas to BEC is accompanied by a collective coherence of the ensemble, in which the BEC's behaviour is governed by a macroscopic, single-entity quantum mechanical state.

The work of Bose and Einstein [26–28], describing photon and boson statistics respectively, underpins our understanding of the formation of BECs. For a harmonically confined ensemble of N bosons, the transition to condensate is expected to occur when the temperature satisfies $k_B T < N^{1/3}\hbar\omega$, where ω denotes the trapping frequency, with typical transition temperatures for $^{87}\mathrm{Rb}$ of several hundred nanokelvin. Some 70 years after the prediction of the phenomenon, the formation of the first BEC was observed in 1995 [29, 30], with the award of the 2001 Nobel prize to Cornell, Wieman and Ketterle marking the significance of this achievement. Extensive studies of the production of large atom number BECs have since followed [31], where the sensitivity of BEC-based interferometers increases with $\sqrt{N}$. Condensation has even been demonstrated in gases with attractive interactions [32], which had not previously been predicted to occur. Seminal examples of atom interferometry followed soon after the first BEC was produced [33, 34], including Ketterle's two-condensate experiment, followed more recently by a compact realisation on an atom chip [35]. Large-area interferometers with BEC have also been realised [36], with atom interferometer sensitivities to phase shifts scaling linearly with the enclosed area.

BEC-based techniques promise further increases in sensitivity through the use of squeezed states [37], with sophisticated squeezing and recycling techniques theoretically approaching the Heisenberg limit [38]. Squeezed measurements have enabled magnetometry measurements with sensitivities below $50\,\mathrm{pT}$ [39], with much of the credit owing to significant advances in the trapping, cooling and imaging technologies afforded experimentalists in the field.

The high degree of control and flexibility afforded with sophisticated instrumentation allows for BECs to be used as probes in a variety of fields, and they have much overlap with a number of areas of physics. Prime examples include solid-state and condensed-matter physics [40], with a controllable simulator for tight-binding models having been recently demonstrated in BEC [41]. BECs also lend themselves well to studies of superfluidity, including the production of stable vortex trails [42], the systematic identification of an equivalent to the classical Reynolds number [43] in non-viscous media, and the fountain effect [44]. They also exhibit much potential in the area of quantum communication and information, serving as a promising candidate for quantum memories [45] and for gate operations in a quantum computation setting [46–48]. They have recently proven themselves amenable to optimisation through machine-learning algorithms [49], and heightened sensitivities mean BECs are well-suited for standardisation applications, with examples including clock transitions in sodium [50, 51]. Atomtronics is an additional emerging field that takes a modular or component-like approach to BEC technologies, aiming to recreate conventional circuit components in BEC. This includes transistors [52, 53], as well as NIST’s BEC-based superconducting quantum interference device (SQUID) [54–56] as an additional example.

In highlighting these fields, I seek not to provide a comprehensive list, but rather to demonstrate the wide range of applications BEC technologies present. Including this list here aims to demonstrate the capacity of our experiment for future research avenues, as well as motivating the introduction of the time-averaged optical potentials that follows.

1.1 Toroidal traps

The BEC interferometers presented thus far have generally relied upon free-space interference, i.e. collections of trapped atoms are released, and after a period of expansion, they overlap and interfere with one another. Much as the introduction of optical cavities and fibres offered additional control in optical settings, BEC interferometry would benefit

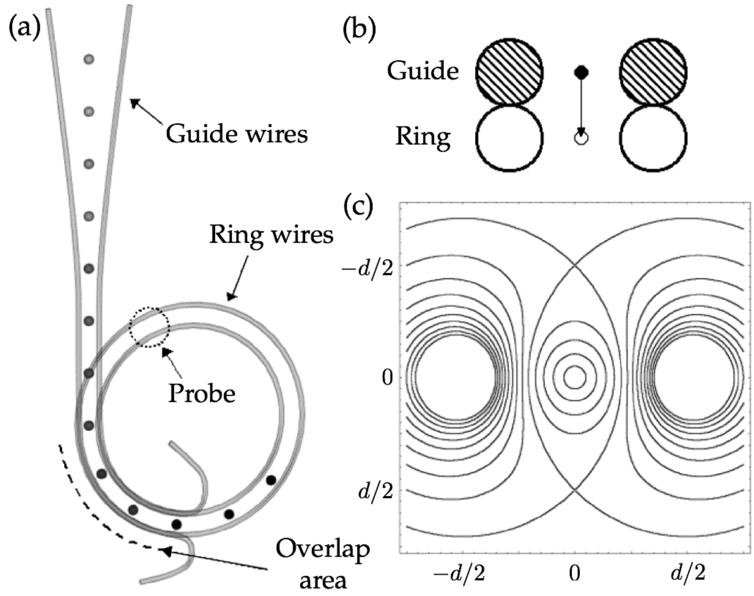

Figure 1.3: A schematic representation of the cold atom storage ring used in the Chapman group. (a) Schematic representation of the ring geometry. The guide wires provide a connection between a cold magneto-optical trap (MOT) at $57\,\mu\mathrm{K}$ and the storage ring. (b) The overlap region at the bottom-left shown as a cross-section. By varying the guide and ring currents, the trap minimum is shifted from between the guide wires (black, shaded) to the ring (open circles). (c) $0.5\,\mathrm{mK}$ contours of the two-wire potential for $d = 0.84\,\mathrm{mm}$ and $I = 8\,\mathrm{A}$. Figure reproduced from [57].

further from the creation of stable atomic waveguides. Within the scope of this thesis, we restrict ourselves to the formation of 3D harmonic, and toroidal geometries, primarily for their direct applications in Sagnac interferometry.

1.1.1 Magnetically-confined toroidal traps

There is no shortage of examples of ring traps for neutral, ultracold atoms formed in the past two decades. Early examples rely on magnetic trapping [58, 59] and radio frequency (RF) dressed fields [60], including the 'storage ring' from the Chapman group [57], shown schematically in Figure 1.3. A large, $2\,\mathrm{cm}$ diameter ring provides magnetic confinement for up to 10^6 atoms of ^{87}Rb. Two concentric circular wires provide a two-dimensional quadrupole field that confines atoms of mean velocities of $1\,\mathrm{m\,.\,s^{-1}}$, or energies of $\sim 100\,\mathrm{neV}$, for several hundred milliseconds.

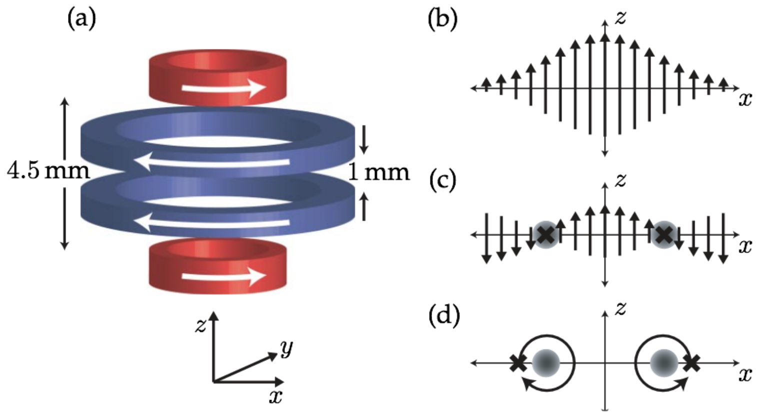

Figure 1.4: Time-orbiting ring trap (TORT) geometry used in the Stamper-Kurn group. (a) Four-coil arrangement used to generate the trap. (b) The field produced by the red (outer, small) coils, providing the required field curvature. (c) Applying a uniform bias with the blue (inner, large) coils creates a ring of zeros (marked ×) in the horizontal plane, at which atoms are trapped. (d) Additional rapid rotation of the field zeros as shown overcomes the effect of Majorana loss. Figure reproduced from [62].

The Prentiss group at Harvard demonstrated the combination of atom diffraction from optical standing waves with propagation in a stadium-shaped magnetic waveguide [61]. Their arrangement encloses an area of $10.9\,\mathrm{cm}^2$ and boasts atomic flux densities of more than $1.0 \times 10^{11}\,\mathrm{atoms\,.\,s^{-1}\,.\,cm^{-2}}$.

The extension of these traps to BEC is demonstrated in [62], in which a time-averaged quadrupole ring is created. The geometry of this arrangement is shown in Figure 1.4. Simple electromagnetic coils provide a magnetic field in which the field orientation reverses at radii ranging from 0.6–$1.5\,\mathrm{mm}$ from the coil axis. Weak-field seeking ^{87}Rb atoms collect around the field zero. Magnetically-sensitive atoms pooling at a sign-change, however, experience large Majorana losses due to spin flips. To overcome this, the zero location is rapidly rotated around the atoms' location to produce a time-orbiting ring trap.

Ryu et al. have demonstrated the formation of a BEC of sodium atoms in a magnetic trap, whose Majorana losses are mitigated through 'plugging' the field zero with a repulsive blue-detuned beam [63]. This experiment further demonstrates an application of ring traps with BEC to studies of superfluidity. Orbital angular momentum is transferred to

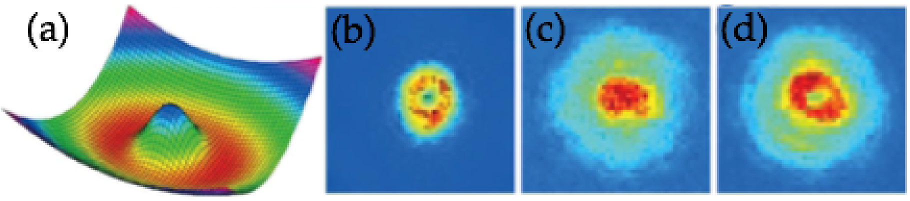

Figure 1.5: Ryu et al.'s 'plugged' magnetic trap. (a) Trap geometry, showing harmonic confinement provided by the magnetic field and a repulsive barrier in the centre, which repels the atoms from the magnetic field zero. (b) In-situ image of atoms within the ring trap. (c) Free space time-of-flight expansion of a non-rotating ring, showing a density peak in the centre. (d) Time-of-flight expansion of a ring with $\hbar$ orbital angular momentum, showing a zero in the density at the centre. This arises from the requirement that the phase be well defined at all positions. Figure reproduced from [63].

the ring condensate from a Laguerre-Gauss (LG) beam, transferring one quantum $\hbar$ from the light field to each atom. This resulted in the observation of persistent flow for up to 10 s, as evidenced by a persistent hole at the centre of the ring in time-of-flight expansion as in Figure 1.5.

1.1.2 Optically-confined toroidal traps

While the traps addressed above offer a high degree of control via precision electronics and coil geometry, they are also restrictive in their reliance upon magnetic interactions to provide confinement. Employing optical potentials instead offers a a magnetically insensitive alternative, which frees the atoms' angular momentum state as an internal degree of freedom. This has advantages for guided interferometry, as transitioning atoms between angular momentum states can be exploited to address different portions of the condensate independently. Similarly, by transferring atoms to a magnetically insensitive hyperfine state via, e.g. RF transitions, the effects of uncompensated DC and AC magnetic fields can be avoided.

An early example of an all-optical ring trap for atoms is Ramanathan et al.'s optical trap [64], created in 2010. An attractive potential is created at the intersection of red-detuned,

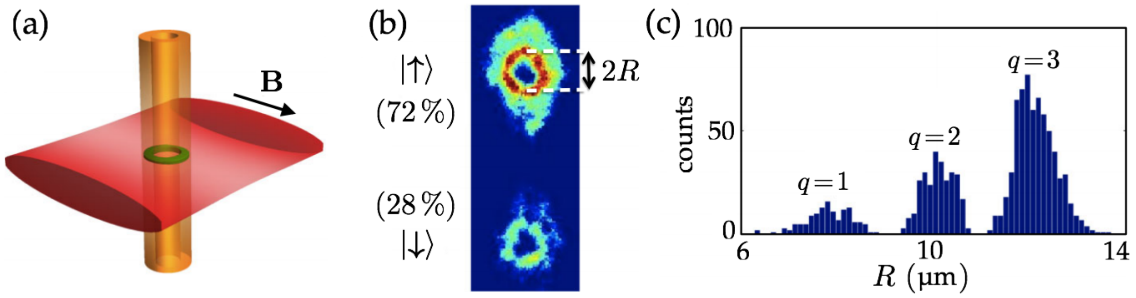

Figure 1.6: All-optical ring trap used in the Hadzibabic group, for detecting persistent currents in BEC. As an all-optical geometry, this trap allows for studying of spinor BECs. (a) Geometry of set up, showing a sheet beam and intersecting Laguerre-Gauss beam. The $\mathbf{B}$ field shown is the externally applied field. (b) Spin state populations measured using absorption imaging, after Stern-Gerlach separation. The radius R is used as a measure of the circulation. (c) Distribution of measured radii for varying degrees of spin polarisation and hold time. The three distinct peaks clearly show the quantised circulation. Figure adapted from [67].

$1030\,\mathrm{nm}$ 'sheet' and 'ring' beams. The sheet beam propagates horizontally, has cross-sectional waists $9\,\mu\mathrm{m}$ (v) and $400\,\mu\mathrm{m}$ (h), and provides confinement against gravity. The vertically propagating ring beam is Laguerre-Gaussian, as in [65], and confines the condensate to a $\sim 20\,\mu\mathrm{m}$ radius ring. Copropagating LG and Gaussian beams in two-photon resonance with the $|1,-1\rangle \rightarrow |1,0\rangle$ transition transfer angular momentum [66], and result in a long-lived ($\approx 40\,\mathrm{s}$) persistent current. In 2012-13, the Hadzibabic group employed a similar geometry, also to study persistent currents [67], but also observing a dependence of the supercurrent stability on the magnitude of the spin-polarisation vector. For highly imbalanced spin populations, persistent flow for up to $2\,\mathrm{min}$ was observed in rings of radius $12\,\mu\mathrm{m}$. Figure 1.6 shows the geometry, and a selection of measurement results from this experiment.

Optical ring traps are not restricted to studies of persistent currents, but lend themselves well to a host of additional experiments. One such example is the 2014 observation of resistive flow in BEC as a repulsive barrier is dragged through the condensate [68]. As in [64], the ring is $\sim 20\,\mu\mathrm{m}$ in radius, and the transition from superfluid flow to resistive flow with a change in barrier speed is characterised. A similar trap has since been used as an early foray into the field of atomtronics, with the creation of a cold-atom SQUID and Josephson junction analogue [69–72], and measurements of the phonon excitation spectra

[54]. Such devices are promising candidates for magnetometry and rotation sensing.

I will take this opportunity to reflect on the sizes of the rings generated in experiments to date. While earlier magnetic geometries offered larger rings of several millimetre in diameter, they were restricted to the use of thermal atoms, or to single spin states. Optically-formed rings with BECs have traditionally been much smaller, from the Boshier group's 10 µm radius rings [73], through the Hadzibabic group's 12–14 µm radius [67], and finally to NIST's 20 µm radius ring [64]. Introducing an optical feedforward technique was shown to increase accessible radii to 44 µm in [74]. Extensions of the feedforward technique allow us to demonstrate much larger, smooth optical traps of radii up to 150 µm in this thesis.

1.2 Time-averaged optical potentials

While optical potentials are advantageous in that they allow for trapping of different magnetic states, they have suffered historically from restricted sizes. Without the ability to modulate the intensity of static beams spatially, ring geometries have been restricted to regions in confining sheets (see § 1.1.2) in which variations in the optical potential of the sheet are minimal in comparison with the chemical potential. As seen in the above examples, this typically limits rings to radii of $\sim 20\,\mu\text{m}$.

In [73, 74], an alternative means of producing optical potentials for trapping neutral atoms, and indeed BECs, is proposed. Through the use of a two-dimensional acousto-optical modulator (2D-AOM), the location of the focus of a vertically-propagating, far off-resonant beam is controlled, as shown in Figure 1.7. By scanning the beam at a timescale faster than the trapped atoms are able to respond, a time-averaged potential is created. Such potentials offer both dynamic and spatial control over the

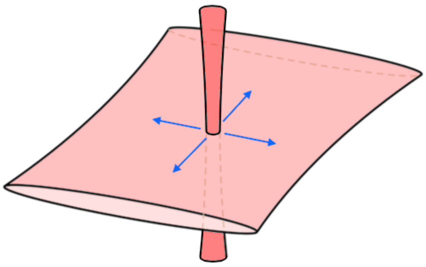

Figure 1.7: One possible geometry that can be used for generating time-averaged optical potentials. The vertically propagating beam is steerable through the use of a 2D-AOM, and rapid scanning of the beam allows for the generation of nearly-arbitrary planar potentials for BECs. Figure adapted from [75].

depth of the potential through tuning the amplitude of the RF input into the 2D-AOM. This enables the production of much larger all-optical ring traps. [74] reports control over potentials with radii of 44 µm, using a feedforward technique to flatten the measured optical intensity. In this thesis, we extend the feedforward principle to the atoms' spatial distribution directly. We note the significant improvements achievable using the atom density as a signal, and are able to generate smooth ring potentials of radii as large as 150 µm.

These techniques are now used in several laboratories, including in the Boshier (Los Alamos) [73] and Kjærgaard (Otago) groups [76]. One scheme at use in Otago is shown in Figure 1.8, illustrating the level of control and precision afforded, with little-to-no atom loss or heating induced in a dynamic, spatially addressable scheme for splitting cold atom clouds. [73] details the production of ring traps similar in size to the static traps of [67, 68], as well as lattices, both rectangular [77] and on a torus [78].

1.3 Motivation

The rich and diverse range of experiments addressed here, in combination with the geometries and precision control afforded by the techniques described, form the basis for the motivation behind the work presented in this thesis. The experiment demonstrates the production of large, smooth, all-optical potentials for BECs with low variations in the atomic density. Using these traps, we are able to access a parameter space previously restricted to magnetically confined atom clouds, with promising potential as a candidate for atomic Sagnac measurements, and with views initially towards studies of superfluidity. We confirm that atoms in the trap are indeed Bose condensed, and furthermore make preliminary measurements demonstrating their phase coherence, demonstrating their capacity for guided interferometric measurements.

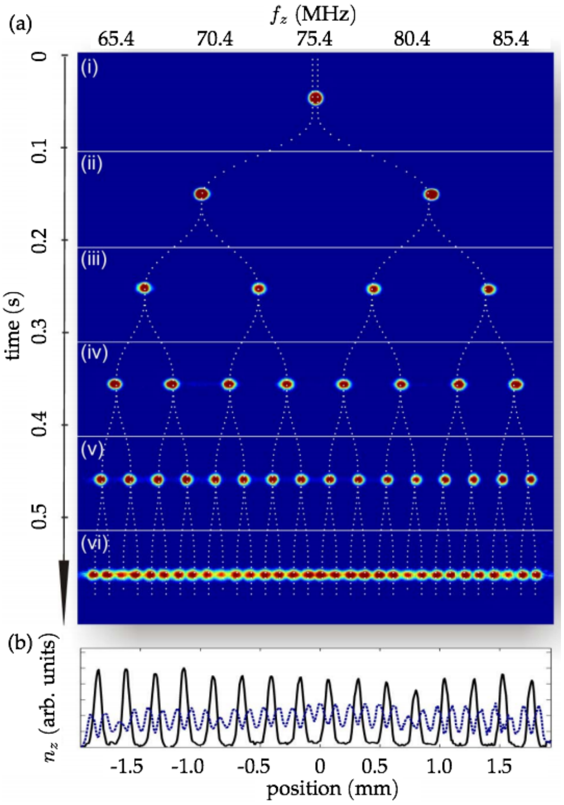

Figure 1.8: An implementation of a time-averaged optical potential at Otago, showing the uniform splitting of a cold cloud of ^{87}Rb into 32 smaller samples. A 1064 nm fibre laser is scanned at a hopping rate of 320 kHz between two closely-spaced frequencies, with the difference in frequencies increasing in time. This process is repeated through 5 iterations to give the patterns shown in (a). (b) depicts the atomic density profile in frames (v, black) and (vi, blue, dashed) of the above image. Figure reproduced from [76].

Thesis outline

Chapter 2 of this thesis presents the theory underpinning interactions between atoms, and electric and magnetic fields, and develops this into the production of time-averaged optical potentials. In chapter 3, we address the fundamental mechanism behind forming a Bose-Einstein condensate, and explore the concept of phase coherence in the context of interferometer. Chapter 4 describes our BEC apparatus, with an emphasis on our method for generating confining potentials. In chapter 5, we present the main results of this thesis, demonstrating our ability to create large ring structures, among other potentials. These are geared towards the creation of atomic waveguides for use in atom interferometry, as well as creating large, smooth traps for studies of superfluidity. As our first production of a BEC occurred during my candidacy, the characterisation of the condensate and relevant traps will also be covered in chapter 5. Chapter 6 discusses the future directions of the experiment, and summarises the contents of the thesis.

Chapter 2

Cooling and trapping of neutral atoms

Significant advances in magnetic and optical techniques for cooling and trapping atoms have played a key role in realising the phenomenon of Bose-Einstein condensation. A range of techniques and geometries have been employed historically, including Doppler cooling, optical molasses, magnetic traps of varying geometry, and optical dipole traps. In this chapter, a theoretical description of the interactions between light, magnetic fields and neutral atoms is presented, developing into techniques for cooling, trapping and evaporating atom clouds. The relevant atomic properties of rubidium-87, the species used in this work, are also included here. Finally, the trapping geometries relevant to the apparatus will be discussed, along with absorption imaging as a technique for detecting atoms.

2.1 Rubidium-87

In what follows, it will be sufficient to treat the atom as a two-level quantum system. Evidently, this approximation does not apply for a general neutral atom, which posseses a considerably more complex level structure. For the group IA elements, known as the alkali metals, however, this approximation is valid. Possessing a single valence electron, the alkali metals permit accurate calculations of their electronic energy levels via perturbative means. In ^{87}Rb in particular, a nearly-closed transition exists between the $5^2\ S_{1/2}$ and $5^2\ P_{3/2}$ states, for which the two-level approximation applies. The structure of this

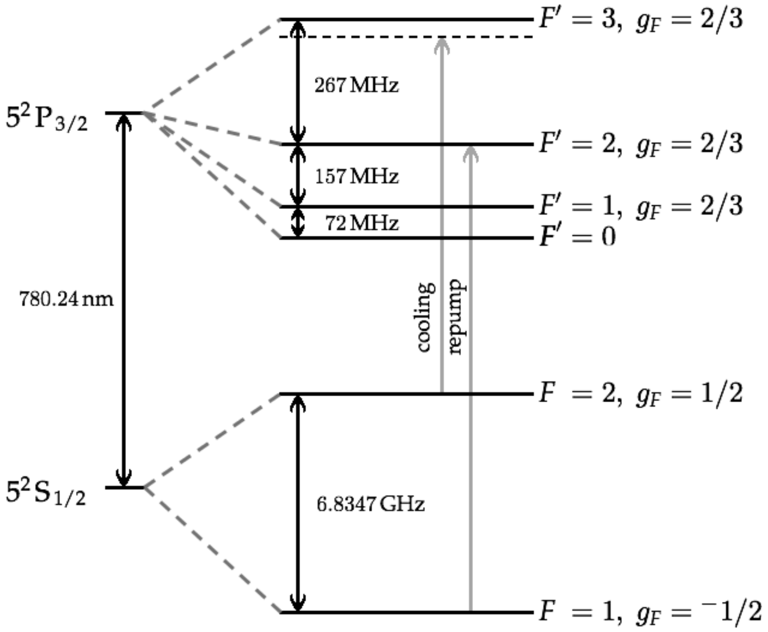

Figure 2.1: Hyperfine structure of the ^{87}Rb D2 line. Levels are labelled with their total angular momentum, F. The relevant transition for cooling is labelled, along with the repump transition, which recylces atoms from the dark $F = 1$ ground state. Dashed, horizontal lines are used to denote detunings of the lasers from resonant peaks. Level spacings are not to scale. Image adapted from [79].

transition, generally referred to as the D2 line, is shown in Figure 2.1.

2.2 Atom-light interactions

Our experiment relies on the interactions between rubidium atoms and laser light, for the purposes of cooling, trapping and imaging. Electrically-neutral atoms exhibit two primary interactions with light, namely the dissipative scattering, and conservative dipole interactions. Non-conservative scattering forces are used in laser cooling, in optical molasses and magneto-optical traps, with this type of interaction dominant for small laser detunings from an atomic resonance. Dipole interactions, in contrast, are conservative, reliant instead upon the interaction of the light-induced dipole moment of an atom with the light field itself. Dipole interactions become dominant for far-detuned laser frequencies. We employ 780 and 1064 nm lasers (and derivatives thereof) for cooling and generating confining potentials respetively, which are detuned from the D2 resonance of ^{87}Rb. Both scattering and dipole interactions play a significant role in the production of condensates in our experiment, and as such are discussed briefly here. More detailed discussions of both forces may be found in [80, 81].

In the presence of an external electric field $\mathbf{E}$, an electric dipole moment $\mathbf{p}$ may be induced in an atom. In the case of weak to moderate electric fields, the expectation value of the dipole moment is linear in the field,

$$\langle \mathbf{p} \rangle = \alpha(\omega)\mathbf{E} \ , \tag{2.1}$$

where $\alpha(\omega)$ denotes the atomic polarisability as a function of the radiation frequency ω. The polarisability is, in general, a function mapping to the complex plane. The real part corresponds to conservative dipole interactions, and the imaginary component describes absorption and emission of photons, giving rise to the scattering forces. It is within the functional form of the polarisability that our understanding of atom-light interactions is contained, and so we seek to obtain an expression for α in terms of the physical properties of the trapped atom, and the confining laser.

Employing a semi-classical ansatz sometimes referred to as the oscillator model as, for example, in [82], we represent the laser field as a classical plane wave, and describe the atom as a quantum mechanical two-level system. In what follows, we only consider the interactions between a single atom and the light field. The field takes the form $\mathbf{E}(t) = \mathbf{E}_0 \cos(\omega t)$. We take a perturbative approach, constructing the atomic wavefunction Ψ as a superposition of the unperturbed ground and excited states, $\psi_g(\mathbf{r}, t)$ and $\psi_e(\mathbf{r}, t)$, with coefficients c_g and c_e respectively, i.e.

$$\Psi(\mathbf{r}, t) = c_g(t)\psi_g(\mathbf{r}, t) + c_e(t)\psi_e(\mathbf{r}, t) \ . \tag{2.2}$$

The coefficients $c_{g,e}$ satisfy the standard normalisation condition

$$|c_g(t)|^2 + |c_e(t)|^2 = 1 \ , \tag{2.3}$$

and each term individually gives the occupancy of the corresponding state. The interaction is described by the Hamiltonian

$$\hat{\mathcal{H}}_{\text{int}} = -\mathbf{p} \cdot \mathbf{E} \; , \tag{2.4}$$

and we isolate the temporal and spatial dependence of $\psi_{g,e}$ through separation of variables. With E_g (E_e) denoting the unperturbed energy of the ground (excited) state, evolving (2.2) under (2.4) gives the time evolution of the coefficients as the coupled differential equations

$$\begin{aligned} -i\hbar\tfrac{\partial}{\partial t}c_g &= c_e \mathbf{p}_{eg} \cdot \mathbf{E}_0 \cos(\omega t) \exp\left(-\tfrac{i}{\hbar}(E_e - E_g)t\right) \; , \text{ and} && (2.5) \\ -i\hbar\tfrac{\partial}{\partial t}c_e &= c_g \mathbf{p}_{ge} \cdot \mathbf{E}_0 \cos(\omega t) \exp\left(+\tfrac{i}{\hbar}(E_e - E_g)t\right) \; . && (2.6) \end{aligned}$$

The matrix elements $\mathbf{p}_{ge} = \langle g|\mathbf{p}|e\rangle$ and $\mathbf{p}_{eg} = \mathbf{p}_{ge}^{\dagger}$ describe the coupling between the ground and excited states induced by the external field. These elements govern the rate of exchange between the two states, and are typically expressed via the Rabi frequency, $\Omega = |\mathbf{p}_{ge} \cdot \mathbf{E}|/\hbar$.

While these expressions capture the stimulated processes of photon absorption and emission, the spontaneous decay due to the natural line width of the state is not encompassed by these equations of motion. This decay tends to deplete the excited state, and may be thought of in terms of classical radiative energy loss as described in [81]. The damping rate at driving frequency ω is given by

$$\begin{aligned} \Gamma_\omega &= \left(\frac{\omega}{\omega_0}\right)^2 \Gamma, \quad \text{where} && (2.7) \\ \Gamma &\equiv \frac{\omega_0^3}{3\pi\epsilon_0\hbar c^3} |\langle e|\mathbf{p}|g\rangle|^2 && (2.8) \end{aligned}$$

is the resonant or natural line width of the excited state, when driven at $\omega_0 = (E_e - E_g)/\hbar$. This results in a decay with lifetime $2/\Gamma_\omega$, or equivalently adds an imaginary contribution to the energy of $-i\hbar\Gamma_\omega/2$. Including this contribution, and transforming to the more convenient variables introduced above, equations (2.5) and (2.6) become

$$\begin{aligned} \tfrac{\partial}{\partial t}c_g &= ic_e\Omega\cos(\omega t)e^{-i\omega_0 t} + \tfrac{\Gamma_\omega}{2}c_e \;, && (2.9)\\ \tfrac{\partial}{\partial t}c_e &= ic_g\Omega\cos(\omega t)e^{+i\omega_0 t} - \tfrac{\Gamma_\omega}{2}c_e \;. && (2.10) \end{aligned}$$

The addition of the decay term leads to the existence of a steady-state solution, in which

$$\tfrac{\partial}{\partial t}|c_{g,e}|^2 = 0 \;, \tag{2.11}$$

i.e. the occupancy of both ground and excited states is unchanging. Solving for this condition, and combining the solution with the definition (2.1), we obtain the final expression for the polarisability

$$\alpha(\omega) = 6\pi\epsilon_0 c^3 \frac{\Gamma}{\omega_0^2[\omega_0^2 - \omega^2 - i(\omega/\omega_0)^3\Gamma\omega_0]} \;. \tag{2.12}$$

We note that this perturbative approach is valid only provided the perturbative energy is much less than the decay term, i.e. the Rabi frequency $\Omega^2 \ll (\delta^2 + \Gamma^2/4)^{1/2}$. This condition is satisfied in most experimental arrangements, and is indeed the case for the experimental scenarios described within this thesis.

2.2.1 Scattering forces

As mentioned earlier, the scattering forces are encompassed in the imaginary component of the polarisability. In particular, the scattering force is given by

$$\mathbf{F}_{\text{sc}} = \hbar\mathbf{k}\Gamma_{\text{sc}} \;, \tag{2.13}$$

where **k** is the photon wave vector, and, when illuminating the atom with light of intensity $I(\mathbf{r})$,

$$\Gamma_{\text{sc}}(\mathbf{r}) = \frac{1}{\hbar\epsilon_0 c}\text{Im}(\alpha)I(\mathbf{r}) \;. \tag{2.14}$$

Evaluating the imaginary component of α, we find:

$$\mathrm{Im}(\alpha) = \frac{6\pi c^3 \epsilon_0}{\omega_0} \left(\frac{\omega}{\omega_0}\right)^3 \frac{\Gamma^2}{\left((\omega_0^2 - \omega^2)^2 + \Gamma^2 \omega_0^2 \left(\frac{\omega}{\omega_0}\right)^6\right)} \,. \tag{2.15}$$

In many experimental settings, the laser frequency is suitably far detuned from the resonance that the final term in the denominator may be neglected. In this case, the scattering rate takes on the somewhat friendlier form

$$\Gamma_{\text{sc}}(\mathbf{r}) = \frac{3\pi c^2}{2\hbar\omega_0^3} \left(\frac{\omega}{\omega_0}\right)^3 \left(\frac{\Gamma}{\omega_0 - \omega} + \frac{\Gamma}{\omega_0 + \omega}\right)^2 I(\mathbf{r}) \,. \tag{2.16}$$

Nearer an atomic resonance, this final term in the denominator cannot be neglected. In fact, an additional term also arises due to the non-zero interaction time, which causes a saturation effect. For sufficiently large light intensities, the excited state population saturates. Defining the *saturation intensity*

$$I_{\text{sat}} = \frac{\hbar\omega_0^3 \Gamma}{12\pi^2 c^2} \,, \tag{2.17}$$

the near-resonant scattering rate takes the form

$$\Gamma_{\text{sc}}(\mathbf{r}) = \frac{\Gamma}{2} \frac{I/I_{\text{sat}}}{1 + I/I_{\text{sat}} + (2\Delta/\Gamma)^2} \,, \tag{2.18}$$

where we have defined $\Delta = \omega - \omega_0$ as the detuning of the laser field from resonance.

2.2.2 Optical molasses

Atoms within a near-resonant laser beam undergo continuous absorption and spontaneous re-emission of photons. The spontaneous decay back to the ground state is, on average, isotropic, however the absorption process always results in a transfer of momentum to the atom along the beam propagation direction. The net force over a large number of absorption-emission cycles is therefore along the propagation direction of the laser. This can be used to slow atoms moving against the beam [83, 84].

This simplified scenario, however, does not of itself provide a protocol for cooling atoms. The force is not selective on the atom's velocity, and so would also accelerate slow-moving atoms along the direction of the beam, causing heating instead. For a genuine cooling effect, a dissipative interaction dependant on the atom's velocity is required. Modifying the effective frequency of the laser to account for the Doppler shift experienced by the atoms yields a net damping force. This fact is exploited in the creation of an optical molasses, the topic of this section, and forms an integral part of magneto-optical traps, which will be addressed in § 2.3.2.

When first trying to create optical configurations for cooling and trapping atoms using the dissipative scattering forces, a number of obstacles were encountered. The interested reader is directed to [85] for a detailed discussion of these factors. Primarily, however, the geometries within which cooling and confinement can occur are restricted by an optical equivalent of the Earnshaw theorem. The most commonly used geometry that does provide an overall cooling effect comprises three pairs of counterpropagating laser beams, of pairwise orthogonal polarisations, so as to prevent interference effects. These polarisations can be simply achieved by retro-reflecting the beams, incorporating a waveplate to rotate the polarisation appropriately. The laser beams in an optical molasses are of a frequency slightly lower than the atomic transition, a condition generally termed *red-detuned*.

We can restrict out attention to the one-dimensional case, with two counter-propagating beams of orthogonal polarisation, in order to gain an understanding of the mechanism applied in an optical molasses. An atom moving along (or against) the direction of propagation of a laser perceives a Doppler shift in the laser frequency of

$$\delta_{\mathrm{Doppler}} = -\mathbf{k} \cdot \mathbf{v} \,, \tag{2.19}$$

where $\mathbf{v}$ is the atom's velocity, and $\mathbf{k}$ is the photon wave vector, which points along the laser's propagation direction. Atoms moving in the propagation direction therefore perceive a lower, or *redder* frequency, than if they had been stationary, while atoms moving against or into the beam perceive a higher, or *bluer* frequency. Atoms in an overall red-shifted beam will therefore scatter more often when moving *against* a beam, as compared with an atom moving *along* the beam, as motion into the beam brings the light's frequency closer to resonance with the atomic transition.

In what follows, we define the positive direction as the direction of the atom's velocity. Combining (2.13) and (2.18), and summing the contributions to the total molasses force F_{mol} for each of the two beams, we have

$$\begin{aligned} F_{\text{mol}} &= F_- + F_+ \, , \\ &= -\hbar k \frac{\Gamma}{2} \left[\frac{1}{1 + I/I_{\text{sat}} + (2(\Delta + kv_{\|})/\Gamma)^2} \right. \\ &\qquad \left. - \frac{1}{1 + I/I_{\text{sat}} + (2(\Delta - kv_{\|})/\Gamma)^2} \right] \frac{I}{I_{\text{sat}}} \, . \end{aligned} \tag{2.20}$$

Here we have replaced Δ in each term with $(\Delta \pm kv_{\|})$ in accordance with (2.19). In most experimental settings, including ours, the molasses lasers have relatively small detunings from the transitions, and the Doppler shifts are smaller again, i.e. $|kv_{\|}| \ll |\Delta| \ll \omega_0$. This allows us to treate the above expression approximately, and simplify it further. Using a binomial expansion for the Doppler shift, we find

$$\begin{aligned} F_{\text{mol}} &= -\hbar k \frac{\Gamma}{2} \left[\frac{1}{1 + I/I_{\text{sat}} + (2\Delta/\Gamma)^2 (1 + 2kv_{\|}/\Delta + \dots)} \right. \\ &\qquad \left. - \frac{1}{1 + I/I_{\text{sat}} + (2\Delta/\Gamma)^2 (1 - 2kv_{\|}/\Delta + \dots)} \right] \frac{I}{I_{\text{sat}}} \, , \end{aligned} \tag{2.21}$$

and once again yields, finally,

$$\begin{aligned}F_{\text{mol}} &= -\hbar k\frac{\Gamma}{2}\left[\frac{1}{1+I/I_{\text{sat}}+(2\Delta/\Gamma)^2}\left(1-\frac{4\Delta^2}{\Gamma^2}\frac{2kv_{\parallel}/\Delta}{1+I/I_{\text{sat}}+(2\Delta/\Gamma)^2}+\ldots\right)\right.\\ &\qquad \left.-\frac{1}{1+I/I_{\text{sat}}+(2\Delta/\Gamma)^2}\left(1+\frac{4\Delta^2}{\Gamma^2}\frac{2kv_{\parallel}/\Delta}{1+I/I_{\text{sat}}+(2\Delta/\Gamma)^2}+\ldots\right)\right]\frac{I}{I_{\text{sat}}}\\ F_{\text{mol}} &= \frac{4\hbar k^2}{(1+I/I_{\text{sat}}+(2\Delta/\Gamma)^2)^2}\left(\frac{2\Delta}{\Gamma}\right)\left(\frac{I}{I_{\text{sat}}}\right)v_{\parallel}\,. \qquad (2.22)\end{aligned}$$

Note that the force here is proportional to the atom's velocity, and so for negative Δ or red detuned beams, damps the motion of the atoms. Combining three pairs of counter-propagating, red-detuned beams of appropriate polarisations oriented along the Cartesian axes results in a so-called optical molasses [86, 87]. This geometry was observed to cool a gas of ^{23}Na to below 10^{-3} K in 1986 [88, 89], and serves to cool atoms to temperatures approaching the Doppler temperature,

$$T_{\text{Doppler}} = \frac{\hbar\Gamma}{2k_B}\,. \qquad (2.23)$$

For the D2 transition of ^{87}Rb, used in our experiment, $T_{\text{Doppler}} = 146\,\mu$K.

Further cooling is achievable when considering the multiplicity of real atoms, i.e. extending the above model to multi-level atoms, and considering the interactions of atoms with polarisation gradients. Perhaps the most well-known mechanism for cooling below the Doppler temperature optically is known as Sisyphus cooling. This mechanism involves repeated conversion of kinetic energy to potential energy using a polarisation gradient. Electronic transitions occur as a result of optical pumping, repeatedly cycling atoms back to the lower-lying substates, removing the converted energy through transfer to the light field. The reader is directed to references [90, 91] for further detail on this mechanism. The important consequence of such mechanisms is that significantly lower temperatures may be obtained. For the Sisyphus mechanism in particular, the *recoil limit* is attained when the energy transferred from the atom to the light in a single cycle equals the root-mean-square kinetic energy associated with the absorption-emission event. The minimum attainable temperature for such an arrangement is then

$$T_{\text{rec}} = \frac{\mathbf{p}\cdot\mathbf{p}}{mk_B} = \frac{\hbar^2 k^2}{mk_B}\,, \tag{2.24}$$

with a value of $T_{\text{rec}} = 360\,\text{nK}$ for the D2 line of ^{87}Rb.

One important addition to the two-level model for ^{87}Rb is that the $|F = 2\rangle \rightarrow |F' = 3\rangle$ cooling transition is not completely closed. Stimulating this transition alone results in a significant atomic population entering the $|F = 1\rangle$ ground state, shown earlier in Figure 2.1, which is optically dark for the cooling transition. A low-intensity beam of repump light, slightly detuned from the $|F = 1\rangle \rightarrow |F' = 2\rangle$ transition, recycles these atoms back into the cooling cycle.

While these scattering forces play an important role in the cooling process, they do not ultimately prove a suitable candidate for achieving BEC or creating traps for ultra-cold atoms. For one, the critical temperatures for the onset of condensation are of order $10^{-7}\,\text{K}$, some $10^3 - 10^4$ times smaller than T_{Doppler}. While this is comparable to temperatures attainable through Sisyphus cooling, the quoted onset temperatures of $10^{-7}\,\text{K}$ rely on the atoms being spatially confined within a small volume. See, for example (3.10) and (3.12). The damping force of the mechanisms described thus far is not directly dependent on the *position* of an atom within the laser beams, rather only its *velocity*. The optical molasses therefore provides no spatial confinement, and cooled atoms will eventually leave the beam intersection and be lost. This shortfall can be overcome by combining a magnetic field with the optical molasses, as we shall see in §2.3.2. As an additional consideration in the context of interferometry, scattering events contribute significantly to decoherence, resulting in a loss of contrast. It is desirable in the context of this work to then minimise the scattering rate by transferring these pre-cooled atoms into a conservative trap. To further cool the atoms below the Doppler temperature, we turn to conservative atom traps, and the associated evaporative cooling mechanisms.

2.2.3 The dipole interaction potential

The optical dipole force is of particular relevance to the traps employed in this work. Captured by the real part of the polarisability, the induced dipole potential is given by

$$U_{\text{dip}}(\mathbf{r}) = -\frac{1}{2\epsilon_0 c}\text{Re}(\alpha)I(\mathbf{r})\ , \tag{2.25}$$

with resultant energy shifts for each atomic level given by

$$\Delta E_i = \frac{3}{2}\pi c^2 \times I(\mathbf{r})\sum_{i\neq j}\frac{\Gamma_{ij}C_{ij}^2}{\omega_{0,ij}^3\Delta_{ij}} \tag{2.26}$$

in the same 'far detuned' limit we used earlier. The coefficients C_{ij} are the Clebsch-Gordan coefficients for the relevant transitions, listed in [80, 92], and Δ_{ij} denotes the detuning $\Delta_{ij} = \omega - \omega_{ij}$ of the laser from each transition $i \to j$.

In the case of ^{87}Rb, the isotope used in our experiment, there are two main transitions of interest. These are the D1 transition, from $5\ ^2\text{S}_{1/2} \to 5\ ^2\text{P}_{1/2}$, and the D2 transition, from $5\ ^2\text{S}_{1/2} \to 5\ ^2\text{P}_{3/2}$. These transitions have wavelengths $\lambda_1 = 794.978\,\text{nm}$ and $\lambda_2 = 780.241\,\text{nm}$ respectively. Details of the transitions and strengths are included in Appendix A. Evaluating (2.26) for the ground and excited states of each of these two lines, and summing the contributions gives a total expression for the dipole potential

$$\begin{aligned} U_{\text{dip}}(\mathbf{r}) &= -\frac{\pi c^2\Gamma_2}{2\omega_2^3}\left(\frac{2}{\omega_2+\omega} - \frac{2}{\omega_2-\omega}\right)I(\mathbf{r}) \\ &\quad -\frac{\pi c^2\Gamma_1}{2\omega_1^3}\left(\frac{1}{\omega_1+\omega} - \frac{1}{\omega_1-\omega}\right)I(\mathbf{r}) \\ &\equiv -KI(\mathbf{r})\ , \end{aligned} \tag{2.27}$$

defining the proportionality constant K. For our dipole potentials, we use a $1064\,\text{nm}$ laser. When combined with the relevant transition properties for ^{87}Rb, and applying correction factors for the effects of polarisation (see, e.g., [81]), we obtain a value of $K = 1.857 \times 10^{-36}\,\text{m}^2.\text{s}$.

We highlight at this point the dependence of (2.27) and (2.16) on the detuning from resonance, $\Delta_i = \omega - \omega_i$. The dominant contributing term for each of these forces scales as $\mathbf{F}_{\text{sc}} \propto \frac{1}{|\Delta_i|^2}$, while $\mathbf{F}_{\text{dip}} = -\nabla U_{\text{dip}} \propto \frac{1}{|\Delta_i|}$. For large detunings, we therefore expect the scattering events to become less probable, while dipole interactions begin to dominate. For very large detunings, the effects of scattering become negligible, and the dominant dipole interaction is effectively conservative. Any loss in interaction strength from the large detuning can be compensated for by using a higher intensity beam. With $\Delta_i < 0$, the beam is said to be *red*-detuned from the atom transition, and K is a positive constant. This gives rise to minima in the dipole interaction potential at points of high intensity, and atoms are confined around the focus of a laser beam. The converse is true for positive, or *blue*, detunings, which result in atoms being repelled by the light field.

We note also that as the potential gradient $-\nabla U$ provides a force on the atoms, gradients in the intensity profile accelerate atoms in the laser beam. In many cases, this means that smoothly varying intensities are desired to prevent unwanted accelerations, which cause clouds of trapped atoms to heat. Additionally, by carefully selecting and controlling the geometries of lasers used to confine atoms, dipole interactions provide a flexible range of potentials within which experiments with ultra cold atoms may be performed.

2.3 Atomic interactions with magnetic fields

While the scattering and dipole interactions of neutral atoms with light fields provide some cooling and trapping mechanisms, it is often desirable to create large-volume, strongly confining traps. This can be achieved with magnetic traps, which form a fundamental component of the cooling process in the experiment presented in this thesis. Magnetic trapping is employed in our 2- and 3D magneto-optical traps (MOTs), and also forms a key component of the hybrid trap.

2.3.1 Zeeman effect

As with the optical forces, the interaction between an atom and an externally-applied magnetic fields arises through the magnetic dipole moment. In contrast with the optical interaction, however, the magnetic confinement couples to the *permanent* magnetic moment, rather than an *induced* electric dipole moment. When an atom with magnetic moment $\boldsymbol{\mu}$ is present in a magnetic field $\mathbf{B}$, the interaction between the two contributes an additional system energy

$$\hat{\mathcal{H}}_{\text{mag}} = -\boldsymbol{\mu} \cdot \mathbf{B} \ . \tag{2.28}$$

This interaction energy is minimised for $\boldsymbol{\mu} \parallel \mathbf{B}$, and so tends to align the magnetic dipoles along the direction of the field. The magnetic moment $\boldsymbol{\mu}$ arises from the atom's intrinsic angular momentum, which has three primary contributions. These are the spin ($\mathbf{S}$), orbital ($\mathbf{L}$) and nuclear ($\mathbf{I}$) angular momenta. Assuming $\mathbf{B}$ is oriented along the $\hat{\mathbf{y}}$ direction, the component of $\boldsymbol{\mu}$ along $\hat{\mathbf{B}}$ is then given by

$$\mu_y = -\frac{\mu_{\text{B}}}{\hbar} \left(g_S S_y + g_L L_y + g_I I_y \right) \ , \tag{2.29}$$

where $g_{S,L,I}$ are the Landé g-factors associated with each contribution, and the Bohr magneton is denoted $\mu_{\text{B}} = 9.274 \times 10^{-24}\,\text{J}\,.\,\text{T}^{-1}$. In weak $\mathbf{B}$ fields, the individual contributions from the spin, orbital and nuclear angular momenta are not independently conserved. Rather, the total angular momentum $\mathbf{F}$ is conserved, with

$$\mathbf{F} = \mathbf{S} + \mathbf{I} + \mathbf{L} \ . \tag{2.30}$$

It can be shown that the individual contributions precess about $\hat{\mathbf{B}}$. Their projections along $\hat{\mathbf{B}}$ are good quantum numbers, and the projection of $\mathbf{F}$ itself along $\hat{\mathbf{B}}$ in particular is denoted m_F. This gives rise to a simplified representation of (2.29), with

$$\hat{\mathcal{H}}_{\text{mag}} = g_F m_F \mu_{\text{B}} B_y \ , \tag{2.31}$$

and an associated force on the atom of

$$\mathbf{F}_{\text{mag}} = -g_F m_F \mu_{\text{B}} \nabla B_y \; . \tag{2.32}$$

The sign of the product $g_F m_F$ determines whether the atoms are attracted to regions of high magnetic field or low magnetic field. While static field maxima cannot be stably produced in free space, stable field minima can be created with appropriate coil geometries. As such, only the low-field seeking states can be magnetically trapped. Low-field seeking states have $g_F m_F > 0$, and for ^{87}Rb, these are the $|F, m_F\rangle = |1, -1\rangle, \; |2, 1\rangle$, and $|2, 2\rangle$ states. While $g_F m_F$ is greatest for the $|2, 2\rangle$ state, our experiment uses the $|1, -1\rangle$ state, which has substantially lower atom loss rates from the trap.

2.3.2 Magneto-optical traps

As introduced in §2.2.2 earlier, three pairs of counter propagating, red-detuned laser beams constitute an optical molasses, which may be used to create a damping force that cools atoms. Such a configuration of beams, however, suffers from the lack of spatial confinement, with damping forces dependent only on the atoms' velocities. The 1987 development of the magneto-optical trap (MOT) saw the addition of a spatially dependent restoring force to the damping provided by an optical molasses [89], thereby creating one of the first large-volume traps for electrically neutral atoms. Creating a MOT is achieved by overlaying a spatially varying magnetic field, typically a quadrupole field, with the three-axis optical molasses. Conceptually, the magnetic field induces a Zeeman splitting of the internal states, such that an electronic transition within the atom is brought closer to resonance with the laser field further from the field centre. Being closer to resonance, these atoms experience an increased scattering rate, therefore experiencing a stronger restoring force. This combination of magnetic field and laser geometry then results in spatial confinement in addition to cooling.

Considering again a two-level atom, we will allow the upper level to be split through the application of an external magnetic field into three sub-levels, with $m_F = -1, 0, +1$. In

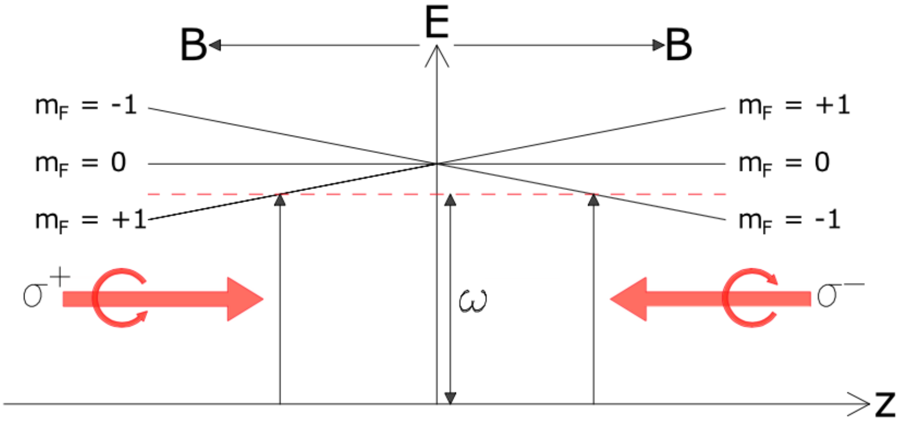

Figure 2.2: Schematic representation of the operation of a magneto-optical trap. The upper energy manifold is split into $m_F = -1, 0, +1$ levels. A magnetic field is applied, that increases linearly along the z direction. This induces Zeeman splitting of the levels. As atoms move along the $\pm z$ direction, the $m_F = \mp 1$ levels come into resonance with the laser beam travelling in the opposite direction, providing a net restoring force towards the trap centre. Circular polarisations $\sigma^\pm$ couple to the appropriate transitions selectively. Figure reproduced from [93].

our simple model, the lower level remains unsplit with $m_F = 0$. Furthermore, for simplicity, we shall let the magnetic field vary linearly in the vicinity of the trap centre. The resulting electronic structure and its spatial dependence is illustrated in Figure 2.2.

The spatial dependence of the transition energy induces a corresponding dependence in the scattering rate, with atoms further from the trap more likely to absorb photons from the laser beam(s) that push them back towards the trap centre. This is enforced through the optical transition selection rules, which couple transitions with $\Delta m_F = \pm 1$ to the circular polarisations $\sigma^\pm$ respectively. This serves to localise atoms near the centre of the magnetic field, while the optical molasses slows the motion of the atoms. This trapping technique has become a key element in modern cold atom experiments, and can readily be used to form high atom number clouds of over 10^9 atoms [29, 94]. In our experiment, we employ MOTs in both 2D and 3D geometries, with the former providing a large-volume source cloud of precooled atoms from which to load our 3D-MOT.

2.4 Conservative traps for neutral atoms

The cooling and trapping geometries presented thus far have relied on dissipative interactions as a means of cooling and confining atoms. However, as we have seen, the temperatures attainable in such traps are limited by the recoil of photons. In this section, we explore magnetic and optical confinement geometries which instead rely on conservative potentials. These potentials allow for tight, dense traps, resulting in improved hold times or lifetimes, the ability to achieve much lower temperatures, and ultimately, the formation of a BEC. In addition, limiting scattering aids in maintaining coherence within the clouds.

2.4.1 Magnetic traps

In our experiment, after loading of the 3D-MOT, we transfer the cold atom cloud to a magnetic trap. The field we employ for this purpose is that of a spherical quadrupole field, and so we shall discuss that geometry here in some detail. Additional magnetic trapping geometries will also be addressed at the end of the section. The use of radio frequency transitions as a means of evaporation in a magnetic trap will be covered in this section, as well as the primary atom loss mechanism in the quadrupole trap.

Spherical quadrupole

Experimentally, magnetic fields are most readily generated and controlled by passing currents through coils of wire. The Helmholtz configuration of coils is likely familiar to many physicists, with two coils of radius R separated by the same distance R, as for the edges of a cylinder. Such an arrangement generates a uniform field at the centre of the two coils. When creating magnetic traps, in contrast, we are aiming to create a uniform field *gradient*. Inverting the direction of the current flow in one of the coils creates such a field, with the geometry termed anti-Helmholtz, and the resultant field known as a spherical quadrupole. The geometry, along with representative field lines, is shown in Figure 2.3.

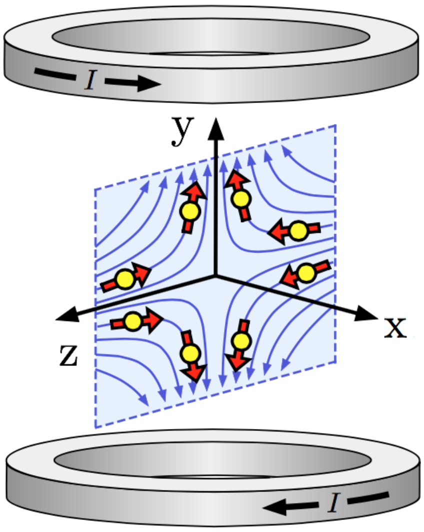

Figure 2.3: Coil arrangement and field profile of spherical quadrupole field, showing currents flowing in opposite directions in each of the two coils. The vertical dimension here is elongated for clarity, with the coil centres actually spaced by the coil radius. Shown in blue are the field lines, while the red block arrows show the alignment of atoms' magnetic moments along the field lines. Figure adapted from [75].

Importantly, about the centre of the field, the magnetic field is linear along each of the coordinate axes, i.e.

$$\mathbf{B}_{\mathrm{SQ}} = b\left(\frac{x}{2}\hat{\mathbf{x}} + \frac{z}{2}\hat{\mathbf{z}} + y\hat{\mathbf{y}}\right) , \tag{2.33}$$

where the field is parametrised in terms of b, the gradient in the y-direction. Note that the gradient along the coil axis is twice that along the radial direction, and so the coil axis is most naturally aligned so as to oppose gravity. The field gradient is readily computable in terms of the coil parameters and current, using the on-axis expressions for the field due to a single coil. Applying, for example, the law of Biot and Savart gives the field at a distance y along the axis as

$$\mathbf{B}(0,y,0) = \frac{\mu_0 I R^2}{2}\left(\frac{1}{((R/2-y)^2+R^2)^{3/2}} - \frac{1}{((R/2+y)^2+R^2)^{3/2}}\right) , \tag{2.34}$$

which in turn yields

$$b = \frac{\partial}{\partial y}\mathbf{B}(0,0,y)\bigg|_{y=0} = \frac{48\mu_0 I}{25\sqrt{5}R^2} . \tag{2.35}$$

In a purely magnetic trap, this gradient must be sufficient to provide support against gravity. For ^{87}Rb, this is $\approx 31\,\mathrm{G.cm^{-1}}$, which corresponds to a current of $6.2\,\mathrm{A}$ for our coils (see §4.2.1). Larger field gradients are generally used in the purely magnetic trap, however, as this renders it more robust against heating and leads to improved atom retention.

Evaporation in magnetic traps

The magnetic trap provides our first opportunity to cool trapped atoms evaporatively. We will return to the concept of evaporation in an optical context in §2.4.5, but include a conceptual outline here for completeness. First and foremost, elastic collisions between trapped atoms serve to cause thermalisation of a trapped ensemble. Higher velocity atoms tend, on average, to be located further from the trap centre. These atoms are subject to a larger Zeeman shift of their energy levels. Driving transitions using an RF antenna selectively outcouples atoms with larger Zeeman shifts to untrapped m_F states, thereby removing the fastest atoms from the distribution. Elastic collisions cause rethermalisation at a lower temperature, as the RMS velocity has been reduced. By steadily lowering the frequency of the RF radiation, both the spatial extent and velocity distribution of the trapped cloud are reduced, resulting in an overall reduced temperature. Very cold clouds and high number densities in both position- and momentum-space may be achieved through evaporation in magnetic traps [95], attaining temperatures as low as $\sim 200\,\mathrm{nK}$. Number densities achievable with these schemes exceed $6.2 \times 10^{10}\,\mathrm{cm^{-3}}$.

Majorana loss

The magnetic dipole placed within a magnetic field precesses about the local field in an effect known as Larmor precession. For atoms moving within spatially varying fields, the Larmor frequency

$$\omega_L = \frac{\boldsymbol{\mu} \cdot \mathbf{B}}{\hbar} \tag{2.36}$$

fixes the rate at which atoms can respond to field changes. Imagine, for example, an atom moving along a linear field gradient. Locally, it precesses at ω_L, and provided $\omega_L \gg \frac{1}{B}\frac{\partial B}{\partial t}$, the atom's precession isn't materially affected by the changing $\mathbf{B}$ field. This means it remains in the same m_F state, and adiabatically follows the field. More precisely the condition for adiabaticity reads

$$\omega_L \gg \frac{\mathbf{v} \cdot \nabla \mathbf{B}}{|\mathbf{B}|} \,. \tag{2.37}$$

This is generally easily satisfied under most experimental circumstances, with one notable exception. As $|\mathbf{B}| \to 0$, the right hand side of this equation tends to infinity, and the criterion is violated. In this circumstance, the atom's magnetic moment cannot track the local field, and the atom transitions into another m_F state in a phenomenon referred to as a Majorana spin-flip [96]. The new state is, in general, no longer trapped by the field configuration and the atom is consequently lost from the trap. This is a particular issue for cold atom clouds in quadrupole traps, which have a dense core of slow-moving atoms trapped in the vicinity of the magnetic field zero. This limits the densities achievable in the trap on the whole, and indeed leads to a heating effect. With cooler atoms preferentially leaving the trap, the remaining atoms rethermalise at a hotter temperature - the reverse, if you will, of an evaporative cooling process.

To counter these losses, which can be prohibitively large, potentials with non-zero minima have been designed. Alternative configurations of magnetic fields provide one solution, with popular examples including Ioffe-Pritchard [97] and time-orbiting potential (TOP) [98] traps. As we have alluded to earlier - an often advantageous approach involves the transfer to an entirely optical potential, for which spin flips no longer have significant loss impacts. Our experiment utilises a hybrid trapping technique, incorporating both magnetic and optical elements, exploiting the advantages offered by both trapping techniques. The hybrid trap geometry will be discussed in further detail in §2.4.3.

2.4.2 Optical traps

In order to achieve the high phase-space densities necessary for condensate formation in a solely magnetic trap, large coils are typically required to create sufficiently tight traps. Optical arrangements, on the other hand, are often much more compact. The practical advantages of optical approaches were demonstrated in 2001, with the first production of an all-optical, spinor BEC [99] of ^{87}Rb comprising 3.5×10^4 atoms distributed among the $F = 1,\ m_F = (-1, 0, 1)$ states. In our experiment, Gaussian beams are used in order to create dipole traps for cold clouds of ^{87}Rb. After initial cooling stages, atoms can be transferred into traps formed by:

- a single red-detuned beam;
- a pair of intersecting orthogonal beams; or
- a horizontal ‘sheet’ beam, with overlaid time-averaged potential.

These geometries are explored here, obtaining expressions for the trapping potentials in each case. The use of optical potentials for efficient evaporation is also discussed in this section.

Dipole trap

A Gaussian TEM$_{00}$ mode, as shown in Figure 2.4, is one of the most straightforward optical traps that can be formed. Such a beam has an intensity profile given by

$$I(\mathbf{r}) = I_0 \left(\frac{w_0}{w(z)} \right)^2 \exp\left(-2 \frac{(x^2 + y^2)}{w^2(z)} \right) , \tag{2.38}$$

where

$$\begin{aligned} w(z) &= w_0 \sqrt{1 + \left(\frac{z}{z_R} \right)^2} \text{ , and} \qquad (2.39) \\ z_R &= \frac{\pi w_0^2}{\lambda} \, . \qquad (2.40) \end{aligned}$$

Here w_0 is known as the beam waist, and is adjustable by varying the focal lengths of lenses used in beam expansion and focussing. The Rayleigh length z_R is defined as the distance from the focus, measured along the propagation direction, over which the beam radius expands by $\sqrt{2}$. Typically $w_0 \gg \lambda$, and so the Rayleigh length satisfies $z_0 \gg w_0$. In cold atom experiments, the beam waist is typically of order 10^2–10^3 µm, with Rayleigh

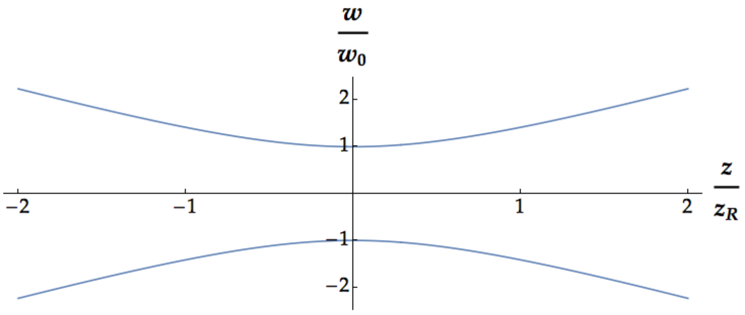

Figure 2.4: Longitudinal profile of a Gaussian TEM$_{00}$ mode. The blue curve shows the $1/e^2$ radius of the transverse beam profile as a function of position along the beam. The beam is propagating along the z axis, with its focus occurring at $z = 0$. Coordinates are normalised by the waist, determined by the optics used, and the Rayleigh length, given by $z_R = \frac{\pi w_0^2}{\lambda}$.

lengths $\sim 1\,\text{mm}$.

For red-detuned beams, the induced dipole interaction causes atoms to be drawn to points of high intensity. In this case, cold atoms collect at the beam focus. For sufficiently deep traps, i.e. a more intense laser field, the potential is approximately harmonic. Modelling the energy levels of an atom confined in a harmonic potential is quite straightforward, with spacings given in terms of the trapping frequencies. Expanding the potential in quadratic terms about $\mathbf{r} = 0$, we find

$$\begin{aligned} U_{\text{dip}}(\mathbf{r}) &\approx \frac{2KI_0}{w_0^2}x^2 + \frac{2KI_0}{w_0^2}y^2 + \frac{KI_0}{z_R^2}z^2 - KI_0\,, && (2.41)\\ &\equiv -V_{\text{depth}} + \tfrac{1}{2}m_{\text{Rb}}\left(\omega_x^2x^2 + \omega_y^2y^2 + \omega_z^2z^2\right)\,, && (2.42)\end{aligned}$$

which defines the trapping frequencies

$$\begin{aligned} \omega_{x,y}^2 &= \frac{4KI_0}{m_{\text{Rb}}w_0^2}\,, \text{ and} && (2.43)\\ \omega_z^2 &= \frac{2KI_0}{m_{\text{Rb}}z_R^2}\,, && (2.44)\end{aligned}$$

and the trap depth

$$V_{\text{depth}} = KI_0\,. \tag{2.45}$$

In practice, the peak intensity I_0 isn't an easily measurable quantity, and so we typically express the frequencies and trap depth in terms of the total beam power instead. The power is given by the integral of the intensity profile over the x and y directions, yielding

$$\begin{aligned} P &= \int_{-\infty}^{\infty}\int_{-\infty}^{\infty} dx\, dy\, I(\mathbf{r}) \\ &= \tfrac{1}{2}\pi w_0^2 I_0 \ , \end{aligned} \tag{2.46}$$

such that the frequencies become

$$\omega_{x,y}^2 = \frac{8KP}{\pi m_{\mathrm{Rb}} w_0^4} \ , \text{ and} \tag{2.47}$$

$$\omega_z^2 = \frac{4KP}{\pi m z_R^2 w_0^2} \ . \tag{2.48}$$

This gives an aspect ratio of

$$\frac{\omega_{x,y}}{\omega_z} = \frac{\sqrt{2} z_R}{w_0} \ , \tag{2.49}$$

which, given $z_R \gg w_0$ leads to clouds of trapped atoms being elongated dramatically along the length of the beam. In practice, this may reduce the trapping frequency along the length of the beam so far as to prevent confinement along the beam altogether. Combining a magnetic field, or additional optical beams in crossed traps instead, provides improved confinement along the third dimension. This is particularly important in order to maintain high elastic collision rates, and thermalisation in the trap, which are key elements required for effective evaporation.

Crossed dipole traps

Two crossed, red-detuned beams provide confinement along all three Cartesian axes, stemming the expansion of trapped atom clouds along the length of a single beam. When combining two or more laser beams, with suitably chosen polarisations to avoid interference, the trapping frequencies add in quadrature. For simplicity, we consider the case of two crossed beams of equal waist and power, propagating along the x and z directions

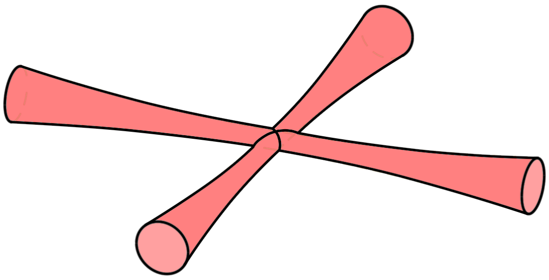

Figure 2.5: Diagrammatic representation of two crossed dipole beams. Atoms are trapped in the region of beam overlap at the centre of the image, with tighter vertical confinement than for a single beam. Image adapted from [75].

respectively, as shown in Figure 2.5.

As, in the absence of interference, the potentials from individual beams add, we combine the trapping frequencies in quadrature to obtain

$$\omega_{x,z}^2 = \frac{8KP}{m_{\mathrm{Rb}}\pi w_0^4} + \frac{2KP}{m_{\mathrm{Rb}}\pi w_0^2 z_R^2}\ , \text{ and} \tag{2.50}$$

$$\omega_y^2 = 2 \cdot \frac{8KP}{m_{\mathrm{Rb}}\pi w_0^4}\ . \tag{2.51}$$

This demonstrates the capability of this beam arrangement to prevent expansion of the atoms along the length of either beam, and also shows the increase in the vertical confinement by a factor of $\sqrt{2}$. It is often a good approximation to neglect the contribution to $\omega_{x,z}$ of terms which depend on the Rayleigh length, z_R, as they are typically much smaller than the transverse confinement provided by the other beam.

Sheet confinement

The above treatment assumed a beam profile that is cylindrically symmetric about the propagation direction. By using cylindrical lenses, however, beams may be focussed and expanded independently along the two Cartesian axes in the transverse plane. This yields a flat 'sheet' beam, with tight confinement along only one of the Cartesian axes, in contrast with the previous example.

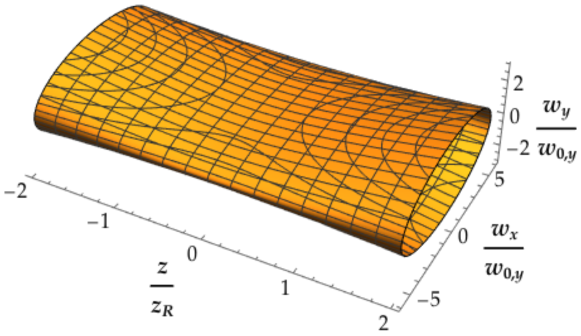

Figure 2.6: Longitudinal profiles of a cylindrically-expanded sheet beam. The beam is propagating along the z direction. Tight confinement is provided in the y direction, with a relaxed trapping frequency in the x direction. A waist ratio of 5.5 is chosen here, solely for illustrative purposes. The plotted contour shows the coordinates at which the intensity has dropped by a factor of $1/e^2$.

Figure 2.6 shows an example of such a sheet beam. Notably, the increased waist along the x direction also leads to a dramatic increase in the corresponding Rayleigh length, such that the transverse intensity profile along x is essentially uniform over the same range of z values.

The intensity profile of the sheet can be described as

$$I(\mathbf{r}) = I_0 \left(\frac{w_{0,x} w_{0,y}}{w_x(z) w_y(z)} \right) \exp \left(-2 \frac{x^2}{w_x(z)^2} - 2 \frac{y^2}{w_y(z)^2} \right) , \tag{2.52}$$

which takes the same form as (2.38) earlier, but allows for independent waists in the x and y directions. Performing the same expansion as earlier yields the trapping frequencies

$$\omega_x^2 = \frac{8KP}{m_{\mathrm{Rb}} \pi w_{0,x}^3 w_{0,y}} , \tag{2.53}$$

$$\omega_y^2 = \frac{8KP}{m_{\mathrm{Rb}} \pi w_{0,x} w_{0,y}^3} , \text{ and} \tag{2.54}$$

$$\omega_z^2 = \frac{2KP}{m_{\mathrm{Rb}} \pi w_{0,x} w_{0,y}} \left(\frac{1}{z_{R,x}^2} + \frac{1}{z_{R,y}^2} \right) . \tag{2.55}$$

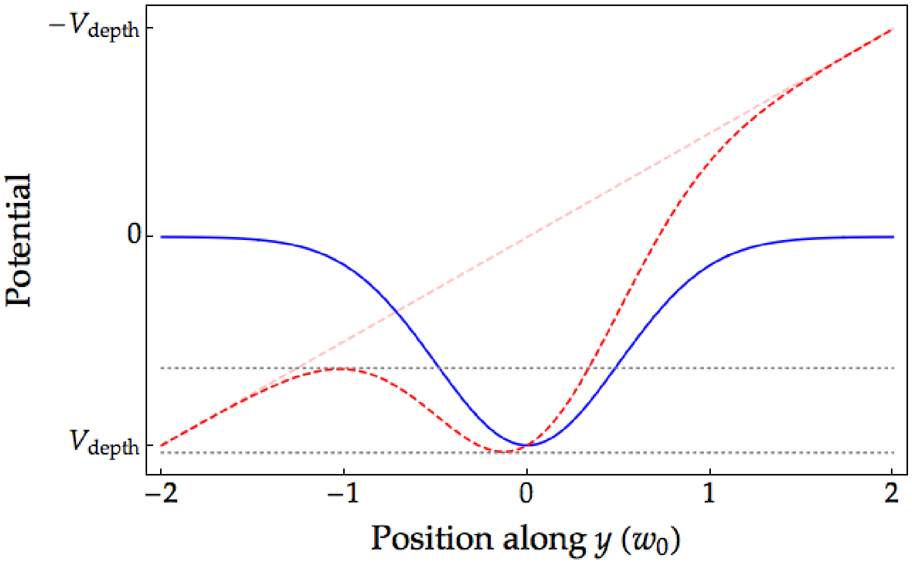

Figure 2.7: A schematic representation of the effect of gravity on the trap depth, and the location of the minimum of an optical dipole trap, in the vertical direction. The solid, blue curve shows the Gaussian profile in the absence of gravity. The red, dashed curve shows the anharmonic trap created as the effects of gravity are included. These effects are more pronounced for weaker traps. Noteworthy features include the reduced depth, indicated by the horizontal grey lines, and the shift in the location of the minimum slightly to the left.

Effects of gravity

It is noteworthy for not only the sheet potential, but generally for optical dipole potentials, that the effect of gravity is usually non-negligible. Including gravity in the total potential experienced by the atom adds a linear term, which may begin to dominate in weaker traps, including when performing optical evaporation. This results in a slight anharmonicity, and a sag in the location of the minimum relative to the beam focus. Most notably, however, the depth of the trap is significantly reduced. A schematic representation of this is shown in Figure 2.7.

2.4.3 Hybrid magnetic & optical traps

While traditionally magnetic traps have been frequently used to create high atom-number BECs, including the first realisation of condensation in an atomic vapour [29, 30], modern approaches tend to favour optical [99, 100] approaches. Optical traps, however, suffer from low trap loading rates and very high laser intensities needed to provide adequate confinement against gravity. A hybrid magnetic and optical approach [101] aims to combine the advantages of both approaches. Hybrid traps can yield BECs of ^{87}Rb of up to 2×10^6 atoms in short duty cycles of $\sim 16\,\mathrm{s}$. Having trapped and cooled a large number of atoms to, or near to, degeneracy in the hybrid trap, the cooled atoms can be efficiently transferred to all-optical potentials, which enables studies with spinor BECs [99, 102, 103]. In this context, the hybrid traps may be viewed as a bridge between the large-volume, spin-selective magnetic traps, and smaller, spin-insensitive optical traps.

Overlaying an optical dipole trap a small distance below the magnetic field zero shifts the potential minimum away from the zero, and mitigates Majorana losses. Further to this, hybrid traps offer a solution for the anharmonicity, sag, and trap depth reduction induced by gravity. In the given configuration, the magnetic field provides confinement against gravity, restoring the full trap depth and Gaussian profile of the dipole trap for an appropriate choice of field gradient. In the case of ^{87}Rb in the $|F = 1, m_F = -1\rangle$ state, this corresponds to a gradient of $30.5\,\mathrm{G.cm}^{-1}$. Profiles of the hybrid field are shown in Figure 2.8.

The apparatus used for this work first achieved BEC in a hybrid geometry similar to [101] in October 2014, and we have subsequently created time-averaged all-optical potentials for high atom-number, nearly-arbitrary planar potentials [1]. We now routinely form BECs of $\sim 1.5 \times 10^6$ atoms in our hybrid trap, with yet higher atom numbers achievable in our larger, all-optical ring structures after transferring from the hybrid trap.

2.4.4 Time-averaged optical potentials

Combining the beam geometries presented thus far provides us with an understanding of the trap shown in Figure 1.7. If we additionally allow the vertical, or ‘scanning’, beam to move around the sheet, we open the door to a diverse range of optical planar potentials for cold atom experiments. With technologies such as acousto-optical modulators, the location of the intersection of the vertically propagating beam with the sheet may be

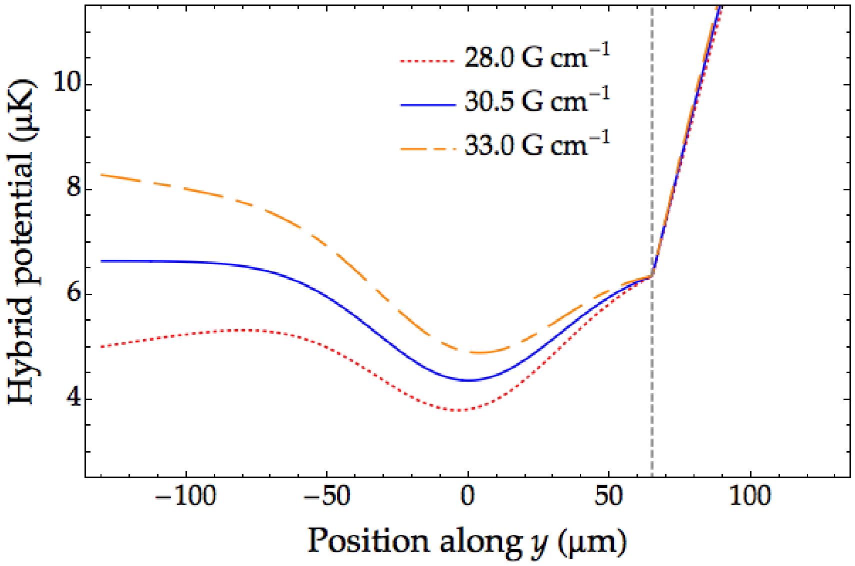

Figure 2.8: Hybrid magnetic and optical trapping potential along the vertical axis, plotted for a selection of magnetic field gradients. The potential comprises an optical dipole trap using a 100 mW beam of 1064 nm laser light, focussed to a 65 μm $1/e^2$ waist, and a spherical quadrupole field, as used in our experiment. The vertical, dashed, grey line shows the location of the magnetic field zero, at which Majorana spin-flip losses occur. This is offset by one waist from the dipole trap, in a region of low atomic density, preventing large losses. At $30.5\,\mathrm{G.cm}^{-1}$, the field gradient is enough to support against gravity, evidenced by the flat tail as $y \to -100^+$. This cancels the gravitational sag and trap depth reduction suffered by all-optical traps, c.f. Figure 2.7.

controlled, thereby adjusting the location of the atom cloud. By rapidly scanning this beam, continuous geometries can be formed, acting, e.g. as waveguides for atomic flow.

The concept of time-averaged potentials for cold atoms, while recent, certainly isn't foreign [104]. Time-averaged and time-orbiting traps are often used in magnetic settings to avoid low-field seeking, spin-polarised atoms from passing through the zero of a magnetic field, which results in Majorana spin flips and large-scale atom loss, as in [62, 105].

In order for us to be able to treat the potential as time-averaged, we require that the scanning speed far exceeds the speed at which the atoms are able to respond. In the particular case of a BEC, this is captured by the trap frequncies, as well as the speed of sound in the condensate. We shall return to this point again in chapter 3, when discussing our experimental implementation.

We shall first consider the case of an ideal sheet beam, in which there is finite confinement in the y direction, against gravity, but the transverse confinement and variations in the depth are negligibly small. We shall denote the position of the focus of the scanning beam within the sheet as $\mathbf{r}_t$, and neglect the confinement in the y direction due to the scanning beam itself, as this will be dominated by contributions from the sheet. The instantaneous potential due to the scanning beam at time t is then

$$U_{\text{scan}}(\mathbf{r}, t) = -KI(\mathbf{r} - \mathbf{r}_t) \ , \tag{2.56}$$

which, on average, is

$$\langle U_{\text{scan}}(\mathbf{r}) \rangle_T = -\frac{K}{T} \int\limits_T dt\ I(\mathbf{r} - \mathbf{r}_t) \ , \tag{2.57}$$

with T the period of the scanning. The total potential is found by adding the sheet confinement term, which is approximately harmonic, $U_{\text{sheet}} = \frac{1}{2} m_{\text{Rb}} \omega_y^2 y^2$. In both of the above expressions, $I(\mathbf{r})$ denotes the Gaussian profile of a dipole beam given in (2.38). For a continuous scan at fixed speed, this is equivalent to the spatial convolution

$$\langle U_{\text{scan}}(\mathbf{r}) \rangle_T = -K \int d^2\mathbf{r}'\ I(\mathbf{r} - \mathbf{r}')\ f(\mathbf{r}') \ , \tag{2.58}$$

provided the period of the scan is much shorter than the atoms' response time. As mentioned earlier, the integration is carried out only over the x and z dimensions, as contributions to confinement along the scanning beam are negligible in comparison with the sheet confinement. Here $f(\mathbf{r}')$ describes the beam locations which contribute to the overall potential. For example, the function

$$f(\mathbf{r}') = \frac{1}{2\pi r} \delta(\sqrt{x'^2 + z'^2} - r) \tag{2.59}$$

describes a ring of radius r, while

$$f(\mathbf{r}') = \frac{1}{L} \left(\Theta(x' + L/2) - \Theta(x' - L/2) \right) \delta(z') \ , \tag{2.60}$$

with Θ the Heaviside step function, describes a line trap of length L along the x direction. The simplicity of the form of (2.58) means that a diverse collection of potentials can be generated in this manner, with precise control over the function f.

In our arrangement, there are some additional factors which also need to be considered. In particular, the approximation that the sheet is ideal does not hold true over the length scales in which we are interested. Even with carefully corrected intensities for the vertical beam at each location in its scan [74], the creation of larger rings is still inhibited by the shape of the sheet. In the first instance, this has minimal effect on the trapping frequencies, as the gradients in the sheet beam potential remain small. It does, however, lead to significant variations in the trap depth at different locations in the combined potential of the sheet and scanning beams.

We are particularly interested in the generation of ring potentials, and so shall consider them specifically here. Considering the sheet potential shown in Figure 2.6, we can immediately see the source of the depth variations. For potentials with spatial extent comparable to the Rayleigh length, there is a substantial change in the peak intensity of the sheet, as in Figure 2.9. Given our BECs have energies at the nanokelvin scale, even relatively conservative rings of radii $\sim 5\,\%$ of the Rayleigh length are sensitive to the rolloff of the sheet in the x direction. The situation is further pronounced for rings that are not centred on the sheet, as in Figure 2.10. For weak traps with depths ~ 50–$200\,\mathrm{nK}$, changes of this magnitude can have a dramatic effect on the angular density profile of atoms trapped in the potential.

In addition, these considerations apply to an ideal sheet and time-averaged potential. Any additional beam structure on either the sheet or vertical beams, or slight angles in the propagation direction of the sheet, further exacerbate these variations in trap depth, and can introduce additional offsets and gradients into the angular trap depth profiles. In chapter 4, we will present a feedforward algorithm designed to combat these variations, enabling the creation of considerably larger ring structures with large atom numbers and

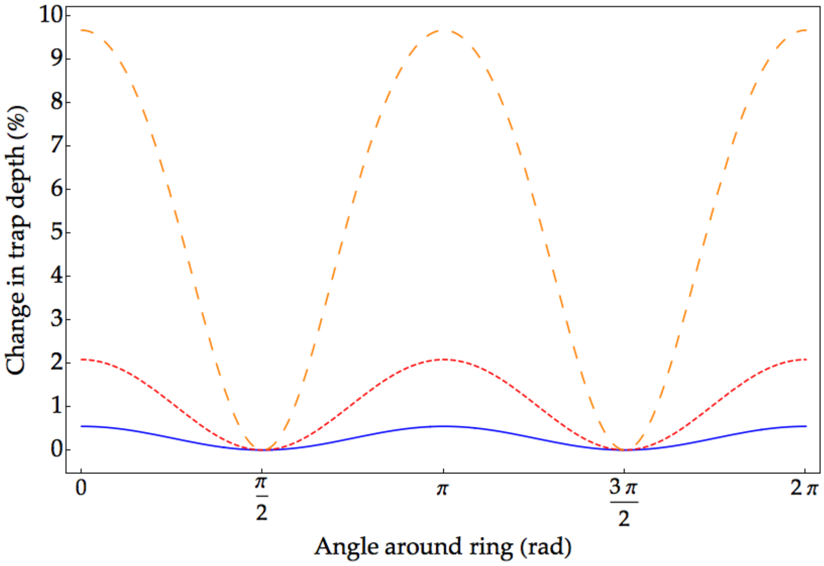

Figure 2.9: Variation in the trap depth of rings formed on a sheet due to the elliptical shape of the sheet. This figure shows curves for rings with their centres coinciding with the focus of the sheet beam. The three curves correspond to rings of radius (a) 1 % (blue, solid); (b) 2 % (red, dotted); and (c) 5 % (orange, dashed) of the y Rayleigh length. In what is shown, the x waist is 5.5 times larger than the y waist.

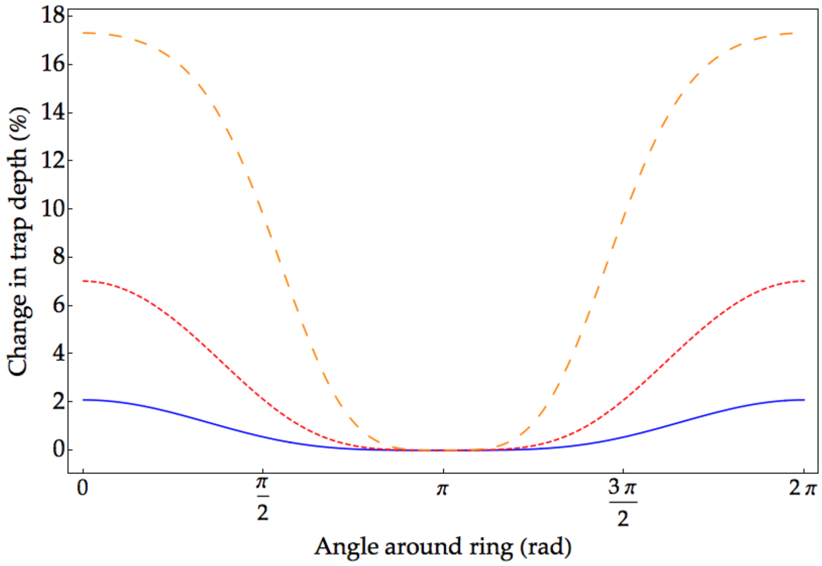

Figure 2.10: Variation in the trap depth of rings formed on a sheet due to the elliptical shape of the sheet. This figure shows curves for rings with one side of the ring coinciding with the focus of the sheet beam. The three curves correspond to rings of radius (a) 1 % (blue, solid); (b) 2 % (red, dotted); and (c) 5 % (orange, dashed) of the y Rayleigh length. In what is shown, the x waist is 5.5 times larger than the y waist.

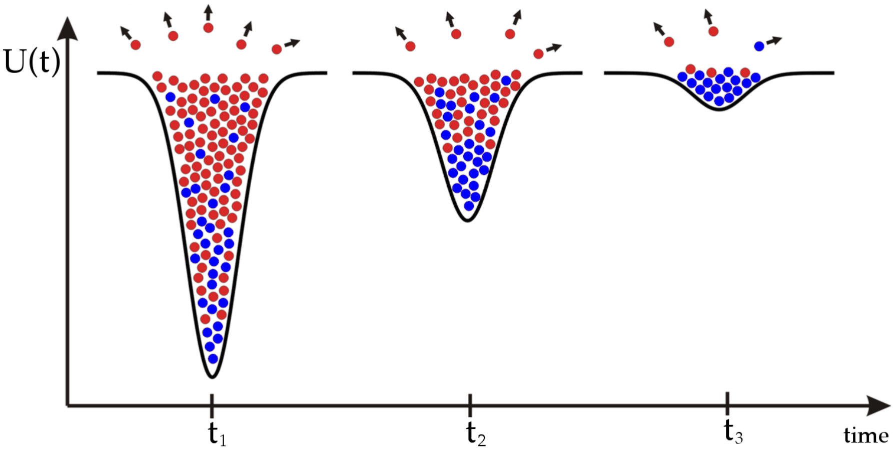

Figure 2.11: Schematic representation of the evaporation process in an optical dipole trap. Atoms in the trap have a statistical distribution of velocities consistent with their temperature. Here, hotter atoms are shown in red, while colder atoms are shown in blue. Colder atoms preferentially occupy the deepest parts of the trap, while hotter atoms are more often found at the edges. By slowly lowering the trap depth, these hotter atoms are selectively removed. The remaining atoms rethermalise at a lower temperature. Image adapted from [82].

low density variation around the ring.

2.4.5 Optical evaporation

The use of the dipole interaction in conjunction with Gaussian beams also provides an effective means of cooling atoms below the Doppler temperature, via an evaporative mechanism [106]. As we saw in the magnetic trap, we aim to selectively remove the hottest (or equivalently fastest) atoms from an ensemble, allowing the remaining atoms to rethermalise at a lower temperature. In an optical dipole potential, this is achieved by slowly lowering the intensity of the laser beam, affording access to the temperatures necessary for condensate formation. The process relies on the rethermalisation of atoms which remain trapped, which occurs most rapidly for tighter (higher frequency) traps. As a consequence, the beam intensity can be lowered quickly initially without causing additional loss. A schematic representation of the optical evaporation is shown in Figure 2.11. This mechanism was used to form the first ^{87}Rb BEC in a crossed-dipole trap comprising 2 beams derived from a CO_2 laser [99].

2.4.6 Parametric heating

The difficulty associated with directly and precisely measuring the beam waists at the trapping location make a direct calculation of the trapping frequency difficult. In practice, the reverse process is used instead: the trapping frequencies are identified experimentally, and the beam waists and corresponding Rayleigh lengths determined from these. The trapping frequencies may be determined by a process called parametric heating, in which the power of the trapping beam is modulated at an angular frequency ν. It can be shown [107, 108] that significant heating and particle loss occur for modulation frequencies $\nu = 2\omega_i$, even if the magnitude of the modulation is quite small.

In addition to providing a direct technique for measuring the trapping frequencies, this phenomenon gives insight into an additional heating mechanism. Any noise on the trapping beam intensity with a frequency close to this parametric resonance can potentially result in quite a dramatic loss of atoms, or a significant rise in the temperature of the cloud.

2.5 Detecting cold atoms

Measurements in condensate experiments follow largely from collecting images of the atoms. In our experiment, we employ an absorption imaging technique. This is one of the simplest techniques for detecting atoms, and relies - as the name suggests - on the absorption of resonant light by the atoms. While simple, however, the technique has been demonstrated to resolve mean atom numbers as low as 3.7 atoms [109]. The imaging light passes through the atom cloud, during which time the atoms absorb some of the light in a density-dependent manner. By comparing an image of the illuminating laser light with and without atoms present, the density profile may be extracted. A simplified diagram illustrating the principle is shown in Figure 2.12. Quantities such as the atom number are measured by the light transmission, and the temperature is extracted from the extent of the cloud in ballistic expansion.

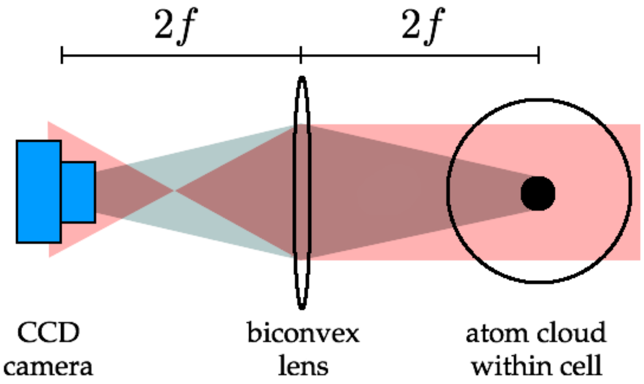

Figure 2.12: Schematic depiction of absorption imaging. The shadow cast by the atoms is focussed onto the CCD surface for imaging. The probe laser beam is shown here in red. Alternative lens arrangements can be used to provide magnification.

To convert the data in the images to number densities, we need to account for the light which has been blocked by the atoms. We showed earlier in (2.18) the rate of incoherent scattering of imaging light uniformly in all directions. This corresponds to an absorption cross section

$$\sigma = \frac{3\lambda^2}{2\pi}\frac{1}{1+I/I_S+(2\Delta/\Gamma)^2}\ , \tag{2.61}$$

where Γ is the width of the atomic transition, Δ the detuning of the imaging light from the transition, I the intensity of the imaging light and I_{sat} is the saturation intensity of the transition, as given by (2.17). This cross-section may be used in the Beer-Lambert law for intensity attenuation,

$$\frac{dI}{dz} = -n(x,y)\sigma I\ . \tag{2.62}$$

Naturally, the photons arriving at the camera have passed through the atom cloud along a particular dimension. As a result, they contain little information about the density profile along the beam propagation direction, but correspond instead to the density integrated along the corresponding dimension. This quantity is often referred to as the column density, $n(x, y)$. Combining the above equations yields

$$n(x, y) = \frac{1}{\sigma} \ln \left(\frac{I(x, y)}{I_a(x, y)} \right) , \tag{2.63}$$

also given in [82, 110]. Here $I_a(x, y)$ denotes the imaging light intensity, including the shadow cast by the atoms, while $I(x, y)$, with no subscript, denotes the imaging intensity with no atoms present. In practice, the imaging intensities used are much lower than the transition's saturation intensity. Under these conditions, the I/I_S term in the denominator of (2.61) can be neglected.

It is useful here to also introduce the optical density (OD), equal to the logarithm in (2.63), prior to division by σ. The OD captures the shape of the column density, while remaining computationally straightforward to evaluate, without considering factors such as the detuning and saturation intensity. In practice, as in other laboratories [82], we capture 3 images when evaluating the OD. The first two images correspond to the intensities in the above expressions, while the third is an image of the background light with the imaging laser turned off. This third dark image, with intensity profile $I_D(x, y)$, is subtracted from both other images before evaluating the ratio, i.e.

$$\mathrm{OD} = \ln \left(\frac{I(x, y) - I_D(x, y)}{I_a(x, y) - I_D(x, y)} \right) . \tag{2.64}$$

Computationally, the total atom number may then be determined by summing the OD at each camera pixel, multiplying by the pixel area, and dividing by the cross-section. This effectively forms the integral of the column density,

$$N_{\text{total}} = \iint dx\, dy\, n(x, y) \approx \frac{1}{\sigma} A_{\text{pixel}} \sum_{i,j} \mathrm{OD}_{i,j} . \tag{2.65}$$

Chapter 3

Bose-Einstein condensation

The extension of textbook, single-particle quantum mechanics, as described by the Schrödinger equation, to many-particle systems naturally gives rise to two sub-classes of fundamental particles. We can write the combined wavefunction for two indistinguisable particles labelled '1' and '2', in terms of their single particle wavefunctions as

$$\Psi(\mathbf{x}_1, \mathbf{x}_2) = \tfrac{1}{2}\left(\psi_1(\mathbf{x}_1)\psi_2(\mathbf{x}_2) \pm \psi_1(\mathbf{x}_2)\psi_2(\mathbf{x}_1)\right) \ , \tag{3.1}$$

where the total wavefunction is either symmetric or antisymmetric under the exchange of the two particles, depending on the choice of sign between the terms. This exchange interaction is represented mathematically by swapping the spatial coordinates x_i. The specific form above arises from the condition that the measurable particle density, $|\Psi(\mathbf{x}_1, \mathbf{x}_2)|^2$, is invariant under the exchange operation - i.e. a mathematical expression of indistinguishability. This separation of the multi-particle wavefunction into the symmetric and antisymmetric branches leads to a natural division of particles into two separate groups: *bosons* and *fermions*.

Taking the negative sign results in an antisymmetric wavefunction, which describes the fermions. This fermionic nature is manifest in the particles' spin quantum numbers, which for fermions are half-integers, $\pm\frac{1}{2},\ \pm\frac{3}{2},\ \ldots$. Of note is the fact that the wavefunctions themselves ψ_1 and ψ_2 cannot be equal for fermions. Were this the case, enforcing indistinguishability under particle exchange, i.e. $x_1 \leftrightarrow x_2$, requires the combined two-particle wavefunction to identically equal zero. This is a manifestation of the Pauli exclusion principle, which states that two fermions cannot, regardless of temperature or other factors, macroscopically occupy the same single particle state. This forms the basis for quantum descriptions of chemistry phenomena, as electrons with $|s| = \frac{1}{2}$ are fermions, and therefore subject to Pauli exclusion.

On the other hand, bosons, or particles of integer spin, do not suffer from the same cancellation. They correspond to symmetric solutions of (3.1), for which setting the wavefunctions ψ_1 and ψ_2 equal to one another results in a non-zero combined wavefunction. This signifies the ability of identical bosons to exist in the same quantum state simultaneously. By reducing the temperature dramatically, the statistics of such a particle result in a macroscopic accumulation of bosons in an ensemble in the corresponding single-particle ground state. This is a phenomenon known as Bose-Einstein condensation.

3.1 Bose-Einstein statistics

The theory underpinning Bose-Einstein condensation was first proposed in 1924 [26–28], and as such is well-developed and has been summarised in textbooks and review articles [110]. What follows below loosely parallels the discussion found in [111], to which the reader is referred for additional detail and discussion.

At 'normal' temperatures T, for which $k_B T$ is much larger than the spacing between adjacent energy levels of a particle, we are familiar with taking a Maxwell-Boltzmann distribution $\propto \exp(-E_i/k_B T)$ to describe the spread of particles among different energy states. Indeed, both fermions and bosons have near-Boltzmann distributions in this regime. At colder temperatures, however, the statistics for bosons and fermions diverge from the Boltzmann case. The mean occupation of a state i for a non-interacting boson is given

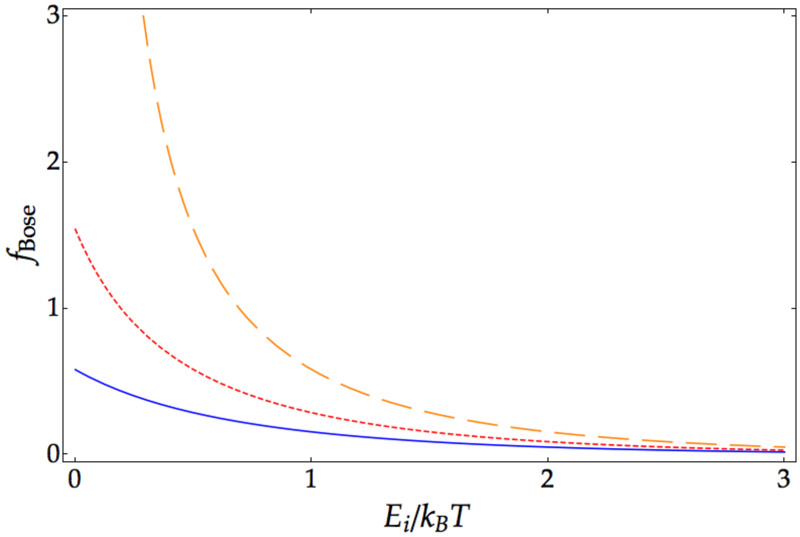

Figure 3.1: Bose distributions for state energies $E_i \sim k_BT$. Curves are shown for different values of the chemical potential μ. The blue, solid curve corresponds to $\mu = -k_BT$. The red, dotted curve corresponds to $\mu = -0.5k_BT$. Finally, the dashed, orange curve corresponds to $\mu = 0$, and applies for all temperatures T below the onset of condensation.

instead by the Bose distribution,

$$f_{\text{Bose}}(E_i) = \frac{1}{\exp[(E_i - \mu)/k_BT] - 1}\,, \tag{3.2}$$

where μ denotes the chemical potential. (Incidentally, fermions are subject to a similar distribution, but $+1$ replaces -1 in the denominator). The role of μ is to explicitly enforce the conservation of total particle number, and an expression for it in terms of N and T may be derived accordingly, using the relation $N = \sum_i f_{\text{Bose}}(E_i)$. Figure 3.1 shows the distribution for a selection of chemical potentials. We note also, that for larger values of T, states with larger values of $E_i - \mu$ are occupied, and the Bose distribution satisfies

$$f_{\text{Bose}}(E_i) \simeq \exp[-(E_i - \mu)/k_BT]\,, \tag{3.3}$$

i.e. the Bose distribution is equal asymptotically to the Maxwell-Boltzmann distribution.

In order for the distribution function to remain non-negative, we must impose a condition on $\mu(T)$ as the temperature decreases. In this limit, bosons accumulate in the ground state, and μ increases. It cannot, however, exceed the energy of the lowest single-particle state without f_{Bose} becoming negative. The consequence of this is that the maximum occupation of any excited state is

$$N_{\text{max}}(E_i) = \frac{1}{\exp[(E_i - E_{\text{min}})/k_B T] - 1} \; . \tag{3.4}$$

If these states are unable to accommodate all N particles in an ensemble, then the remaining particles macroscopically occupy the ground state, forming a Bose-Einstein condensate. This is encapsulated in the asymptotic behaviour of the $\mu = 0$ curve in Figure 3.1, which shows the occupancy of a state with $(E_i - \mu) \to 0$ can be arbitrarily large. In the following section, we will determine the lowest attainable temperature before atoms must begin to collect in the ground state. This is termed the *critical temperature*, T_c.

3.2 Critical temperature and condensate fraction

In order to determine T_c, we will take an approach common in thermal and statistical physics. For all excited states, we shall assume that $k_B T$ exceeds the level spacing, and that the total number of atoms in excited states

$$N_{\text{ex}} = \sum_i f_{\text{Bose}}(E_i) \; , \tag{3.5}$$

is well approximated by the integral

$$N_{\text{ex}} \approx \int_0^\infty dE \; g(E) \; f_{\text{Bose}}(E) \; , \tag{3.6}$$

where $g(E)$ is the density of states. By arguing that on average, one quantum state exists per volume $(2\pi\hbar)^3$ of phase space, it can be shown [111] that

$$g_{\text{fp}}(E) = \frac{V m^{3/2}}{2^{1/2}\pi^2\hbar^3} E^{1/2} \; , \tag{3.7}$$

for an ensemble of free particles of mass m in a volume V, and in particular

$$g_{\text{ho}}(E) = \frac{E^2}{2\hbar^3 \omega_x \omega_y \omega_z} \,, \tag{3.8}$$

for an ensemble of particles confined to a 3-dimensional harmonic potential. Here ω_i denotes the trapping frequency along the i axis, as introduced in § 2.4.2.

Integrating (3.6) with the density of states for the harmonic potential (3.8), we find

$$N_{\text{ex}} = \left(\frac{k_B T}{\hbar}\right)^3 \frac{1}{\omega_x \omega_y \omega_z} \sum_{k=1}^{\infty} \frac{[\exp(\mu/k_B T)]^k}{k^3} \,. \tag{3.9}$$

In the limit $\mu \to 0$, the number of atoms in the excited state saturates as the sum in the previous equation reduces to the Riemann zeta function, $\zeta(3)$. This yields the critical temperature at which the onset of condensation occurs,

$$T_{c,\text{ho}}(N) = \frac{\hbar}{k_B} \left(\frac{N \omega_x \omega_y \omega_z}{\zeta(3)}\right)^{1/3} \,. \tag{3.10}$$

This may be further used to show that the fraction of condensed atoms in a 3-dimensional, harmonic trap is given by

$$\left.\frac{N - N_{\text{ex}}}{N}\right|_{\text{ho}} = 1 - \left(\frac{T}{T_{c,\text{ho}}}\right)^3 \,. \tag{3.11}$$

In the later parts of this thesis, we concern ourselves primarily with ring geometries. These have harmonic confinement along the y direction, and centred at radius R along the radial direction. The calculation in [112] follows the approach above, and yields the condensation temperature

$$k_B T_{c,\text{ring}} = \left(\frac{3N\hbar^3 \omega_y \omega_\rho}{4\Gamma(\frac{5}{2})\zeta(\frac{5}{2})(2m)^{1/2} R}\right)^{2/5} \,, \tag{3.12}$$

and consequently the condensate fraction obeys

$$\left.\frac{N - N_{\mathrm{ex}}}{N}\right|_{\mathrm{ring}} = 1 - \left(\frac{T}{T_{c,\mathrm{ring}}}\right)^{5/2} . \tag{3.13}$$

The reduced index reflects the geometry change, with the ring geometry having only two degrees of harmonic confinement, with the remaining angular coordinate acting as a 'box' of length $2\pi R$. Each degree of harmonic confinement contributes $+1$ to the index, while the angular 'box' dimension contributes the remaining $+\frac{1}{2}$. For a treatment of the thermodynamic properties for more general potentials, we refer the reader to [113].

3.3 Density profiles

Typically, the quantity most readily accessible for measurement is the atomic density profile, by means discussed in §2.5. The discussion so far has revolved around the statistical occupation of energy states, but has given no consideration to these density profiles. By neglecting interactions between atoms, the discussion so far has implicitly assumed the states and their energies are unchanged by the multi-particle nature, and so for N_c condensed atoms, we can write

$$\Psi_{N_c}(\mathbf{r}) = \sqrt{N_c}\psi_0(\mathbf{r}) , \tag{3.14}$$

assuming the normalisation $\int d^3\mathbf{r}|\Psi_{N_c}(\mathbf{r})|^2 = N_c$, such that $|\Psi_{N_c}(\mathbf{r})|^2$ gives the atomic number density. ψ_0 describes a single-particle, ground state solution to the Schrödinger equation. Remembering that for condensed atoms, $\mu \to E_{\mathrm{min}}$, μ is the quantity which appears in place of the ground state energy,

$$\mu\Psi_{N_c}(\mathbf{r}) = -\frac{\hbar^2}{2m}\nabla^2\Psi_{N_c} + V(\mathbf{r})\Psi_{N_c} . \tag{3.15}$$

For a harmonic potential, the result for the single particle ground state is found in any undergraduate text (see, for example, [114]), and yields a Gaussian wavefunction with corresponding density,

$$n(\mathbf{r}) = \frac{N_c}{\pi^{3/2}\bar{a}^3} \exp\left[-\left(\frac{x^2}{a_x^2} + \frac{y^2}{a_y^2} + \frac{z^2}{a_z^2}\right)\right] , \tag{3.16}$$

where $a_i = \sqrt{\hbar/m\omega_i}$ are the oscillator lengths, and $\bar{a}$ denotes the geometric mean, $\bar{a} = (a_x a_y a_z)^{1/3}$. These lengths are a factor of $\left(\frac{2k_B T}{\hbar\omega_i}\right)^{1/2}$ smaller than the corresponding width for thermally distributed atoms, and a similar factor exists between the distributions of momenta as well. The non-condensed component is therefore typically markedly larger, less dense, and disperses more quickly once released from the trap.

Moreover, in trap the density of condensed atoms in *momentum* space is given by the Fourier transform of Ψ_{N_c}, which gives

$$\tilde{\Psi}_{N_c}(\hbar\mathbf{k}, t = 0) = \frac{1}{\pi^{3/4}\bar{c}^{1/2}} \exp\left[-\left(\frac{\hbar^2 k_x^2}{2c_x^2} + \frac{\hbar^2 k_y^2}{2c_y^2} + \frac{\hbar^2 k_z^2}{2c_z^2}\right)\right] , \tag{3.17}$$

with $c_i = \hbar/a_i$. Once released from trap, the potential term in the Schrödinger equation is zero, and so the wavefunction evolves as

$$\tilde{\Psi}_{N_c}(\hbar\mathbf{k}, t) = \tilde{\Psi}_{N_c}(\hbar\mathbf{k}, 0) \exp\left(-i\frac{\hbar(\mathbf{k}\cdot\mathbf{k})t}{2m}\right) . \tag{3.18}$$

Evaluating the inverse Fourier transform and squaring, we obtain the density profile in time-of-flight expansion:

$$|\Psi_{N_c}(\mathbf{r}, t)|^2 = \frac{1}{\pi^{3/2}} \prod_i \frac{1}{a_i\sqrt{1+\omega_i^2 t^2}} \exp\left[-\frac{r_i^2}{a_i^2(1+\omega_i^2 t^2)}\right] . \tag{3.19}$$

For $t \gg \omega_i^{-1}$, we find that the condensate expands to have widths given by $a_i\omega_i t$ in each direction. Given large ω_i leads to small a_i, this reflects an inversion in the observed *aspect ratios* between dimensions relative to their in-trap density profile. Shorter dimensions in trap become large in time-of-flight, while longer dimensions tend to expand more slowly. This anisotropic expansion serves as a common marker for the existence of a condensate, as the expansion of thermal atoms is instead isotropic.

Interacting bosons

While the non-interacting model predicts several of the key features observed in BECs, a more realistic model should account for the interactions between the atoms themselves. At normal room temperatures and pressures, it's a straightforward calculation to show that the particle densities are typically $\sim 10^{19}\,\mathrm{cm}^{-3}$. Typical condensates, however, are several orders of magnitude less dense, at $\sim 10^{12}$–$10^{13}\,\mathrm{cm}^{-3}$. Consequently, the interaction between atoms at positions $\mathbf{r}$ and $\mathbf{r}'$ is well-described by the contact potential

$$U_{\text{int}}(\mathbf{r}-\mathbf{r}') = g\delta^{(3)}(\mathbf{r}-\mathbf{r}') \ , \tag{3.20}$$

where the coupling constant $g = \dfrac{4\pi\hbar^2 a_s}{m}$ depends on the s-wave scattering length a_s of the species. This amounts to adding an extra density-dependent potential into the Schrödinger equation,

$$i\hbar\frac{\partial}{\partial t}\Psi = -\frac{\hbar^2}{2m}\nabla^2\Psi + (V_{\text{ext}} + g|\Psi|^2)\Psi \ . \tag{3.21}$$

This equation is known as the Gross-Pitaevskii equation (GPE), and effectively describes weakly-interacting gases. We can, for example, immediately extract the shape of the ground state density. In the limit of formation of a pure condensate, $T \to 0$, with the consequence that the kinetic term in the GPE is negligible. This is known as the Thomas-Fermi approximation. The total energy is given by the chemical potential, and so we have for the ground state density

$$n_{\text{TF}}(\mathbf{r}) = |\Psi|^2 = \begin{cases} \dfrac{\mu - V(\mathbf{r})}{g} & , \ \mu > V \\ 0 & , \ \mu \leq V \ . \end{cases} \tag{3.22}$$

This form allows the chemical potential to be calculated readily, by enforcing normalisation of the wavefunction.

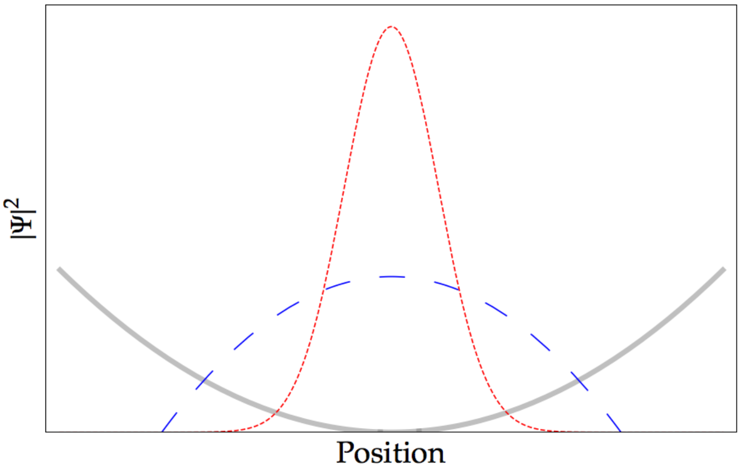

Figure 3.2: A comparison between the non-interacting and Thomas-Fermi solutions for the ground state wave function of a harmonic potential, shown in grey. The dotted, red curve shows the density profile for an ideal Bose gas. The dashed, blue curve shows the Thomas-Fermi solution for weakly interacting bosons, namely the negative of the confining potential. To clearly show the shape change between ideal and Thomas-Fermi solutions, the difference in peak densities has been reduced. The ideal Bose gas solution is generally much narrower.

These solutions often vary quite dramatically from the solutions for a non-interacting gas, though many of the same concepts (including anisotropic expansion) apply in the same way as discussed above. Figure 3.2 shows a comparison between the non-interacting and Thomas-Fermi solutions along one dimension.

3.4 Bogoliubov expansion

Of course, under experimental conditions, we can never truly reach the Thomas-Fermi limit, with $T \to 0$, but rather will have some fraction of atoms occupying the ground state, while the remaining atoms distribute themselves among low-lying excited states. To capture these low-energy excitations, we must extend the GPE model described above by retaining higher-order terms in the expansion. Under second quantisation formalism, we can write the full Hamiltonian for an ensemble of particles in a potential V as

$$\begin{aligned}\hat{\mathcal{H}} &= \int d^3\mathbf{r}\ \hat{\Psi}^\dagger(\mathbf{r}) \left[-\frac{\hbar^2}{2m}\nabla^2 + V(\mathbf{r}) \right] \hat{\Psi}(\mathbf{r}) \\ &\quad + \frac{1}{2} \iint d^3\mathbf{r}\ d^3\mathbf{r}'\ \hat{\Psi}^\dagger(\mathbf{r})\hat{\Psi}^\dagger(\mathbf{r}')U_{\text{int}}(\mathbf{r}-\mathbf{r}')\hat{\Psi}(\mathbf{r}')\hat{\Psi}(\mathbf{r})\ , \end{aligned} \tag{3.23}$$

where $U_{\text{int}} = g\delta^{(3)}(\mathbf{r}-\mathbf{r}')$ describes the interaction between atoms in the condensate. The bosonic nature is enforced through the Bose commutation relations for the field operators

$$\left[\hat{\Psi}(\mathbf{r}),\hat{\Psi}^\dagger(\mathbf{r}')\right] = \delta^{(3)}(\mathbf{r}-\mathbf{r}')\ , \quad \left[\hat{\Psi}(\mathbf{r}),\hat{\Psi}(\mathbf{r}')\right] = 0\ , \quad \text{and} \quad \left[\hat{\Psi}(\mathbf{r})^\dagger,\hat{\Psi}^\dagger(\mathbf{r}')\right] = 0\ . \tag{3.24}$$

For low temperatures, well below the condensation temperature T_c, the field operator $\hat{\Psi}(\mathbf{r})$ can be treated as a perturbation on the condensate wavefunction. Following the approach taken in [79], we decompose the field operator in the form

$$\hat{\Psi}(\mathbf{r},t) = \Phi(\mathbf{r},t) + \delta\hat{\Psi}(\mathbf{r},t)\ , \tag{3.25}$$

with Φ the wavefunction of the condensate itself, and $\delta\hat{\Psi}$ a small perturbation for non-condensed atoms. Our treatment earlier neglected the contribution of $\delta\hat{\Psi}$ altogether, constituting a zeroth order approximation to $\hat{\Psi}$. Retaining the contribution of $\delta\hat{\Psi}$ to first order allows for the identification of low-energy eigenvalues. We are interested in finding the energies of excitations above the condensate's chemical potential, and so consider the full Hamiltonian as the sum of a mean-field contribution $\mu\hat{N}$, and the excitations, denoted here by $\hat{K}$.

Substituting (3.25) into (3.23) gives the excitations

$$\begin{aligned}\hat{K} &= (E_0-\mu N_0) + \int d^3\mathbf{r}\,\Big(-\delta\hat{\Psi}^\dagger(\mathbf{r},t)\frac{\hbar^2}{2m}\nabla^2\delta\hat{\Psi}(\mathbf{r},t)\\ &+ \left[V(\mathbf{r})+2g|\Phi(\mathbf{r},t)|^2-\mu\right]\delta\hat{\Psi}^\dagger(\mathbf{r},t)\delta\hat{\Psi}(\mathbf{r},t)\\ &+ \frac{g}{2}\Big(\Phi(\mathbf{r},t)^2[\delta\hat{\Psi}^\dagger(\mathbf{r},t)]^2 + \Phi^*(\mathbf{r},t)^2[\delta\hat{\Psi}(\mathbf{r},t)]^2\Big)\Big)\ ,\end{aligned} \tag{3.26}$$

which we now seek to express in the spectral representation.

Under the action of $\hat{K}$, the operators $\delta\hat{\Psi}$ and $\delta\hat{\Psi}^\dagger$ evolve according to the coupled equations

$$\begin{aligned} i\hbar\frac{\partial\delta\hat{\Psi}}{\partial t} &= \left[-\frac{\hbar^2}{2m}\nabla^2 + V(\mathbf{r}) + 2n_0(\mathbf{r})g - \mu\right]\delta\hat{\Psi} + g\Phi(\mathbf{r})^2\delta\hat{\Psi}^\dagger \text{ , and} \quad (3.27) \\ -i\hbar\frac{\partial\delta\hat{\Psi}}{\partial t} &= \left[-\frac{\hbar^2}{2m}\nabla^2 + V(\mathbf{r}) + 2n_0(\mathbf{r})g - \mu\right]\delta\hat{\Psi}^\dagger + g\Phi^*(\mathbf{r})^2\delta\hat{\Psi} \text{ .} \quad (3.28) \end{aligned}$$

Here n_0 denotes the number density of *condensate* atoms only. Noting that for fixed-energy states, we expect the time evolution to be encapsulated by rotating exponentials of the form $\exp(\pm iE_it/\hbar)$, we assume trial solutions of the form

$$\delta\hat{\Psi}(\mathbf{r},t) = \sum_i \left[u_i(\mathbf{r})\hat{\alpha}_i \exp(-iE_it/\hbar) - v_i^*(\mathbf{r})\hat{\alpha}_i^\dagger \exp(+iE_it/\hbar)\right] \text{ .} \quad (3.29)$$

Here $\hat{\alpha}_i^\dagger$ is the creation operator for a boson in the i^{th} energy state. This type of transformation of the field operators is known as a Bogoliubov transformation [115], with appropriate choices of u and v diagonalising the operator $\hat{K}$. Enforcing the condition that the transformation be canonical, i.e. the new $\hat{\alpha}_i$ operators must also obey the Bose commutation relations, we additionally impose

$$\int d^3\mathbf{r} \; \left[|u_i(\mathbf{r})|^2 - |v_i(\mathbf{r})|^2\right] = 1 \text{ .} \quad (3.30)$$

Moreover, the condensate wavefunction Φ is free to be taken as real. Expressed in terms of u and v, the coupled equations (3.27) and (3.28) become the Bogoliubov equations

$$\begin{aligned} \left[-\frac{\hbar^2}{2m}\nabla^2 + V(\mathbf{r}) + 2g_0(\mathbf{r}) - \mu - E_i\right]u_i(\mathbf{r}) - gn_0(\mathbf{r})v_i(\mathbf{r}) &= 0 \text{ , and} \quad (3.31) \\ \left[-\frac{\hbar^2}{2m}\nabla^2 + V(\mathbf{r}) + 2g_0(\mathbf{r}) - \mu + E_i\right]v_i(\mathbf{r}) - gn_0(\mathbf{r})u_i(\mathbf{r}) &= 0 \text{ .} \quad (3.32) \end{aligned}$$

Identifying the eigenvalues E_i allows the excitations to be expressed in diagonal form, with $\hat{K} =$ constant $+ \sum_i E_i\hat{\alpha}_i^\dagger\hat{\alpha}_i$, or the sum of products of excitation energies and numbers.

Excitations in a BEC

In this thesis we are exploring ring geometries, which have a uniform potential in the angular direction. This warrants a brief introduction of the Bogoliubov excitations present in a uniform potential. Given the spatial invariance of such a potential, we can express the Bogoliubov functions u and v as plane-wave solutions,

$$u(\mathbf{r}) = \frac{u_{\mathbf{k}}}{\sqrt{\tau}} \exp(i\mathbf{k}\cdot\mathbf{r}) \qquad \text{and} \qquad v(\mathbf{r}) = \frac{v_{\mathbf{k}}}{\sqrt{\tau}} \exp(i\mathbf{k}\cdot\mathbf{r}) \ , \tag{3.33}$$

and we may also take $V(\mathbf{r}) = 0$. Here τ is the system volume, which is included to allow for normalisation. Using these solutions in the Bogoliubov equations gives for the state energies

$$E_{\mathbf{k}} = \sqrt{\frac{\hbar^2 k^2}{2m}\left(\frac{\hbar^2 k^2}{2m} + 2n_0 g\right)} \ . \tag{3.34}$$

For small $|\mathbf{k}|$, this reduces to the form

$$E_{\mathbf{k}} \simeq \hbar k\sqrt{\frac{n_0 g}{m}} = \hbar k\sqrt{\frac{\mu}{m}} \ . \tag{3.35}$$

As the energy is linear with $|\mathbf{k}|$, this describes a sound-like excitation, with $\hat{\alpha}^{\dagger}_{\mathbf{k}}$ creating a single phonon. The speed of sound-wave propagation is given by the surd, $c_s = \sqrt{\frac{\mu}{m}}$. For large $|\mathbf{k}|$, we obtain instead the following energy:

$$E_{\mathbf{k}} \simeq \frac{\hbar^2 k^2}{2m} + g n_0 \ , \tag{3.36}$$

which describes a free particle propagating in the mean field of the condensate atoms. A threshold for the change in behaviour from collective to free excitations is defined when the bracketed terms in (3.34) are equal to one another. This defines ξ, the condensate healing length,

$$\xi^2 = \frac{1}{8\pi n a_s} = \frac{\hbar^2}{2m\mu} \ . \tag{3.37}$$

This length is the typical scale over which the condensate wavefunction 'heals' to the bulk value when subject to a local perturbation.

3.5 Interference, atom interferometry and coherence

The linearity of the Schrödinger equation leads to a natural mapping between a description of electromagnetic fields, and the atomic wavefunction. We are all familiar with the concept of superposition in the context of electromagnetism, in which we sum contributions to the total electric field at a point on a screen from all points in a source aperture. We represent this mathematically as

$$\mathbf{E}(\mathbf{r}) = \int\limits_{\text{aperture}} dx'\ dy'\ \mathbf{E}_0 \exp\left(i\mathbf{k}\cdot(\mathbf{r}-\mathbf{r}') - i\omega t\right)\ , \tag{3.38}$$

and calculate the squared complex norm of the resultant to obtain the intensity profile. In direct analogy with optical interference, condensates exhibit similar behaviour. When propagating along a direction in which there is no confinement (i.e. in free space, or along a flat waveguide), the wavefunction has momentum distribution given by (3.18). Noting that $\mathbf{p}t = ms_{\mathbf{p}}$, where $s_{\mathbf{p}}(t)$ is the distance travelled by that momentum component in time t, we find that the wavefunction itself has a rotating exponential of the same form as (3.38). The squared complex norm $|\Psi_{N_c}|^2$ therefore plays an analogous role to the intensity in optical interference, yielding fringes in the atomic density. These contributions are complicated by the fact that a BEC comprises a distribution of momenta, much like using a multifrequency laser in optical interference. This leads to a variation in the fringe structure over time.

Extending the wavefunction to include internal degrees of freedom, such as the spin state, permits the use of non-spatial quantities as a measure of the phase difference between BEC sources. This can prove valuable in that typical fringe spacings are often shorter than optical resolution permits - and so can be difficult to measure. The same principle as above exists, but instead of measuring the position of fringes as the signal for phase difference, one can instead measure the relative populations of different internal states - often much more readily achievable.

Given these options for signals to measure, it is natural to then ask how well - even with perfect detection ability - these signals would portray information about the phase. It is a well understood concept in optics and laser physics that transition linewidths lead to a timescale (and corresponding length) over which the laser beam's phase can no longer be expected to be correlated. This is quantified by the *coherence time* (length), which we aim to make as large as possible for the most robust, sensitive interferometric measurements. An analagous concept exists in BEC, with fluctuations in the phase arising in condensate geometries approaching the 2D (and indeed, 1D) limits. The phase fluctuations arise not only due to the geometry [116–119], but also from the effects of finite temperature and whether or not thermal equilibrium is maintained during evaporation [120]. In the case that the coherence time or length is inadequate, the contrast in the density fringes washes out, limiting the detection resolution of the device.

In [112], the coherence properties of a BEC confined to a toroidal potential are explored. Rescaling the lengths with $l_y = \sqrt{2\mu/M\omega_y^2}$, $l_\rho = \sqrt{2\mu/M\omega_\rho^2}$, and assuming thermal occupation of low-lying Bogoliubov modes, Mathey et al. show that the correlation function of the phase is given by

$$\langle \delta\varphi(\theta,0)^2 \rangle = \sum_j \frac{2gN_j}{2\pi^2 R l_y l_\rho E_j}(1-\cos(j\theta)) \, , \tag{3.39}$$

where the sum is evaluated over the states j. N_j is given by the Bose distribution (3.2), while θ denotes the angular position around the ring, and φ denotes the condensate phase at that location. The role of this phase is evident in the density-phase model, which assumes a condensate wavefunction of the form $\Psi_{N_c}(\mathbf{r}) = \sqrt{n(\mathbf{r})}\exp(i\varphi(\mathbf{r}))$. For small energies E_j, the occupancy is dominated by the term

$$N_j \approx \frac{k_B T}{E_j} \, , \tag{3.40}$$

and summing over these energies E_j yields

$$\langle \delta\varphi(\theta,0)^2 \rangle = \frac{g k_B T}{\pi^2 l_y l_\rho} \frac{R}{(\hbar c)^2} (-\theta^2/2 + \pi|\theta|) \ . \tag{3.41}$$

The single-particle correlation function therefore decays as

$$\langle \Psi^\dagger(\theta)\Psi(\theta') \rangle \sim \exp\left(-\frac{R|\theta-\theta'|}{l_\varphi} \right) \ , \tag{3.42}$$

where the coherence length l_φ is given by

$$l_\varphi = \frac{\hbar^2 N_c}{\pi m R k_B T} \ . \tag{3.43}$$

It is customary to define the transition from phase coherence to the phase fluctuating regime in BEC be equating the coherence length with the longest dimension in the system. In this case, we let $l_\varphi = \pi R$, to obtain the temperature, T_φ, below which phase fluctuations are suppressed,

$$k_B T_\varphi = \frac{\hbar^2 N_c}{\pi^2 m R^2} \ . \tag{3.44}$$

The main result of this thesis demonstrates the production of large ring BECs of radii up to $100\,\mu\text{m}$, with system-size coherence demonstrated by cloud temperatures well below T_φ.

Chapter 4

Experimental apparatus

The experimental realisation of atomic Bose-Einstein condensates is still a comparatively new achievement, with the first creation of a BEC having occurred in 1995. While degeneracy has since been reached on a number of occasions, the construction and calibration of a system capable of producing a BEC remains a non-trivial exercise. In this chapter, we describe the ^{87}Rb BEC apparatus used in this work, detailing features including our vacuum, laser setup, and magnetic field arrangements.

Overview

Our system design is based on NIST's experiment [101], comprising a dual-vacuum arrangement, with a high vacuum (HV) section at $\sim 10^{-7}$ mbar connected to an ultra-high vacuum (UHV) section at $\sim 10^{-11}$ mbar via a low-conductance feedthrough. The HV section includes a glass, rectangular vapour cell, while the UHV contains an octagonal glass cell with seven optical ports in the horizontal plane, as well as optical access both above and below. The eighth face in the horizontal plane connects the octagonal glass cell to the remainder of the vacuum. In the high-vacuum section, the higher pressures favour MOT loading, and so we form a cigar-shaped, 2D magneto-optical trap in this region. Atoms are transferred from this large cloud through the feedthrough into the ultra-high vacuum, where a full 3D-MOT is formed. The lower pressure in the UHV region prevents atom loss due to background collisions with untrapped atoms. After loading the 3D-MOT, the cooling lasers are extinguished, and the atoms are transferred into the quadrupole magnetic trap. Radio frequency evaporation is then used to further decrease the temperature of the atoms. This results in a smaller, denser cloud, suitable for loading into the hybrid trap. Overlaying the dipole and/or sheet beams at this stage of the sequence creates the final potentials for the atoms.

Prior to my candidacy, the experiment was able to produce large 3D-MOTs of ^{87}Rb, however had not yet succesfully formed a condensate. A short time into my candidacy, we were able to routinely form large 3D-MOTs of up to $\sim 3 \times 10^9$ atoms, which now yield nearly-pure BECs of 1.5×10^6–2.0×10^6 atoms in our ‘standard’ hybrid trap. Over the course of my candidacy, we implemented a time-averaged, all-optical trap for creating large ring potentials, including feedforward methods to smooth the potential to a uniform trap depth. By the end of my candidacy, we were able to routinely create phase coherent ring BECs of up to 3.0×10^6 atoms in large, time-averaged traps with radii from $50\,\mu\mathrm{m}$ through $150\,\mu\mathrm{m}$.

4.1 Initial cooling stages

In this section, we will briefly cover the vacuum system, the generation of the cooling and repump light, and the 2D-MOT arrangement. These systems had already been constructed and were functioning prior to my candidature, and are presented here briefly for completeness. The interested reader is directed to [75] for further detail on the technical aspects, construction and characterisation of these elements.

4.1.1 Vacuum system

Our vacuum system is shown in Figure 4.1. The first element of note is the glass vapour cell, which acts as the chamber for our 2D-MOT. By passing current through a filament

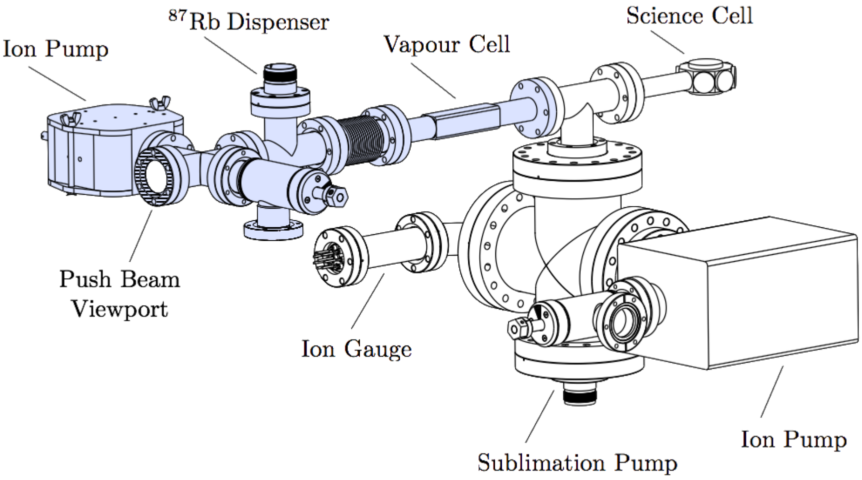

Figure 4.1: Vacuum system used in our experiment. The 2D-MOT is formed in the vapour cell, while the stages from 3D-MOT through to BEC take place in the science cell. The various pumps maintain pressures of 10^{-7} mbar on the vapour cell side, and 10^{-11} mbar on the science cell side. Leading from the vapour cell into the T-piece between it and the science cell is a narrow feedthrough, which maintains the $\sim 1000\times$ pressure difference between the high (blue) and ultra-high (white) vacuum sections. Image adapted from [75].

of rubidium contained in the dispenser section, a vapour of rubidium is injected into the system. The large, rectangular windows of the vapour cell offer optical access for the cylindrically-expanded cooling beams used to form a 2D-MOT. The vapour cell windows are $25.4\,\mathrm{mm}\times 100\,\mathrm{mm}$ rectangles, to match optics used for the overlaid molasses. The viewport neighbouring the ion pump[1] is colinear with the vapour and science cells, and permits optical access for a push beam. The push beam is $20\,\mathrm{MHz}$ red-detuned from the cooling transition. This beam moves ^{87}Rb atoms from the 2D-MOT in the vapour cell, into the science cell, where they are recaptured in the 3D-MOT.

The ultra-high vacuum section is maintained with an Agilent titanium sublimation pump, and a Varian Starcell ion pump. The science cell itself, manufactured by Colorado Precision Glass, comprises seven $25.4\,\mathrm{mm}$ diameter windows in the horizontal plane, and two $40\,\mathrm{mm}$ diameter ports above and below the cell. These windows are broadband coated on both surfaces with anti-reflective (AR) films, which prevent optical interference of both

---

[1] This Gamma Vac 10S pump has subsequently failed from alkali poisoning, but this has not proved detrimental to the system operation.

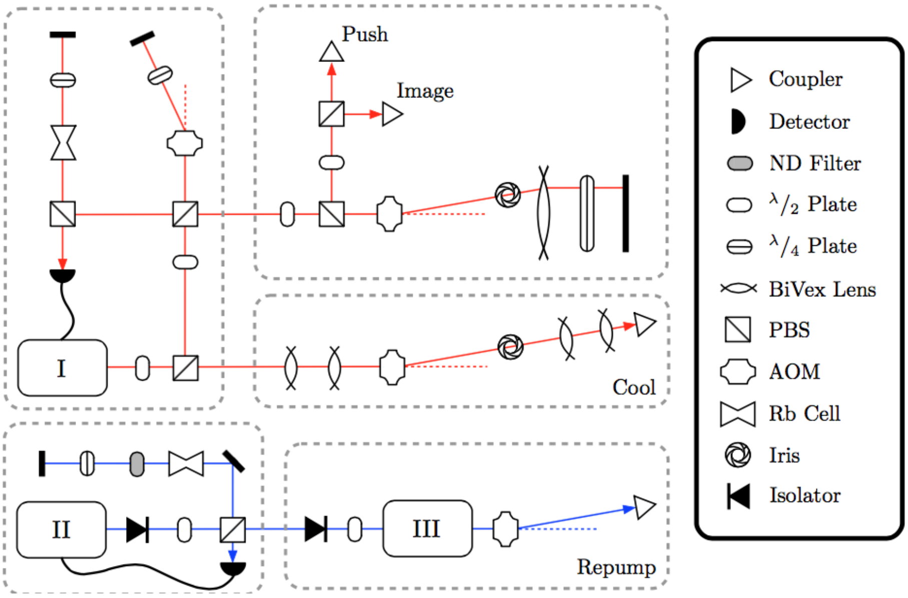

Figure 4.2: Cooling and repump laser arrangement. (I) 1 W Toptica TA-Pro diode laser, used as the source for our cooling light. The double-passed AOM in the top-left box provides control over the lock to the $F = 2 \rightarrow F' = (2, 3)$ crossover. This laser is then divided for cooling and imaging purposes. (II) 40 mW Toptica DL-100 diode laser, used for the repump transition. Isolators prevent back-reflections from the spectroscopy cell. (III) 500 mW Toptica DLX110 used to amplify the laser intensity. Image reproduced from [75].

the 780 nm and 1064 nm lasers used for cooling, trapping and imaging. The design of the cell facilitates a high level of optical access from all directions, which we shall return to when discussing our MOT and optical trapping configurations.

4.1.2 Cooling laser arrangement

The beams for cooling and repump are derived from Toptica diode lasers. Acousto-optical modulators (AOMs) are used to dynamically control the frequencies, with shifts of order 10^2 MHz routinely available with many commercial devices. However, as the cooling and repump transitions are separated by over 6.5 GHz (see Figure 2.1), with the major contribution from the 6.835 GHz splitting of the $5^2\,\mathrm{S}_{1/2}$ hyperfine levels, two separately-locked lasers are required. The arrangement is shown in Figure 4.2.

Our cooling light is derived from a 1 W Toptica TA-Pro diode laser, which is locked 320 MHz above the $F = 2 \rightarrow F' = (2, 3)$ crossover resonance using saturated absorption spectroscopy. This feature is selected for locking as it is particularly strong, and therefore provides a stable signal for the lock. The frequency is shifted down by $201.7\,$MHz using an AOM, to arrive at the final frequency, $15\,$MHz red-detuned from the cooling transition. This laser is then distributed with an arrangement of wave plates and polarising beam splitters among the cooling, imaging, and push beams. The laser frequency may be varied by changing the driving RF frequency, enabling us to detune the beams further from resonance when imaging denser clouds.

The repump light is supplied by a seed $40\,$mW Toptica DL100 diode laser, locked on resonance with the repump transition. While generally low intensities are required for the repump light, this laser acts as a seed for several experiments. It is therefore subsequently amplified by injection locking into a $500\,$mW Toptica DLX110 laser.

The cooling, imaging, push, and repump beams are then fibre-coupled, and transferred across to the main experiment table. Here an arrangement of polarising beam splitters and $\frac{\lambda}{2}$ waveplates are used to divide the cooling and repump light between the 2D- and 3D-MOTs. The cooling light is further divided among the two axes for the 2D-MOT, and three axes for the 3D-MOT respectively. Only low intensities are required for the repump light, and it need not be coupled in from all axes, rather can enter the 2D- and 3D-MOTs through a single coupler. The imaging beam is distributed between the horizontal and vertical axes using a similar arrangement.

4.1.3 2D-MOT

The 2D-MOT, within the high-vacuum portion of the system, is readily loaded from the rubidium dispenser at the higher pressures in this portion of the system. Two pairs of race-track coils, shown in Figure 4.3, provide magnetic confinement along two axes. Little confinement is provided along the long axis of the coils, which facilitates pumping of the atoms through to the ultra-high vacuum. The $\sim 4.3\,$W heat generated by the coils under normal operating conditions is readily lost to the surrounding air, and we do not

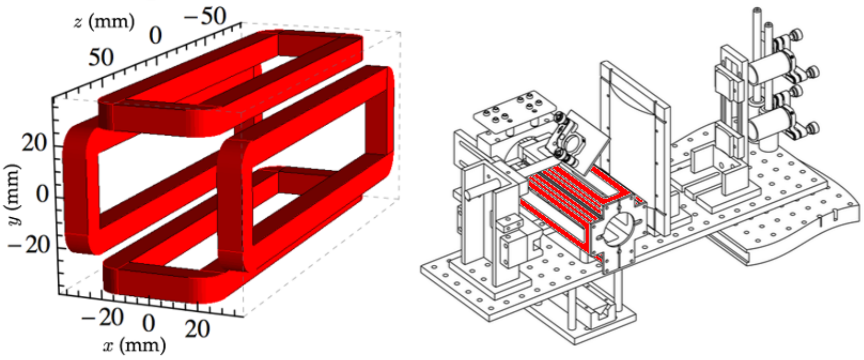

Figure 4.3: 2D-MOT coils, and their placement within the full 2D-MOT arrangement. *Left*: Coil shape and arrangement. The rectangular area enclosed by each coil matches the $25.4\,\mathrm{mm}$ vapour cell width. Each coil is wound from $0.615\,\mathrm{mm}$ diameter enamelled wire, with 40 turns per coil. This provides a gradient of $4.12\,\mathrm{G.cm^{-1}.A^{-1}}$. *Right*: Placement of the coils about the vapour cell, and relative to the 2D-MOT optics. At the right, the vertical (top) and horizontal (bottom) couplers for the cooling beams are shown, along with the cylindrical lenses to expand the beams. At the left, and supported below the main breadboard, are depicted the prisms that retro-reflect the beams back on themselves. Image adapted from [75].

employ any additional cooling for the coils.

Cooling light is supplied via polarisation-maintaining fibres. The collimators incorporate a quarter-wave plate, rendering the beams circularly-polarised. Beams are expanded using a pair of cylindrical lenses: an $f = -50\,\mathrm{mm}$ lens, followed by an $f = 200\,\mathrm{mm}$ lens. The beams form a cigar-shaped intersection volume in the centre of the vapour cell. The alignment and operating currents of the 2D-MOT are optimised by the loading of the 3D-MOT, using the fluorescence signal focussed onto a photodiode. Optimum loading is found to occur for $\sim 5\,\mathrm{A}$ per coil, corresponding to a gradient of $\sim 20\,\mathrm{G.cm^{-1}}$ at the cell centre.

4.2 Ultra-high vacuum

The 2D-MOT forms rapidly under the higher-pressure environment relative to the ultra-high vacuum. Using a push beam, derived from the cooling laser, atoms are pumped into the UHV region, in which they are recaptured in the 3D-MOT, before further transfers into cold atom traps. Here we detail the parameters and geometry of our 3D-MOT and

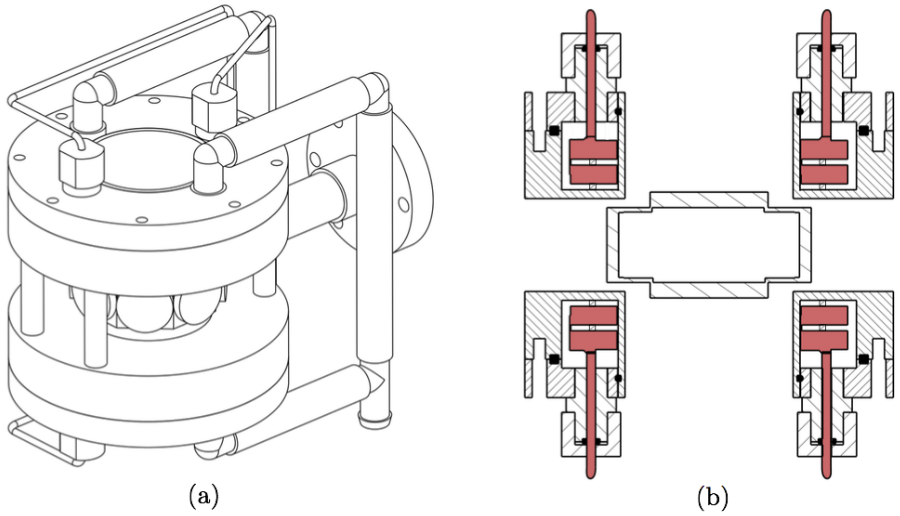

Figure 4.4: Quadrupole field arrangement surrounding the science cell in the ultra-high vacuum portion of the experiment. The coils are connected externally via a switch box, which allows for fast switch-off, and also for independent control of the two coils for purposes of levitation. (a) Coils depicted within their cooling cases, and shown surrounding the science cell. The support posts separate the coils so as to satisfy the anti-Helmholtz condition. (b) Cutaway showing the pairs of coils within the casing. Image reproduced from [75].

magnetic trap, as well as the radio frequency evaporation that ensues.

4.2.1 Quadrupole coils

The quadrupole field used for both the 3D-MOT and magnetic trap comprises two pairs of cylindrical coils, located above and below the science cell. The design is based on that presented in [101]. The coils are each wound from $6.35\,$mm-wide, Kapton backed, flat conducting ribbon, with 90 turns per coil. The arrangement is shown in Figure 4.4. Both above and below the cell, the coil pairs are spaced by $2\,$mm. This pairwise design was used to better facilitate cooling through the increased surface area, as typical experimental parameters produce some $500\,$W heat. The coils are mounted within sealed casings, through which cooling water is pumped. The coil design preserves optical access through all seven horizontal, and two vertical windows of the science cell. Currents are provided by a Delta Elektronika SM60-100 supply via an intermediate switch box, to allow for fast switch-off of the field.

The quadrupole arrangement is also surrounded by larger bias coils, which are used to compensate for both the Earth's magnetic field, and the stray fields resulting from the various pumps maintaining the vacuum.

4.2.2 3D-MOT

The 3D-MOT beams enter the science cell through the diagonal ports as shown in Figure 4.5, as seen from above. The couplers for the 3D-MOT are mounted on a motorised translation stage, which allows the MOT optics to be removed after the atoms have been transferred to the magnetic trap. In particular, this frees up subsequent access for the optical dipole traps through the vertical ports.

For the 3D-MOT, a current of $1.7\,\mathrm{A}$ is used in the quadrupole coils, creating a field gradient of $\sim 8.4\,\mathrm{G.cm^{-1}}$. Typical cooling light powers in each of the six beams are $16.0\,\mathrm{mW}$, with a total of $2.5\,\mathrm{mW}$ of repump light coupled in independently. These parameters yield a 3D-MOT of 2–3×10^9 atoms with $7\,\mathrm{s}$ MOT loading. We find the MOT loading to be relatively insensitive to the repump power.

4.2.3 Magnetic trap and radio frequency evaporation

After being cooled in the 3D-MOT, atoms are undergo a compressed MOT phase as described in [75]. We detune the cooling light to $-110\,\mathrm{MHz}$ over $60\,\mathrm{ms}$, and reduce the repump power to $20\,\mathrm{\mu W}$. This results in a peak intensity of $\sim 9\,\mathrm{\mu W.cm^{-2}}$ for a $12\,\mathrm{mm}$ beam waist. The cloud is thereby reduced to a temperature of $\sim 32\,\mathrm{\mu K}$, at which point extinguishing the repump light for $1\,\mathrm{ms}$ allows atoms to populate the $|F = 1, m_F = -1\rangle$ state. The cloud is then transferred into the magnetic trap. The current in the quadrupole coils is ramped linearly over $1.8\,\mathrm{s}$ from the $1.7\,\mathrm{A}$ MOT value to a peak value of $33\,\mathrm{A}$. This corresponds to a field gradient vertically of $165\,\mathrm{G.cm^{-1}}$. We typically capture between 1.5×10^9 and 2.5×10^9 atoms in the magnetic trap, at a temperature of $120\,\mathrm{\mu K}$. The $1/e$ lifetime in the magnetic trap is approximately $180\,\mathrm{s}$ at this temperature.

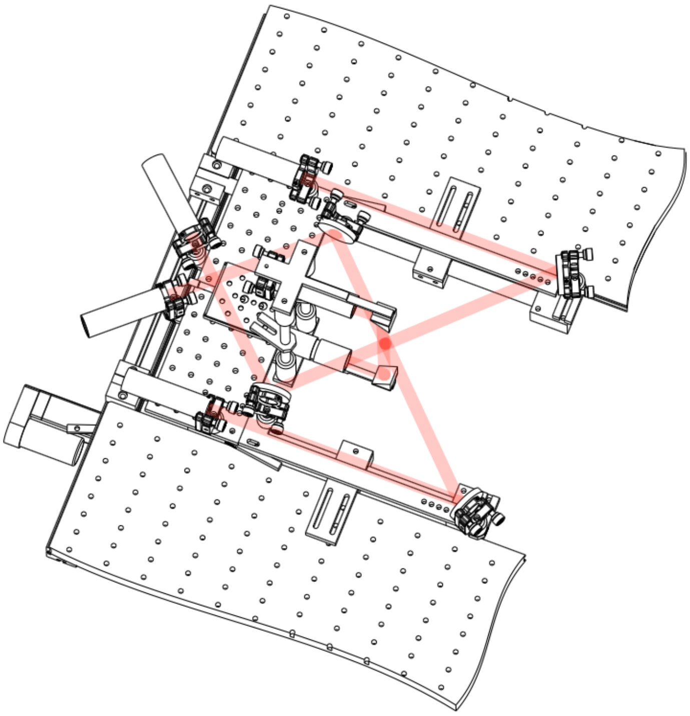

Figure 4.5: 3D-MOT optics, mounted on a motorised translation stage. The science cell is centred at the beam intersection, with the vacuum system extending towards the bottom right of the image. After transfer from the 3D-MOT to the magnetic trap, the MOT optics can be removed by driving the stage back. This permits subsequent optical access for the dipole traps. Image reproduced from [75].

Once trapped in the magnetic trap, RF evaporation follows to further cool the cloud and improve the mode-matching for transfer to the hybrid trap. The antenna used is a circular coil, with a diameter of $40\,\mathrm{mm}$. This was constructed to match the size of the top science cell window, above which the antenna is supported. The RF ramp occurs in two stages, both of which are exponential decays. The frequency is first scanned from $22.00\,\mathrm{MHz}$ down to $3.75\,\mathrm{MHz}$ over $4.0\,\mathrm{s}$, with decay constant $\tau = 1.0\,\mathrm{s}$. The field is then further decreased to $2.00\,\mathrm{MHz}$ over an additional $1.0\,\mathrm{s}$, with decay constant $\tau = 0.3\,\mathrm{s}$. After the full $5.0\,\mathrm{s}$ ramp, we typically have $\sim 1.4 \times 10^8$ atoms at a temperature of $\sim 17.5\,\mu\mathrm{K}$. The $1/e$ lifetime after the evaporation, measured as the decay of atom number, is $115\,\mathrm{s}$, after transfer to the hybrid trap.

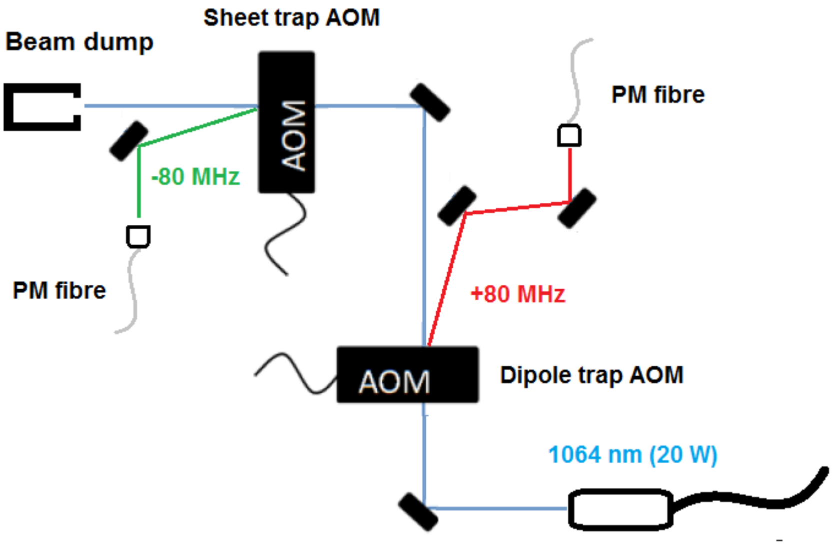

Figure 4.6: The dipole and sheet beams used for optical trapping. Beams are derived from a 1064 nm IPG Photonics YLR-20-LP fibre laser. As the dipole and sheet beams are not needed simultaneously at full-power, the beams are derived from the main laser using daisy-chained acousto-optical modulators. 'PM' denotes a polarisation-maintaining fibre.

4.3 Optical dipole traps

The beams used in both the hybrid (dipole) trap and sheet are derived from a 1064 nm IPG Photonics YLR-20-LP fibre laser, with a maximum power output of 20 W. A schematic representation of the hybrid and sheet beams is shown in Figure 4.6. A separate 1064 nm IPG Photonics YLR-5-LP fibre laser supplies the scanning, vertical beam needed for our time-averaged potentials.

4.3.1 Dipole trap

The main dipole beam is derived from the $+1$ order of an 80 MHz AOM. This is coupled via a polarisation-maintaining fibre into the plane of the atoms, where it is focussed into a beam of $1/e^2$ waist $\sigma_{\text{dip}} = 65\,\mu\text{m}$. The dipole beam propagates horizontally through the science cell, perpendicular to the push beam and feedthrough. The focus of the beam lies approximately σ_{dip} below the zero of the magnetic field used in the hybrid trap. The typical peak power in the dipole beam for transfer from the magnetic trap is 1.5 W. The current in the quadrupole coils is then reduced to $5.6\,\mathrm{A}$, or a gradient of $28.0\,\mathrm{G\,.\,cm^{-1}}$, followed by optical evaporation. When forming a BEC within the hybrid trap, the final beam power is reduced exponentially, typically to $\sim 100\,\mathrm{mW}$. The shape of the combined potential was shown in Figure 2.8, and is essentially harmonic. The calculated trap frequencies for these parameters are $(\omega_x,\ \omega_y,\ \omega_z) = 2\pi \times (78,\ 72,\ 29)\,\mathrm{Hz}$. The weaker confinement along the beam direction is provided by the quadrupole field. We typically capture 22–25 $\times\ 10^6$ atoms in the hybrid trap, and there remain 1–2 $\times\ 10^6$ atoms in a nearly-pure condensate after optical evaporation.

4.3.2 Sheet beam

The sheet beam is derived from the same laser as the dipole beam, using the daisy-chained AOM arrangement shown in Figure 4.6. After coupling into the atom plane via a polarisation-maintaining fibre, the beam is expanded cylindrically from a $2\,\mathrm{mm}$ diameter beam in an $M = 5$ telescope. The telescope comprises an $f = -30\,\mathrm{mm}$, and an $f = 150\,\mathrm{mm}$ cylindrical lens. After expansion, the beam is focussed into the science cell with an $f = 250\,\mathrm{mm}$ cylindrical lens. This yields measured waists of $\sigma_y = 23\,\mathrm{\mu m}$ in the vertical direction, and $\sigma_x = 1.50\,\mathrm{mm}$ horizontally, perpendicular to the beam's propagation direction. While the sheet power used is variable, the trapping frequency vertically is typically of order $\omega_y = 2\pi \times 110\,\mathrm{Hz}$.

4.3.3 Scanning beam

The formation of the scanning beam, derived from a $1064\,\mathrm{nm}$ IPG Photonics YLR-5-LP fibre laser, is shown in Figure 4.7. The beam then passes through an IntraAction DTD-274HA6 two-dimensional acousto-optical deflector (2D-AOD), with transmission optimised for the (+1,-1) order. Expansion with an $M = 3$ telescope, and subsequent focussing into the science cell with an $f = 200\,\mathrm{mm}$ achromatic lens yields a beam waist of $26.5\,\mathrm{\mu m}$.

The 2D-AOD comprises two crossed crystals of TeO_2. To one face of each crystal is attached a piezoelectric device, which is driven at radio frequencies centred at $27\,\mathrm{MHz}$.

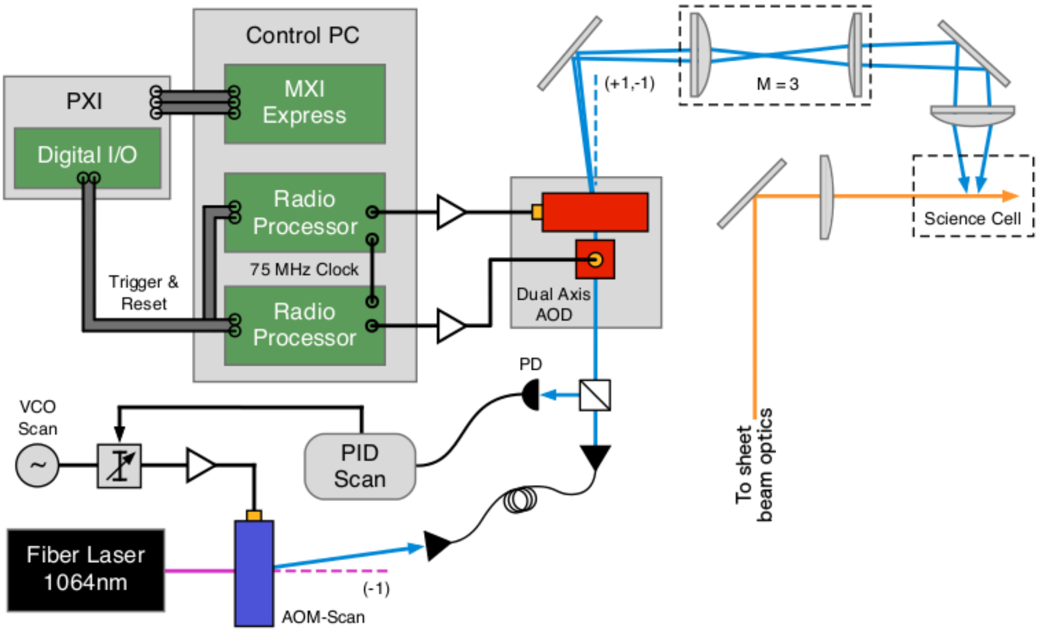

Figure 4.7: Optics and electronics required to generate the scanning vertical beam. An IPG Photonics YLR-5-1064-LP laser is used as the source, operating at 3.8 W, and with the intensity stabilised using a feedback circuit. The beam then passes through a 2D acousto-optical deflector (IntraAction DTD-274HA6), with each axis independently driven by separate amplified signals from PCI-based RF cards (SpinCore RadioProcessor). The (+1,-1) order of the 2D-AOD is isolated with an iris, magnified by a factor of $M = 3$, then focussed into the plane of the sheet beam. Image adapted from [1].

This generates sound waves within the crystals, from which the incident laser diffracts. The grating spacing along each axis, and hence the diffraction angle in that direction, is controlled by the frequency of the sound waves propagating within the crystals. Consequently, the diffracted orders can be made to trace out patterns by carefully controlling the driving frequencies of the piezoelectric devices. The maximum speed at which the beam's deflection angle can be altered is limited by the AOD's access time. This is the time taken for an acoustic wave to traverse the beam waist within the crystal. For our parameters, this is $\sim 5\,\mu\text{s}$, limiting the speed with which we can alter the beam location to $\sim 20\,\text{kHz}$.

4.3.4 Intensity stabilisation

The trapping parameters of the optical traps can vary significantly with the beam power. Despite the use of polarisation maintaining fibres, day-to-day fluctuations can result in non-negligible drifts of the polarisations. This, when coupled with polarisation-selective elements in the beam paths, manifests as variations in the overall beam intensity. Each of the dipole, sheet, and scanning beams are therefore locked using sampling beam cubes, which direct a small fraction of the beam's power onto a photodiode. The photodiode signals are used in a proportional-integral (PI) feedback circuit, which modulates the RF driving power of the AOMs generating the beams, stabilising their intensities. The relevant circuit is included in Appendix B.

4.4 Imaging

In our experiment, we are able to image along two axes. One axis runs horizontally through the chamber, while the second runs vertically through the centre of the chamber. We use two different sets of optics for these axes. The horizontal imaging employs an $f = 150\,\mathrm{mm}$ lens in the $2f$–$2f$ arrangement, as we saw in Figure 2.12 in chapter 2. This provides 1:1 images of the atoms in the cell, and is useful for imaging the atoms at early stages of trapping, including the magnetic and hybrid traps, prior to the final optical evaporation.

The vertical imaging geometry is shown schematically in Figure 4.8. As the interesting structure of potentials we are able to generate is within the horizontal plane, this plane contains most of the interesting detail. The vertical axis therefore makes use of a specifically designed compound objective lens, in conjunction with an $f = 300\,\mathrm{mm}$ achromatic relay lens. The arrangement provides a magnification of $f_{\mathrm{relay}}/f_{\mathrm{objective}} = 6.38$.

The compound lens used in the vertical imaging is based on the design presented in [121], and is formed from commercial Thorlabs lenses. The lenses are mounted within a

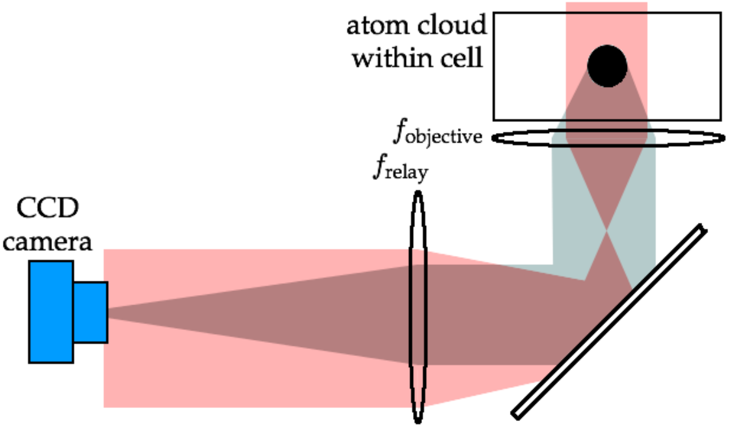

Figure 4.8: Imaging geometry for the vertical imaging used in our experiment. The probe laser beam is shown here in red. The imaging along this axes employs an objective–relay configuration of lenses. The objective is an $f = 47\,\text{mm}$ compound lens based on the design of [121], which corrects for imaging aberrations, and compensates for the thickness of the science cell window. The relay lens is a $f = 300\,\text{mm}$ achromatic lens. The arrangement offers a magnification of $f_{\text{relay}}/f_{\text{objective}} = 6.38$.

section of PVC tube, with machined aluminium rings spacing the lenses within the tube. The PVC tube resides within the lower quadrupole coil, with the vertical 3D-MOT beam transmitted through the back of the compound lens into the science cell. The aluminium spacing rings have each had a small section cut out of them, to prevent eddy currents during the switch off of the magnetic field. The lens combination is optimised for $780\,\text{nm}$ light, to suit the cooling transition used for imaging. When tested outside the main system, the lens was found to have a resolution limit of $1.6\,\mu\text{m}$. This was determined by focussing the image of a $1\,\mu\text{m}$ diameter pinhole through the lens onto a camera. The image is shown in Figure 4.9. The pinhole was known to be smaller than the objective's resolution limit, and so the pinhole serves as a point source. The radial intensity profile of the image on the camera is then described by an Airy function, with the resolution limit being the radius of the central Airy disc.

The compound lens is mounted on a translation stage driven by a controllable stepper motor, which allows the lens position to be varied vertically. Our data are taken with various times-of-flight, during which the condensate falls under gravity. Over $25\,\text{ms}$, the

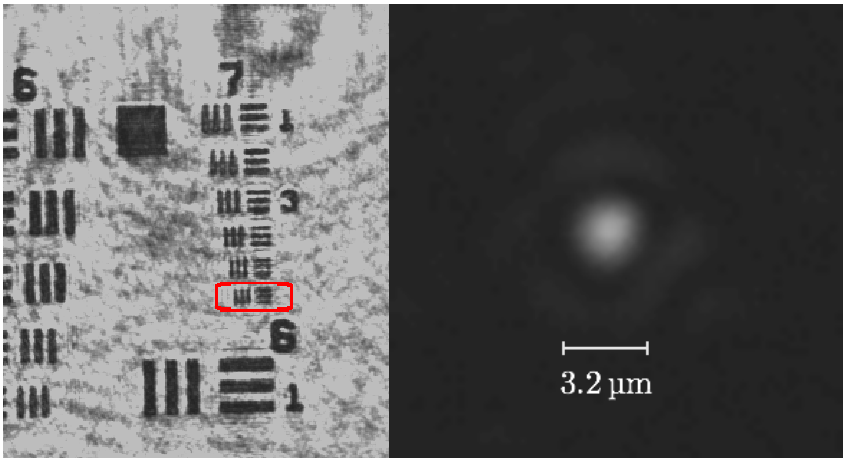

Figure 4.9: Resolution of the compound lens. *Left*: An image of the 1951 USAF resolution test chart, taken through the compound lens, and further magnified with a commercial 10× Olympus PlanApo microscope objective. Images were taken through a test window of thickness 4.0 mm, to match the thickness of the windows in the science cell. The smallest line pairs here, marked with a rounded box, are 2.2 µm wide. They are separated by a distance equal to their width. These line pairs are clearly resolvable, demonstrating that the resolution limit is below 2.2 µm. *Right*: The image of a 1 µm diameter pinhole taken through the same setup, but with a 20× Olympus PlanApo microscope objective. This pinhole is not resolvable by the lens, and so the radius of the central Airy disc is used to identify the resolution limit of 1.6 µm. This is in good agreement with the 1.5 µm predicted theoretically.

condensate falls through a distance of $\sim 3\,\mathrm{mm}$. This would result in a dramatically out-of-focus image using our compound lens, with the high resolution coming at the cost of having a narrow depth of focus. The ability to translate the lens vertically allows us to image the condensate in trap, and at times of flight up to $\sim 30\,\mathrm{ms}$. The accessible times-of-flight are further increased through use of a levitating magnetic field, which will be discussed in the following section.

For both the horizontal and vertical imaging arrangements, the image of the atoms is focussed onto a CCD camera. We use ProSilica EC1380 cameras for both axes, which have square pixels with side lengths of 6.45 µm. This renders structures smaller than 6.45 µm unresolvable with the horizontal imaging. The 1.6 µm resolution limit of the compound lens is theoretically achievable with the vertical imaging, after accounting for the 6.38× magnification.

4.5 Magnetic levitation

To enable us to access later times-of-flight after release from the trap, we have implemented a magnetic levitation scheme. Desirable traits in a levitation field include a vertical gradient sufficient to support against gravity, i.e. $\sim 30.5\,\mathrm{G.cm^{-1}}$, and simultaneously very weak (or no) confinement in the horizontal plane, so as to negligibly affect the cloud's expansion dynamics. This can be achieved by driving the two quadrupole coils in Figure 4.4, i.e. the upper and lower coils, with independent currents, while simultaneously applying a bias field in the vertical direction, which serves to shift the magnetic field zero.

An external switch box reroutes the top coil pair of the quadrupole field to be driven by a second Delta Elektronika ES-30-10 power supply, independently of the bottom coil pair. The bottom coil pair remains connected to the original supply. Currents continue to flow in the anti-Helmholtz directions, but with the current in the top coil roughly $40\,\%$ of that in the bottom coil.

While the atoms remain trapped optically, a small bias field is applied. This defines a quantisation axis, which keeps the atoms in the $F = 1, m_F = -1$ spin state. As the field is uniform, however, it does not otherwise influence the atoms. Without the bias field, the atoms held in the trap form a spinor BEC, with populations distributed among the different degenerate m_F states. While this can be useful for interferometric applications, it precludes levitation, as the different spin states interact with an applied $\mathbf{B}$ field with varying strengths.

After releasing the atoms from the optical trap, they begin to expand, and fall under gravity. In the first $5\,\mathrm{ms}$, the levitation field is ramped up to a peak value, which slows the atoms to a stop. The field is then reduced to only provide support against gravity. The experimental current profiles are shown in Figure 4.10. The final field parameters are $10.5\,\mathrm{A}$ in the bottom quadrupole coil, $4.12\,\mathrm{A}$ in the top quadrupole coil, and $8.5\,\mathrm{A}$ in the

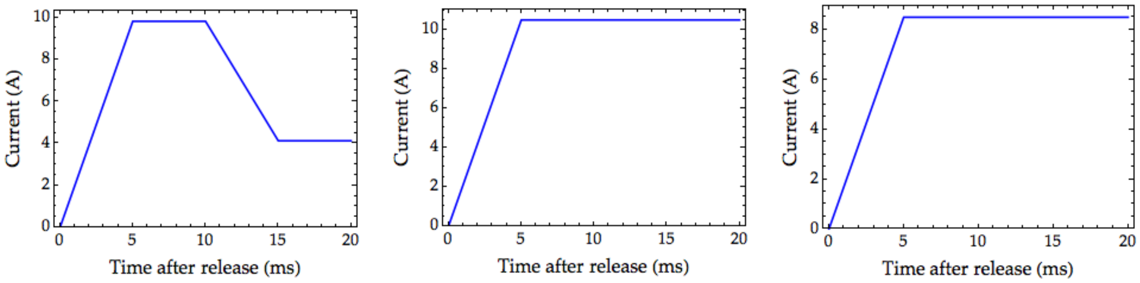

Figure 4.10: Current profiles used for the levitation scheme employed in our experiment. Currents are shown for the top quadrupole coil (*left*), bottom quadrupole coil (*centre*) and bias field coils (*right*). The 'hump' shape of the top coil profile serves to initially catch the falling atoms, then finally to support them against gravity once their velocity reaches zero.

bias field coils. The bias field at these currents provides an offset of $65\,\mathrm{G}$. The calculated field profile with these parameters is shown in Figure 4.11. These parameters result in the atoms being levitated at the equivalent of $14\,\mathrm{ms}$ time-of-flight below the trap, which is readily accessible with our compound lens. Expansion times in excess of $100\,\mathrm{ms}$ are accessible with this technique.

4.6 Single- and double-Bragg diffraction

Following [122], our setup also incorporates a Bragg diffraction scheme for our condensates. This can be used to study the momentum distribution within the condensate, but also as a means of creating atomic beamsplitters for separating, and subsequently recombining the different arms of a Mach-Zehnder-style atom interferometer. The geometry is shown in Figure 4.12, and the technical details of our setup are presented in [123].

The source laser for the Bragg arrangement is a Toptica DL-100 diode laser, locked to the ^{85}Rb $F = 2$ line. The detuning of the two beams from one another is controlled with two AOMs, driven by separate supplies that use the same reference clock. Atoms in the cloud absorb a photon from one beam, and reemit back into the other, gaining momentum $\mathbf{q}$,

$$|\mathbf{q}| = 2\hbar k \sin(\tfrac{\theta}{2}) \;, \tag{4.1}$$

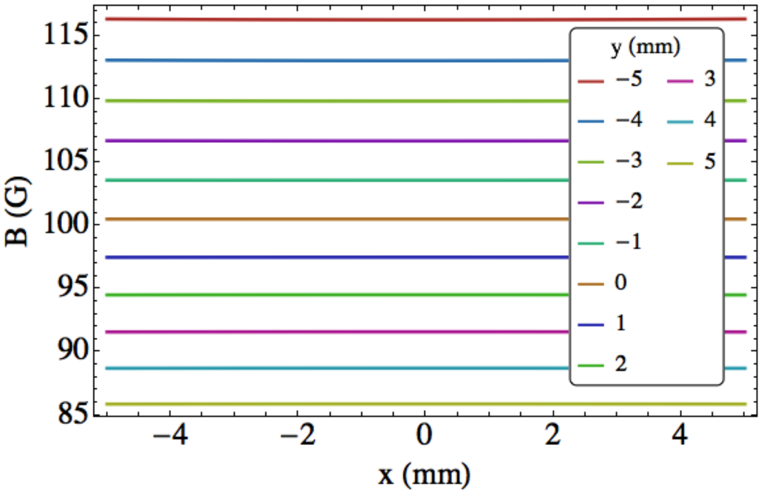

Figure 4.11: Theoretical field profile for the levitation scheme employed in our experiment. The field is radially symmetric, and so is equally flat in the z direction. The even spacing of the contours shows the uniform gradient in the y direction, equal to $30.5\,\mathrm{G.cm}^{-1}$. Image courtesy T. Bell.

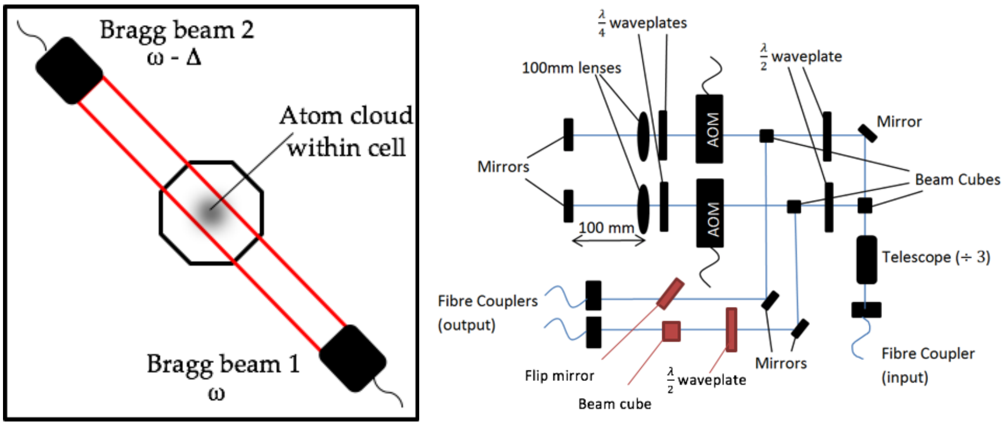

Figure 4.12: *Left*: Geometry of our single- and double-Bragg arrangement, viewed from above. The frequency difference Δ between the two beams determines the momentum transferred to the cloud. *Right*: Laser arrangement for creating the Bragg beams. Two separate AOMs control the frequency difference between the two beams, which governs the momentum transferred to the cloud. The AOMs are driven by RF generators that use the same reference clock for frequency stability. Introducing the flip mirror, and retro-reflecting the lasers in-situ, allows us to convert the arrangement between single- and double-Bragg. Image adapted from [123].

where $\theta = \pi$ for our setup. The detuning required must satisfy conservation of energy, which gives

$$\hbar\Delta = \frac{(2\hbar k)^2}{2m} = 2\pi\hbar \times 15.08\,\text{kHz}\ , \tag{4.2}$$

using k for the $780\,\text{nm}$ light we use. The population of the $|+2\hbar k\rangle$ state varies sinusoidally in time with the effective Rabi frequency,

$$\Omega_{\text{eff}} = \frac{\Omega^2}{2\delta}\ , \tag{4.3}$$

where Ω is the Rabi frequency for the two-level transition introduced in chapter 2, and δ is the shift of the laser frequency from the atomic resonance. Precise control over the pulse length therefore results in control over the populations of the two momentum states.

The single-Bragg arrangement transfers momentum to the cloud in a single direction, whereas double-Bragg, as the name suggests, creates symmetric splitting of the atoms between the $\pm 2\hbar k$ modes. This is realised by superimposing a second Bragg arrangement, with orthogonal polarisation to the first. Our implementation of the double Bragg scheme introduces the red elements in Figure 4.12 to achieve this. With one coupler now not in use, we attach a wave plate and mirror onto it, instead retro-reflecting the beam from the other coupler to create our double-Bragg grating.

Chapter 5

Performance and applications

A key achievement early in my candidacy was the first production of a BEC with our apparatus. In this section we shall provide experimental evidence of BEC creation within our hybrid magnetic and optical trap. We will then detail our creation of time-averaged potentials, bringing together the individual experimental elements introduced in the previous chapter. The evolution of our feedforward technique, from light-only feedforward through to time-of-flight feedback will be presented here. The implications of typical atom numbers and temperatures obtained with our final technique will be discussed, in terms of phase coherence. The chapter closes with with preliminary applications of the ring trap, including probes of coherence, and the generation of acoustic waves.

5.1 Signatures of BEC

There are a number of ways in which we can identify the successful creation of a condensate. One of these hallmarks is the asymmetric expansion introduced in §3.3, which we have observed in our experiment. After optical evaporation in the hybrid trap, we release the condensate from the trap. It expands, simultaneously falling under gravity. Imaging from below, we observe the aspect ratio inversion, from cigar- to pancake-shaped. The sequence is shown in Figure 5.1.

An additional signature of BEC is the emergence of a bimodal distribution in the optical

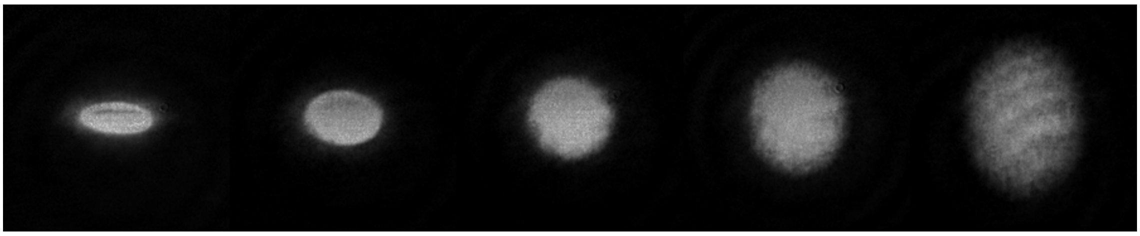

Figure 5.1: Assymmetric expansion of the condensate after release from the hybrid trap. Each frame is a 202 µm×202 µm square, imaged from below the science cell. The dipole beam runs from right to left in the images shown here. Images were taken at 1 ms, 6 ms, 10 ms, 14 ms, and 20 ms after release from the trap, from left to right. The 1 ms image shows the trap aspect ratio, with tighter confinement perpendicular to the dipole beam, and weaker confinement along the beam provided by the quadrupole magnetic field.

density. This comprises a broader, thermal component, with a narrow condensate peak rising from the centre, as seen in Figure 5.2. Using an image of the BEC, taken from below the trap, we can identify that the profile comprises the sum of thermal and condensed components. There is a clear deviation from the Gaussian profile we would otherwise expect for a thermal cloud. The thermal component's $1/e^2$ waist is (103.7 ± 1.5) µm, with the uncertainty estimate arising from the fit parameter statistics. The trapping frequency along this dimension is $\omega_z = 2\pi \times 29\,\mathrm{Hz}$, and using the $10\,\mathrm{ms}$ time-of-flight after expansion, we find a cloud temperature of $(217 \pm 6)\,\mathrm{nK}$. This is consistent with the findings of NIST's experiment [101], on which our apparatus is based, and which employs similar trapping parameters. The NIST group found the onset of condensation to occur at a temperature of $(320 \pm 50)\,\mathrm{nK}$.

5.2 Time-averaged optical ring traps

Our time-averaged ring trap is formed at the intersection of the sheet and scan beams described in §4.3. The ring geometry we wish to form is discretised into a set of points on the circumference. Each of these points corresponds to a pair of driving frequencies (f_x, f_z) for the x and z axes of the 2D-AOD. By driving the two axes at their respective

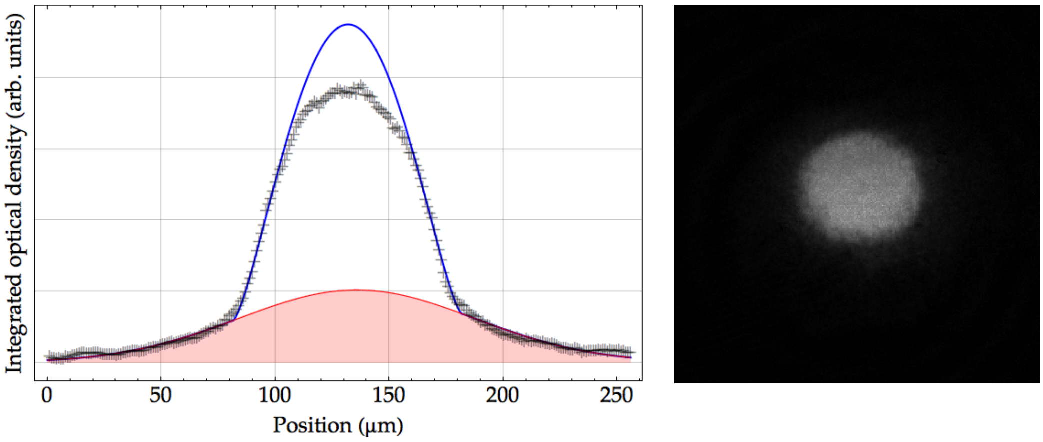

Figure 5.2: Bimodal distribution of atoms between thermal (red) and condensed (blue curve) phases. The optical density is integrated along the vertical direction, and the graph domain matches the size of the image provided at the right. Data points with optical densities higher than 2.0 have been excluded from the fit, as these correspond to light levels too low for the camera to detect. The removal of these data is the source of the discrepancy between the blue curve and the higher experiment data points. The extracted $1/e^2$ waist of the thermal component is (103.7 ± 1.5) µm, yielding an estimated temperature of (217 ± 6) nK.

frequencies, we can steer the scan beam to the corresponding position on the ring circumference. In theory, a maximum separation of points of $0.7w_\rho$, where w_ρ is the scan beam waist, should suffice to form a corrugation-free ring. This concept is illustrated in Figure 5.3. Our initial realisation spaces the beams by this amount, while the final realisations instead use $0.65w_\rho$, which we have found to give smoother traps.

We cycle the beam position through the points on the ring circumference by varying the driving RF frequencies. Control over the depth of the potential at each location is afforded by varying the corresponding amplitude. Both the frequency and amplitude are controlled by a pair of SpinCore RadioProcessor cards, each driving one axis of the 2D-AOD. The cards operate from a common $75\,\text{MHz}$ clock, which prevents the two axes of the 2D-AOD becoming asynchronised. The speed at which we can alter the frequencies without adversely affecting the potential through blurring or smearing effects is limited by the 2D-AOD's access time. The 2D-AOD employed uses the shear mode for sound wave propagation, which gives an access time of $1.6\,\mu\text{s}\,.\,\text{mm}^{-1}$ beam diameter. We use a $2\,\text{mm}$ beam, which restricts us to $\sim 3.2\,\mu\text{s}$ switching speeds. In practice, we have used a

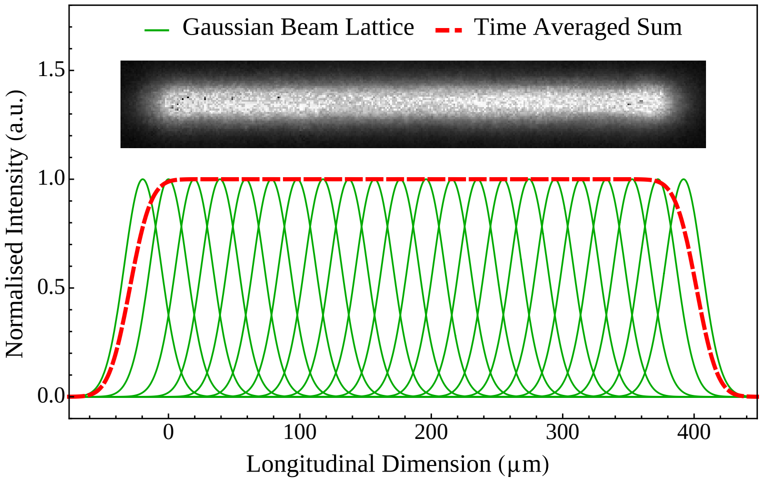

Figure 5.3: Formation of a smooth potential using overlapped gaussian beams. Green and red curves show the calculated intensity profiles of the laser, while the grayscale inset is an absorption image of atoms held in-trap. Each of the individual beam profiles, shown in green, is spaced by $0.7w_\rho$, where w_ρ is the $1/e^2$ waist of the beam. Averaged over the 22 points shown, the dashed, red potential is formed. *Inset*: A to-scale image of a condensed cloud of ^{87}Rb atoms held within the time-averaged line trap. Image reproduced from [1].

switching speed of $5\,\mu\text{s}$ in this work.

5.2.1 Determination of beam waist

The difficulty associated with exactly overlapping the focii of the sheet and scanning beams makes it difficult to determine the effective waist of the beam at the location of the atoms. To determine a meaningful estimate of the waist, we use the parametric heating techniques introduced in §2.4.6.

We have loaded atoms into a crossed configuration with the sheet, and a red-detuned pin beam for radial confinement, of waist $w_{\rho,\text{geo}} = (26.5 \pm 0.6)\,\mu\text{m}$, as presented in §4.3. We modulated the beam intensity by $10\,\%$ sinusoidally, with varying frequency, and measured the number of atoms that remain trapped after the modulation. Plotting this number as a function of the modulation frequency, we have identified the locations of the $\nu = 2\omega$ resonance peaks for the corresponding power. This process was carried out twice, for mean powers of $0.65\,\text{mW}$ and $2.26\,\text{mW}$. The trapping frequencies in the x-z plane

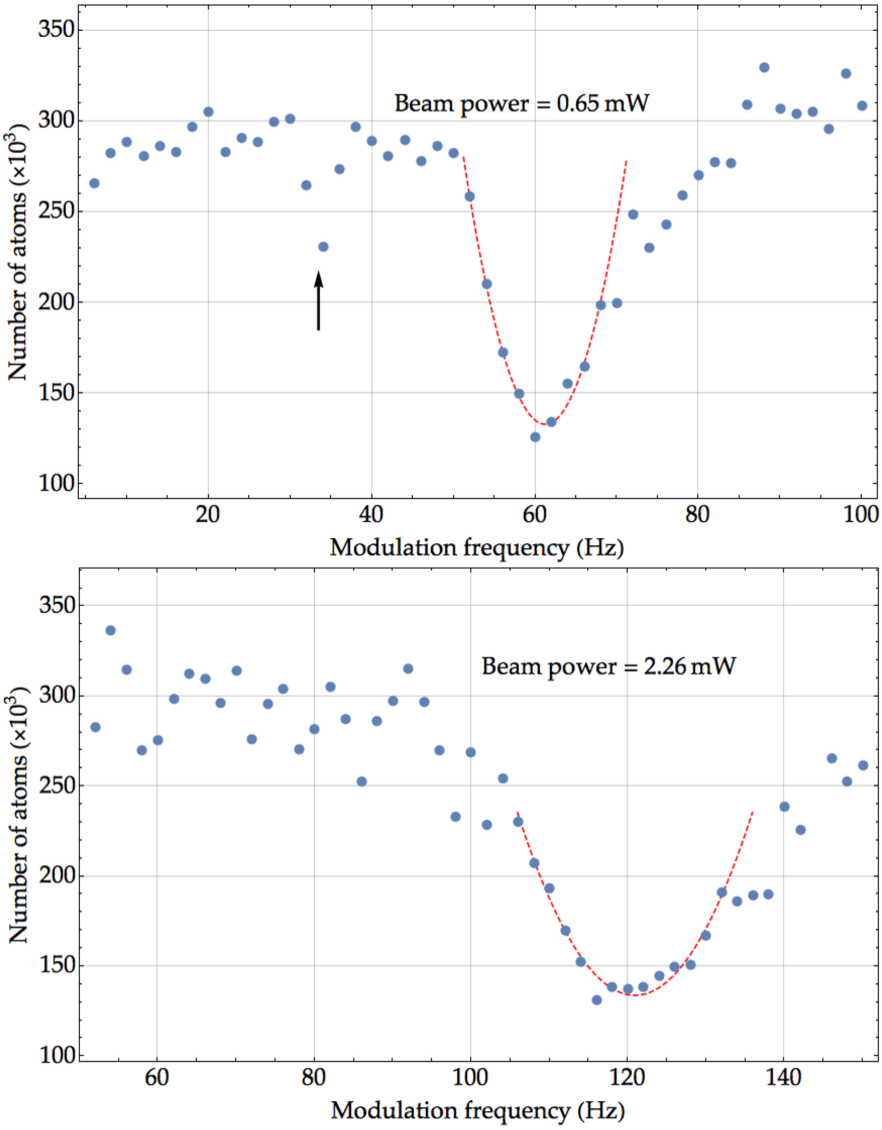

Figure 5.4: Parametric heating of thermal atom clouds in the crossed sheet and vertical pin beam. Data are shown for pin beam powers of $0.65\,\mathrm{mW}$ (above) and $2.26\,\mathrm{mW}$ (below). Parabolic fits to points around the minima are used to identify the centres of the resonances. $2\omega = 2\pi \times (61.20 \pm 0.17)\,\mathrm{Hz}$ for the lower power, while $2\omega = 2\pi \times (120.9 \pm 0.3)\,\mathrm{Hz}$. Uncertainties are extracted from the fit statistics. The black arrow in the top plot marks the position of a small resonance when driven at ω itself, though the parametric enhancement is not present when driving at ω.

obey

$$\omega_\rho^2 = \frac{8KP}{m_{\mathrm{Rb}}\pi w_\rho^4}\,, \tag{5.1}$$

with $K = 1.857 \times 10^{-36}\,\mathrm{m}^2\,.\mathrm{s}$, as shown in §2.2.3, P is the beam power, and w_ρ is the $1/e^2$

waist of the scanning beam. The aforementioned beam waist was then determined by

$$w_\rho = \left[\left(\frac{P_2 - P_1}{\omega_\rho^2(P_2) - \omega_\rho^2(P_1)} \right) \frac{8K}{\pi m_{\mathrm{Rb}}} \right]^{1/4} , \tag{5.2}$$

to give the quoted $w_\rho = (26.5 \pm 0.6)\,\mu\mathrm{m}$. This approach was taken as the ratio of the square roots of powers is lower than the ratio of trapping frequencies, while (5.1) implies they should be equal. The approach taken here reflects this discrepancy in the uncertainty on the waist estimate. [82] attributes similar changes in the beam waist to shifts in the focus location due to thermal effects in the driving AOM, and in our case, the 2D-AOD. The experimentally obtained value is in agreement with the result expected geometrically, when focusing a $d = 6\,\mathrm{mm}$ beam of $1064\,\mathrm{nm}$ light through an $f = 200\,\mathrm{mm}$ lens, namely

$$w_{\rho,\mathrm{geo}} = \frac{2\lambda}{\pi} \cdot \frac{f}{d} , \tag{5.3}$$

which gives $w_{\rho,\mathrm{geo}} = 22.6\,\mu\mathrm{m}$. The larger experimental waist is consistent with the introduction of spherical aberrations, and clipping of the beam on the optics used to image the pin beam into the plane of the atoms.

Using the experimental value for the waist, we can identify the radial trapping frequencies for particular combinations of ring radius, and pin beam power. In a flattened ring, we expect the radial trapping to match the beam's profile, so that

$$I(\rho) = I_0 \exp\left(-\frac{2(\rho - \rho_0)^2}{w_\rho^2} \right) . \tag{5.4}$$

The peak intensity I_0 is determined by fixing the total power, i.e.

$$I_0 = \frac{P}{2\pi} \left[\int_0^\infty d\rho\, \rho\, \exp\left(-\frac{2(\rho - \rho_0)^2}{w_\rho^2} \right) \right]^{-1} . \tag{5.5}$$

The trapping frequencies are then given by (2.43). These frequencies are plotted for a selection of ring radii in Figure 5.5.

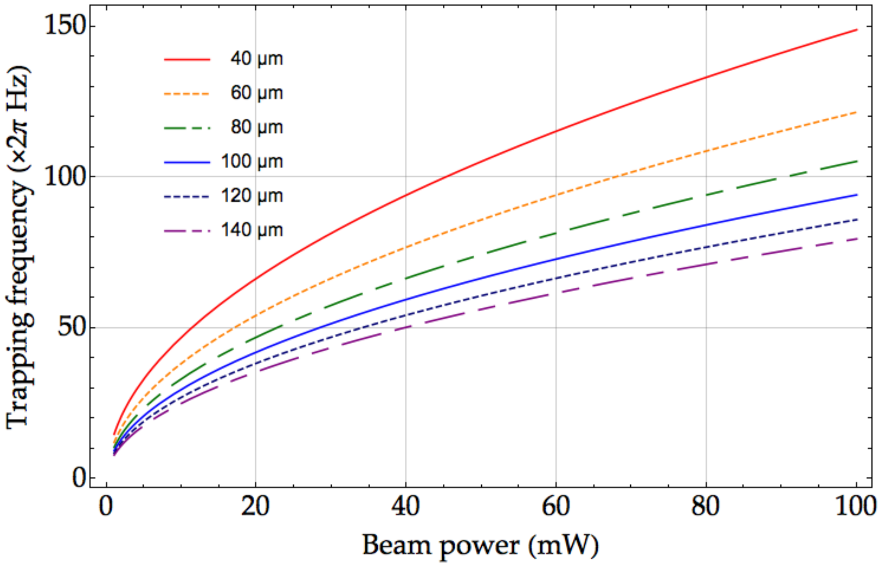

Figure 5.5: Trapping frequencies in the ring as a function of input beam power. As the trap area in the x-z plane increases with larger rings, the intensity is reduced for the same power. These radii and powers encompass the range of values used in our experiments, with the earlier rings using slightly higher trapping frequencies of $2\pi{\times}50$–$70\,\mathrm{Hz}$, and later traps using frequencies of $2\pi{\times}{\sim}\,35\,\mathrm{Hz}$.

5.2.2 Uncorrected ring trap

Loading into an optical trap generated without first applying any corrections yields uneven occupation of the rings with angular displacement. In the initial realisations of our ring traps, loading was achieved by first forming a BEC in the hybrid trap. The BEC was then transferred into the sheet beam, and held in place in the horizontal plane by a static pin beam, generated by the 2D-AOD. The sheet and pin beams were aligned such that their centres overlapped with the BEC in the hybrid trap. The pin beam location (i.e. pair of frequencies) is preprogrammed into registers on the SpinCore cards, along with a second segment of the sequence. The second segment waits for a hardware trigger, after which the pin beam is replaced with a rapidly scanned ring, around which the BEC would then expand. This is represented visually in Figure 5.6. The RF power used for each beam location on the ring is fixed, initially, using a constant peak-to-peak voltage of $0.7\,\mathrm{V}$ from the SpinCore cards. A lower driving voltage of $0.3\,\mathrm{V}$ was used for the initial pin beam, to better match the trapping frequencies between the ring trap, and the crossed sheet and pin.

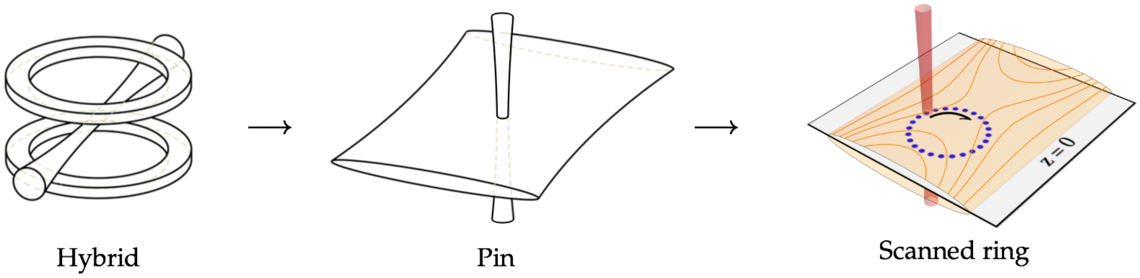

Figure 5.6: Loading process for the initial rings. In our original ring traps, we first evaporated to condensate in the hybrid trap. The transition from the hybrid to the pin then followed adiabatically. The pin to ring transition is, however, not adiabatic. In the scanned trap, the vertical beam cycles through each of the blue locations marked, spending $5\,\mu\mathrm{s}$ at each point. The vertical beam for the 'pin' stage is initially located at the position shown at the right, relative to the ring. The scanned ring also shows contours representing the shape of the sheet potential.

Figure 5.7 shows an example of a ring formed in this manner, after holding the condensate in the ring for several seconds to reduce excitations. For smaller rings of radii $\sim 35\,\mu\mathrm{m}$, we obtain non-uniform angular distributions, while for larger rings, the condensate doesn't fully occupy the ring. It is instead localised to a segment, or several segments, of the ring that correspond to the lowest points in the potential. These variations in the density around the ring arise primarily due to differing beam intensities at each point on the ring, and the rolloff of the optical trap produced by the sheet beam. The distribution shown in Figure 5.7 has decreased density at the top and bottom of the ring, where the sheet beam intensities are lower.

5.2.3 Light-based feedforward

One key candidate for the uneven distribution of atoms around the ring is the 2D-AOD's diffraction efficiency. The efficiency of the diffraction varies as a function of the two driving frequencies, as well as the driving RF powers. The sigmoidal dependence of the diffraction efficiency of the 2D-AOD on peak-to-peak driving voltage is shown in Figure 5.8. Our first attempt to correct the potential mirrors the approach taken in [74]. We temporarily restrict our focus to the potential itself, and image the light directly onto the

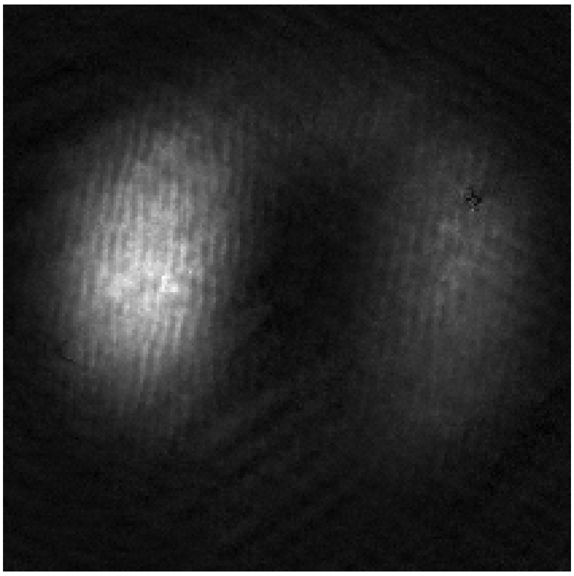

Figure 5.7: $50\,\mu\mathrm{m}$ radius ring generated as a time-averaged potential, before the application of any feedforward corrections. Atoms can be seen to be pooling at the left and right sides of the ring, with little occupation in the top and bottom sections. This atom distribution is consistent with the potentials shown in §2.4.4, with atoms collecting in the centre of the intersecting sheet beam. These atoms remain thermal, as the limited quality of the trap precludes evaporation to BEC.

camera at low incident power. These images of the light itself showed variations in the intensities spatially, and so our first feedforward technique aimed to address this variation in order to flatten the rings.

The light exiting the 2D-AOD was focused onto a photodiode, before it passed through subsequent optics and into the science cell, and the voltage measured over several cycles of the ring. Periodic variation in the measured voltage shows the non-uniformity as a function of angle around the ring. The monotonic nature of the 2D-AOD response to the driving voltage permits the use of a proportional-type feedforward technique to remove these variations. As we were operating at driving voltages of $\sim 0.7\,\mathrm{V}$, corresponding to near-maximum diffraction efficiency, it is necessary to reduce the beam power of each contributing point to match that of the minimum. Figure 5.9 shows representative traces of the photodiode voltage both before and after implementing the feedforward correction.

The correction of the potential for the 2D-AOD's diffraction efficiency yields significant

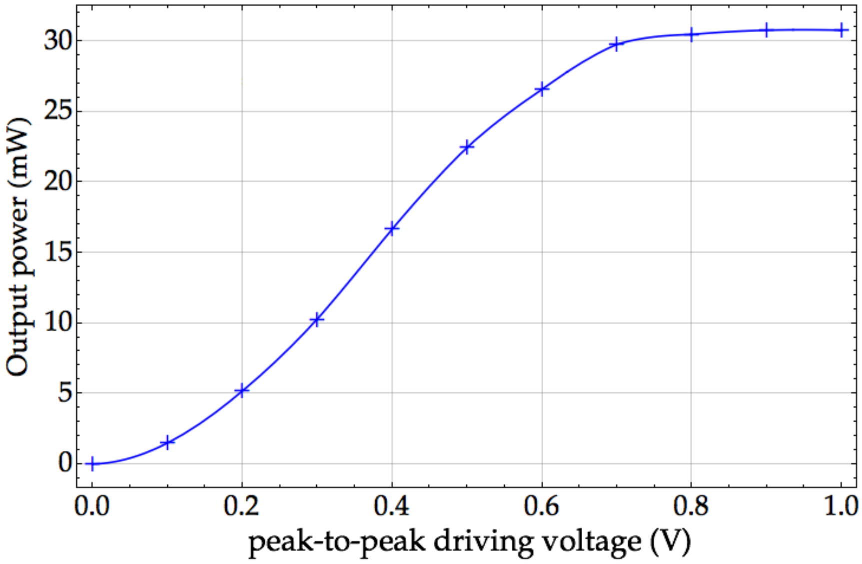

Figure 5.8: Sigmoidal response of the 2D-AOD diffraction efficiency to the peak-to-peak driving voltage. The blue curve shown is an interpolation of the data, and serves only to guide the eye. The piezoelectric elements in the 2D-AOD are driven by amplified RF signals from two SpinCore RadioProcessor PCI cards. The peak-to-peak voltage output of these cards is a maximum of $1.00\,\mathrm{V}$, and the gain of the amplifiers is chosen to maximise our control over the diffracted power through the SpinCore voltages. The response is monotonically increasing between $\sim 0.10\,\mathrm{V}$ and $\sim 0.70\,\mathrm{V}$ with our parameters, and is nearly linear over this region. This permits proportional feedforward control to achieve desired intensities within this range of voltages.

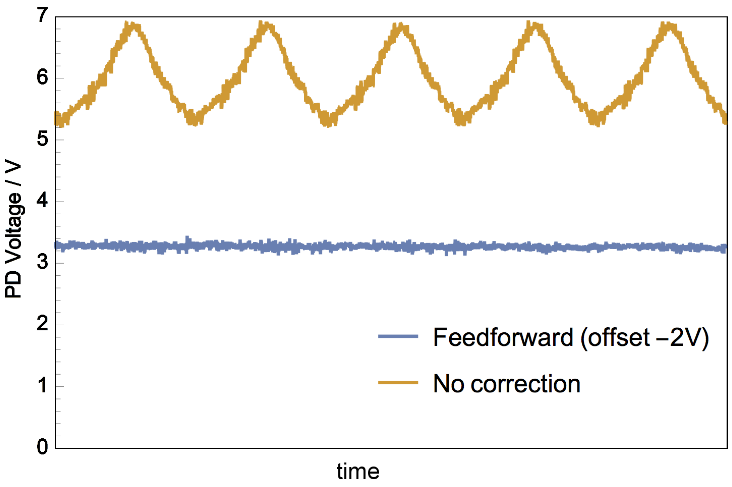

Figure 5.9: Oscilloscope trace of the scanning ring potential. In the uncorrected case, shown here in orange, the measured voltage can be seen to vary periodically. This arises from the dependence of the 2D-AOD's diffraction efficiency on the driving frequency. By measuring each beam location independently, and adjusting the driving frequency of the 2D-AOD accordingly, we can achieve a flatness of the optical potential of less than $2\,\%$. The periodicity is consistent with the scan speed used.

improvement in the quality of the ring traps. With this technique alone, we were able to create rings of radii $\sim 50\,\mu\text{m}$, which showed significant improvement in the distribution of atoms around the ring. A typical example is shown in Figure 5.10. Despite the marked improvement, however, rings corrected in this manner still show variations in density of over $50\,\%$ around the ring, and typically display low condensate fractions. Moreover, the condensed atoms preferentially occupy the deeper parts of the potential, resulting in 'pockets' of condensed atoms within an otherwise thermal ring.

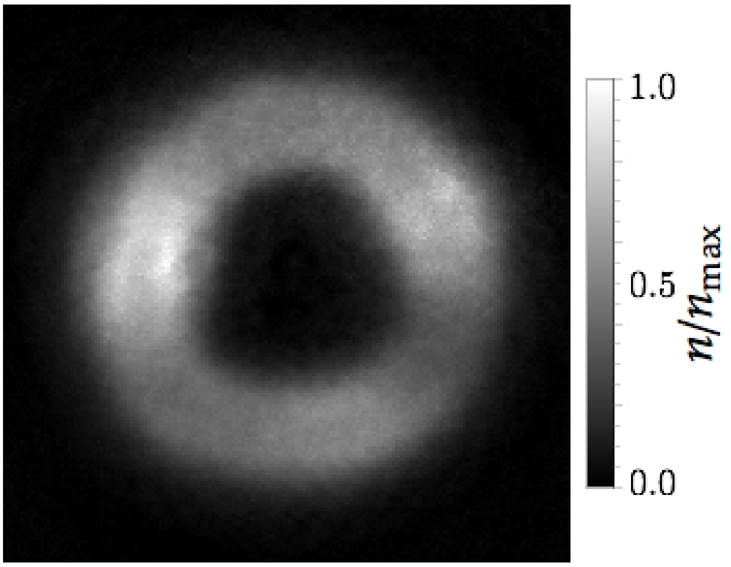

Figure 5.10: Ring trap produced after feedforward on the optical intensity. The ring has a radius of $50\,\mu\text{m}$, and contains 4.5×10^5 atoms. While the ring generated by these means shows marked improvement over the uncorrected ring, the density variations are still significant. The bottom-right segment, in particular, remains at $\sim 25\,\%$ of the density at left.

5.2.4 Atom-based feedforward

A much improved result can be obtained by instead using the atom density itself as the signal for a feedforward algorithm. To do this, the locations of atoms in the ring must be accurately cross-referenced with the corresponding beam positions. Applying a gaussian filter of $25\,\mu\text{m}$ width to the optical density smooths features smaller than the beam waist. Subsequent application of an edge detection to this smoothed image yields contours of the inner and outer ring radii. Figure 5.11 shows the identified contours. Performing least-squares fits of these edge coordinates to a circle gives the location of the ring centre, and the measured radius of the ring, in terms of camera pixel coordinates.

We must also determine the azimuthal coordinate of each beam location. Any rotational offset, which may arise from a slight angle between the 2D-AOD and camera orientations, cannot be determined from an image of the ring, as the beam overlap removes corrugations. The angular offset is instead calibrated by scanning a straight line, with one axis 2D-AOD driven at a fixed frequency. The angle this line forms with the horizontal completes the mapping.

Summing the optical densities in angular bins centred on each beam location gives the angular profile. The variations of each bin value from the mean density constitute the signal used in proportional feedforward for the subsequent realisation. We determine the density fluctuations relative to the mean,

$$\chi(\theta) = \frac{\rho(\theta) - \langle\rho\rangle}{\langle\rho\rangle} \, , \tag{5.6}$$

and use $5\,\%$ of this value to feedforward to the light at the corresponding location. This method has the distinct advantage over the light-based feedforward technique of being *in situ*, and is inherently sensitive to all elements influencing the atoms. Most importantly, it permits the correction for the rolloff of the sheet beam itself, as well as for minor aberrations introduced when expanding and focusing the scanning beam into the plane of the atoms. This has allowed us to create significantly larger optically trapped rings than have been previously demonstrated.

Implementing this atom-based technique gave a significant improvement in the quality of the ring condensates. A side-by-side comparison of an 'out-of-the-box' ring, and its feedforward-optimised counterpart is shown in Figure 5.11. Densities are measured $10.8\,$MHz detuned from the cooling transition.

The algorithm is robust, and applies equally well to larger rings of up to $150\,\mu$m radius.

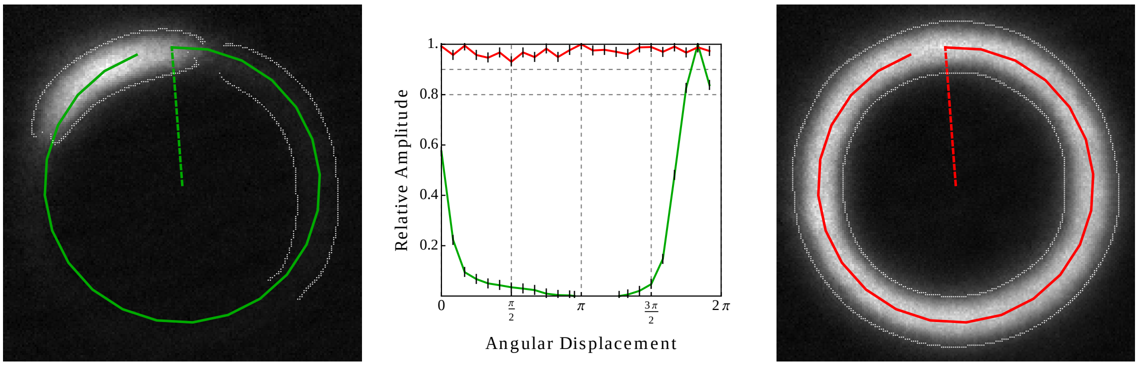

Figure 5.11: Absorption images of BECs trapped in a 70 µm radius trap, taken after 1 ms time-of-flight. White lines are the boundaries of the ring obtained by applying a gaussian filter, and then an edge detection. The green and red lines identify the 24 beam locations used to create the ring. *Left*: Before correction, showing a pooling of atoms at the deepest point in the potential. *Right*: After applying the feedforward technique. *Centre*: Relative atom density as a function of position around the ring. Density fluctuations are reduced to below 10 % using these imaging parameters, though are subject to saturation effects, causing an underestimate of the variation. Image reproduced from [1].

Our method typically reduces density fluctuations to below 10 % after 5 iterations, after which the fluctuations are on the order of the shot-to-shot variation. Temperatures of the ring BECs created in this manner are ~ 60 nK, with condensate fractions of 0.40. The radial trapping frequency is $2\pi \times 55$ Hz. The trap generally captures a total (i.e. thermal, and condensed) of 3.8×10^5 atoms from the 1.0×10^6 in the BEC formed in the hybrid trap. Further discussion of the rings created with this algorithm is available in [1].

5.3 Understanding residual structure

While the condensates formed in this manner appeared smooth to within 10 % in trap, they showed significant structure after a 20 ms period of ballistic expansion. An example of the structure observed in time-of-flight is shown in Figure 5.12. Tightly-spaced radial bands, of typical thickness ~ 18 µm azimuthally, indicate the presence of high-energy excitations. Ultimately, altering the loading has allowed us to mitigate these excitations since.

For 1.5×10^5 condensed atoms in this geometry, we would also expect to be in the phase

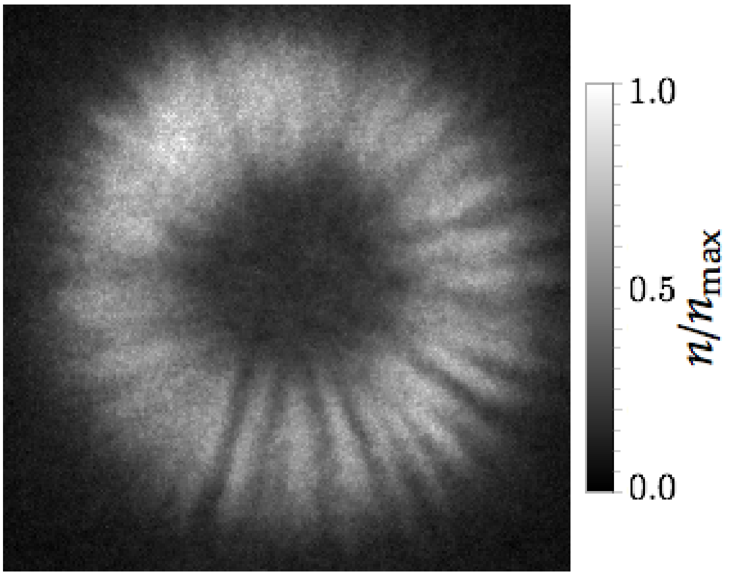

Figure 5.12: Absorption image of the ring BEC after 20 ms time-of-flight expansion. This image is a subsequent realisation of the same trap shown in Figure 5.11. Clear radial bands are evident in the ring, which are suggestive of circulation around the ring. The high spatial frequency relative to the circumference indicates that higher-energy states have significant occupation.

fluctuating regime (see §3.5), with the $1/e$ decay length of the correlation function to be $l_\varphi \approx 63.4\,\mu\mathrm{m} = 0.288\pi R$. As reported in [112], the phase coherence length should exceed the critical value $l_{\varphi,\mathrm{crit}} = \pi R$ in order to be considered globally coherent. The rings presented thus far are therefore not considered coherent.

5.3.1 Loading of ring

In the earlier sections of this chapter, we have considered the case of first forming a BEC in the hybrid trap, then transferring the BEC into the sheet, and finally loading it into the side of a ring, as we saw in Figure 5.6. This has proven ultimately to be an unsuitable means by which to create a ring condensate. It is instead preferable to load atoms thermally, and then evaporate in the ring trap down to BEC. In the first instance, this permits a larger number of atoms to be held in the ring. In addition, releasing a pinned BEC to disperse around the ring induces higher-energy excitations, as the overlap of the wavefunction in the pinned configuration with the ground state of the ring potential is poor. Evaporating within the ring instead minimises the occupation of higher-energy modes.

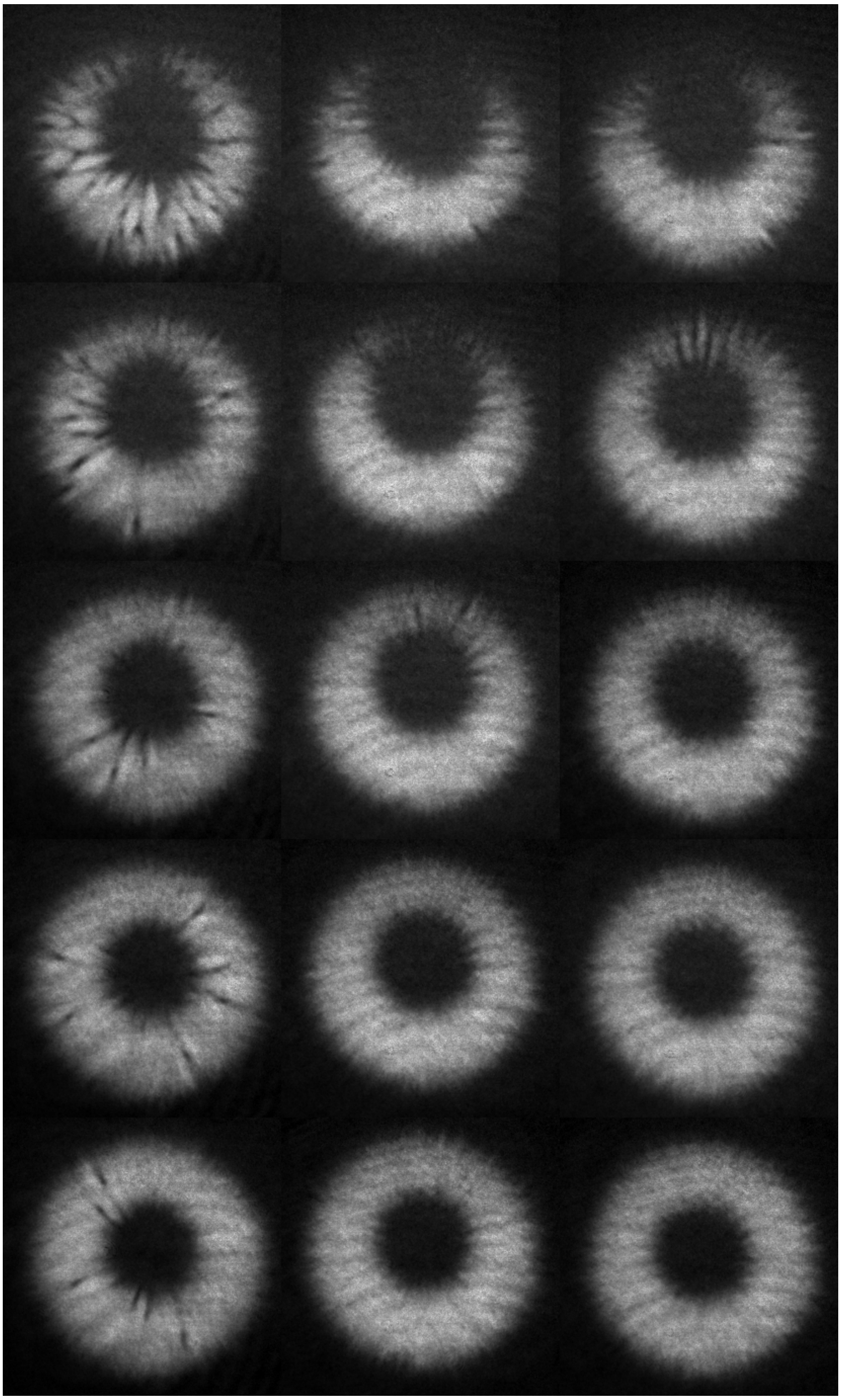

Figure 5.13: Excitations in 20 ms time-of-flight expansion for different loading schemes. The rows of the table are separated by 400 ms, with the first row 200 ms after the start of the evaporation ramp. *Left*: Ring centre overlapping with hybrid trap. *Centre*: Bottom of ring overlapping with hybrid trap, evaporating with sheet only. *Right*: Bottom of ring overlapping with hybrid trap, evaporating with sheet and pin beam powers in common ratio.

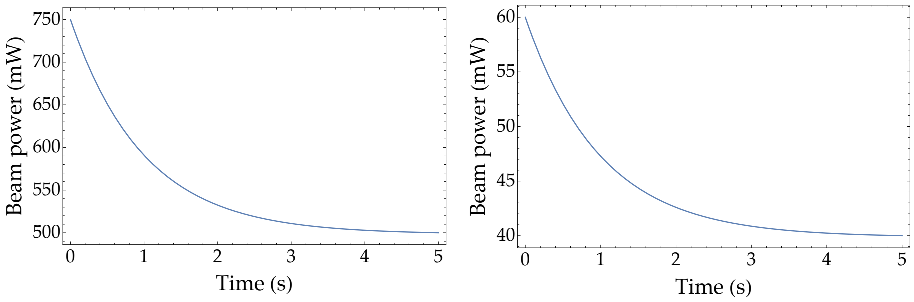

Figure 5.14: Beam powers used in final rings. Actual powers used may vary from those shown, but the beams remain in proportion to one another, reducing by the same factor, and maintaining the same shape. *Left*: Sheet beam power. *Right*: Pin beam power. Ramps used have $1/e$ decay constants of 1 s.

We note the presence of a significant number of vortices in the ring, if loaded with the hybrid trap overlapping with the ring centre. Figure 5.13 shows a comparison of three loading schemes trialled. If, instead, the hybrid is overlapped with the bottom of the ring, the loading creates a significantly smaller number of vortices with the improved overlap. Furthermore, we no longer observe these vortices in the expanded rings after ~ 1.0 s of the optical evaporation. Interestingly, despite the sheet and pin powers being in common ratio for the final trial of Figure 5.13, at earlier times, the ring is still not fully occupied. This arises due to the effect of gravity weakening the sheet's confinement, which becomes more significant as the sheet power is reduced.

In our final rings, which we will analyse in § 5.3.3, we employ exponential ramps on both the sheet and pin beam powers, as shown in Figure 5.14. Specific powers may vary from those shown, but they remain in constant proportion to one another, and reduce to two-thirds of their initial value.

With the improved atom numbers and reduced excitations afforded by this new loading process, we are able to perform the feedforward algorithm using expanded clouds, rather than the in-trap shots. This minimises saturation effects resulting from the higher densities, and allows us to produce very smooth traps for radii up to 150 µm. One such realisation of a 150 µm radius ring is shown in Figure 5.15. The number of atoms trapped

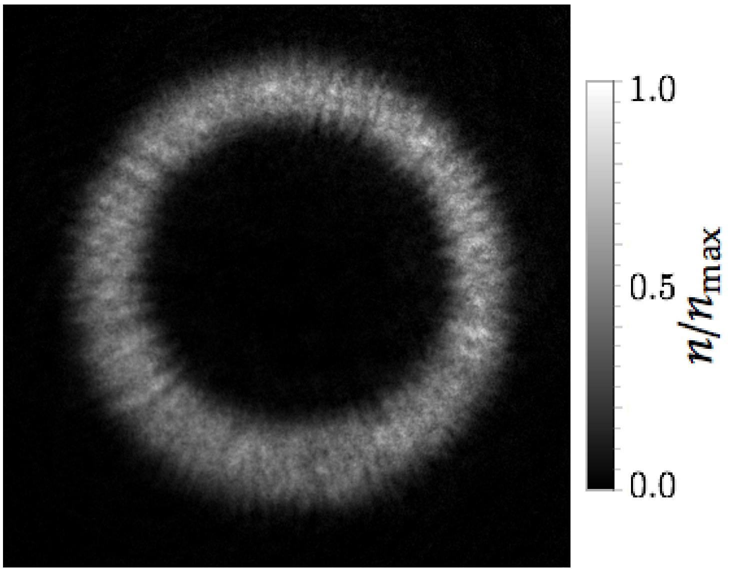

Figure 5.15: $150\,\mu\mathrm{m}$ radius ring after $20\,\mathrm{ms}$ time-of-flight expansion. Variations in the density around the ring are measured at $9\,\%$. The image is normalised to the peak density.

is also considerably larger, up to 3×10^6, and condensate fractions are significantly improved.

5.3.2 Beam tracking

We have noticed in longer time-of-flight images that there was a single, dense band in the ring for most experimental realisations, and subsequently identified that this band tracks the beam location. By varying the hold time in intervals of $t/8$, where t is the scanning period, we are able to track the motion of the bright band at varying scan frequencies. We have performed simulations of a damped Gross-Pitaevskii equation (GPE) for varying scan speeds, and identified a similar behaviour. Comparison of the experimental and simulated data allows us to draw conclusions about the influence of the scanning process itself on the condensate.

Simulation

In the following sections, the Gross-Pitaveskii equation has been integrated numerically with a fourth-order Runge-Kutta method. The simulations in this work were carried out with XMDS [124]. In the data presented here, a $300\,\mu\text{m} \times 300\,\mu\text{m}$ area in the horizontal plane has been sampled on a grid comprising 512×512 points.

A normal computational approach to find the ground state of a potential is to evolve a test wavefunction in imaginary time, $t \to it$, under constant renormalisation. This leads to exponential decay of the wavefunction, with higher-energy states decaying most rapidly, yielding finally the Hamiltonian's ground state. This approach, however, makes little sense in a time-varying potential. In this work, we have found the ground state of the averaged potential in the usual manner, and then insert this ground state into the time-varying potential. Following the approach of [125] and the references within, we employ a phenomenologically-damped GPE,

$$(i-\gamma)\hbar\frac{\partial}{\partial t}\psi = -\left(\frac{\hbar^2}{2m}\nabla^2 + V + g_{2\mathrm{D}}|\psi|^2\right)\psi\,, \tag{5.7}$$

with $\gamma = 0.003$. This value of γ is chosen to match that used in [125], and is known to capture a number of phenomena not encapsulated by the GPE alone. The effective 2D-interaction parameter $g_{2\mathrm{D}} = \frac{\sqrt{8\pi}\hbar^2 a_s}{m_{\mathrm{Rb}} l_y}$ assumes harmonic trapping in the y direction with characteristic length $l_y = 1.505\,\mu\text{m}$. This value is determined by matching the chemical potentials of the 2D and 3D ground states. This type of model has been shown to capture many effects of the interaction between condensed and thermal atoms [126–128]. The averaged potential employed in each case is

$$V_{\text{avg}} = V_{\text{depth}}\left(1 - \exp(-2(\rho-\rho_0)^2/w_\rho^2)\right)\,, \tag{5.8}$$

where $V_{\text{depth}} = k_B \times 181.1\,\text{nK}$ and $\rho_0 = 82.0\,\mu\text{m}$. These parameters yield a $2\pi \times 50\,\text{Hz}$ radial trapping frequency with a $26.5\,\mu\text{m}$ waist beam. The time-varying potential is given by

$$V_{\text{TAOP}} = \zeta N_{\text{pts}} V_{\text{depth}}\left(1 - \exp(-2(\mathbf{r}-\mathbf{r}_0(t))^2/w_\rho^2)\right)\,. \tag{5.9}$$

Here $\mathbf{r}_0(t)$ is given in polar coordinates as $(r_0, 2\pi f t)$, with f the variable scan frequency. $\zeta \approx 0.48155$ is a geometrical factor that encapsulates the overlap between adjacent beam

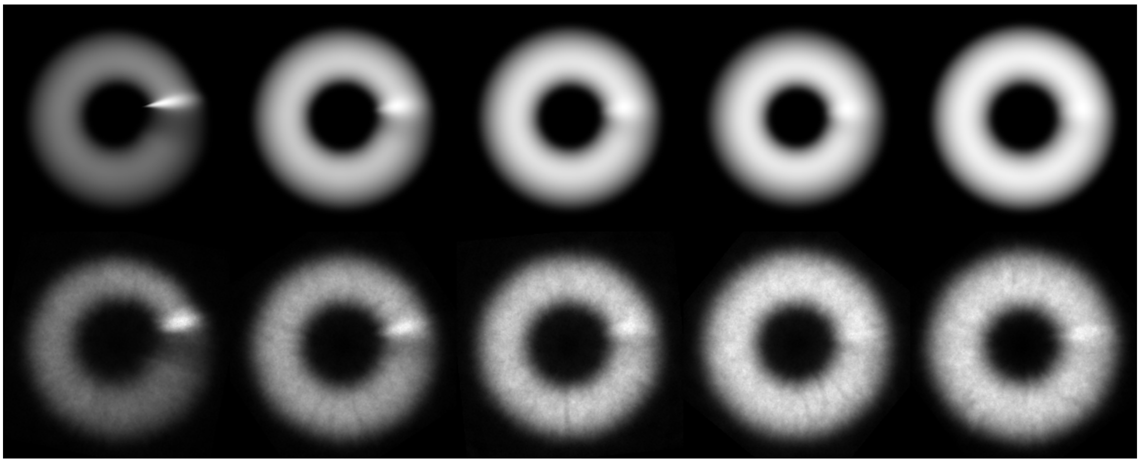

Figure 5.16: Beam tracking behaviour for $82\,\mu\text{m}$ radius rings, shown after $20\,\text{ms}$ time-of-flight. Each individual image is formed by summing 8 images at different beam locations around the ring, which have been individually rotated to compensate for the beam movement. From left to right, the scan frequencies are $625\,\text{Hz}$, $1.750\,\text{kHz}$, $3.250\,\text{kHz}$, $4.750\,\text{kHz}$, and $6.250\,\text{kHz}$. *Above*: Phenomenologically-damped GPE simulations. We employ a 512×512 grid over a $300\,\mu\text{m}$ square region. *Below*: Experimental realisation showing the same beam tracking. Images are independently normalised to their peak densities, and the total number of atoms in each case is 2.0×10^6.

positions, and $N_{\text{pts}} = 32$.

Interestingly, after 250 scan periods, there is negligible variation in the in-trap density. This is consistent with the smoothness of the feedforward images shown in Figure 5.11, and confirms that the absence of the fringes in in-trap experimental data is not simply a result of saturation effects. The time-of-flight expansions, however, show a dramatic beam-following behaviour. A side-by-side comparison of simulated data with the experimental realisation is shown in Figure 5.16.

An important point to make here is that sources including [74] and [73] state scan frequencies well exceeding the trapping frequencies should suffice to be operating in the time-averaged regime. Our realisations have trapping frequencies of $(\omega_\rho, \omega_y) = 2\pi \times (50\,\text{Hz}, 140\,\text{Hz})$, and we still observe beam tracking behaviour above scan frequencies of $3.250\,\text{kHz}$. This behaviour can be characterised both in terms of an azimuthal density gradient, with the bright bands of Figure 5.16 being followed by 'tails' of decreasing density. A sample azimuthal profile demonstrating this behaviour at a scan

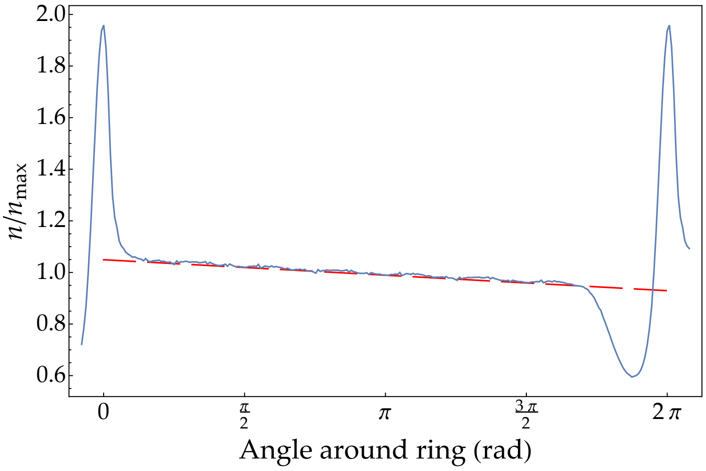

Figure 5.17: Extracted azimuthal profile of ring scanned at $625\,\mathrm{Hz}$ as in Figure 5.16, extracted from simulated data. Shown in blue is the density, normalised by the mean, as a function of angle around the ring. The red, dashed line is a fit to the central region, excluding the bright band and trough at the location of the scanning beam. The gradient of this line decreases with faster scan speed, as shown in Figure 5.18. Note also the angular width of perturbation due to the beam, which is restricted to a wedge of width $\sim 2\pi/N_{\mathrm{pts}}$, where $N_{\mathrm{pts}} = 32$ for this particular geometry. The bright feature at the beam location is shown twice here, with the range extended beyond a single revolution of 2π.

speed of $0.625\,\mathrm{kHz}$ is shown in Figure 5.17. We also observe a decay in the density variations about the mean as we move to higher scanning speeds. Here, by density variations we mean the sum of squares of the data points about the fitted line shown in Figure 5.17, excluding the sharp peak and trough features at the left and right edges of the figure. Both effects are shown in Figure 5.18. Particularly in the context of precision measurement, we must be careful to consider the effects of the scanning process on the condensate's phase *locally*, and how the condensate will respond in time-of-flight expansion.

Local variations in phase

The fact that these bright, beam tracking bands are only present in time-of-flight suggest that they result from local variations of the in-trap *phase*, rather than the condensate *density*. Local phase differences form across the beam profile, with those atoms at the beam's instantaneous location experiencing a different potential to the remaining atoms

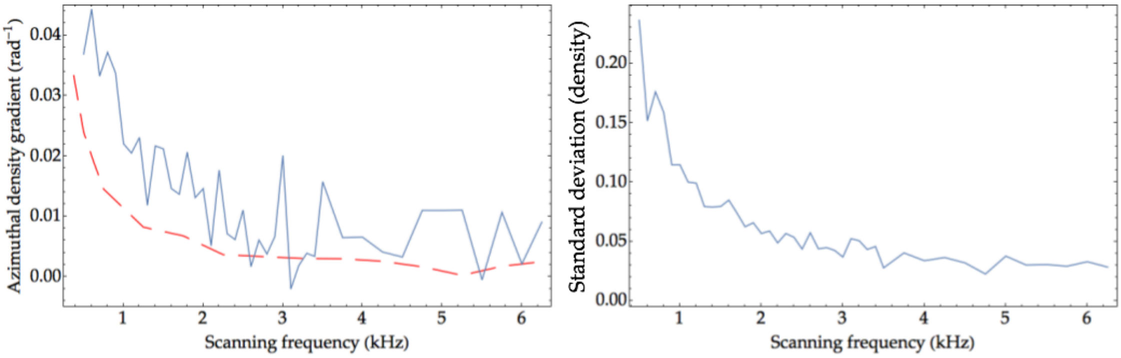

Figure 5.18: Beam tracking behaviour in a scanned optical trap, characterised in terms of the azimuthal density gradient, and the fluctuations in the density about the mean. *Left*: Magnitude of the density gradient in the 'tail' following the bright bands of Figure 5.16. The solid, blue line shows experimental data, while the red, dashed data are extracted from simulations. *Right*: Decay of density variations about the mean value with scan frequency. Variations are normalised by the mean density, after accounting for the gradient from the plot at the left. Pixels in the vicinity of the bright bands shown in Figure 5.16 at the location of the beam are excluded from these plots, with plots instead showing properties of the bulk condensate. Experimental data in both plots provided by T. Bell.

in the ring. The beam's tangential speed exceeds $1\,\mathrm{m\,.\,s^{-1}}$, which well exceeds the condensate's speed of sound. So, while the beam is scanning, the condensate can't move quickly enough to respond before the local variation is removed again when the beam advances. If, however, there exists a residual phase gradient within the condensate when it is released, this will be expressed in the time-of-flight expansion.

Figure 5.19 shows the evolution of the phase in a scanned ring trap, using parameters that closely match our experimental values. These data are taken from the same damped GPE simulations introduced in the previous section. We can see a clear propagation of a phase front starting at the ring's right, and running clockwise in subsequent images. The position of this phase step is consistent with the location of the beam at that time in the simulation.

Contours of the phase around the ring, taken at a radius of $82\,\mu\mathrm{m}$, are shown in Figure 5.20. These correspond to the fourth, fifth and sixth images in Figure 5.19, though the same behaviour is observed for any combination. The key feature in this plot is the

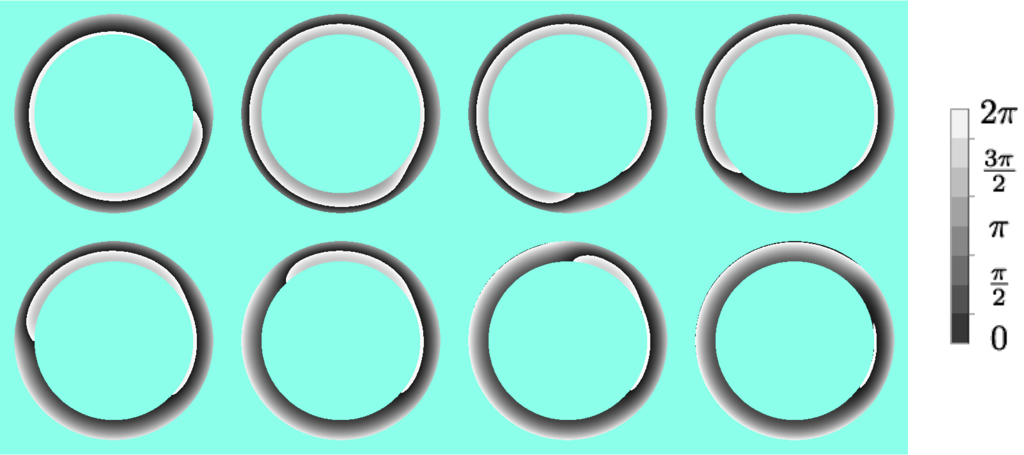

Figure 5.19: 2D-GPE simulations of a condensate held in a ring, scanned at 6.25 kHz. The radial trapping frequency used is 50 Hz, and the radius of the ring is 82 µm. Images are in 20 µs steps, running from left to right. The scanning beam starts on the right of the ring, and scans clockwise. Positions where the atomic density is less than 1 % of the peak value have been excluded for clarity.

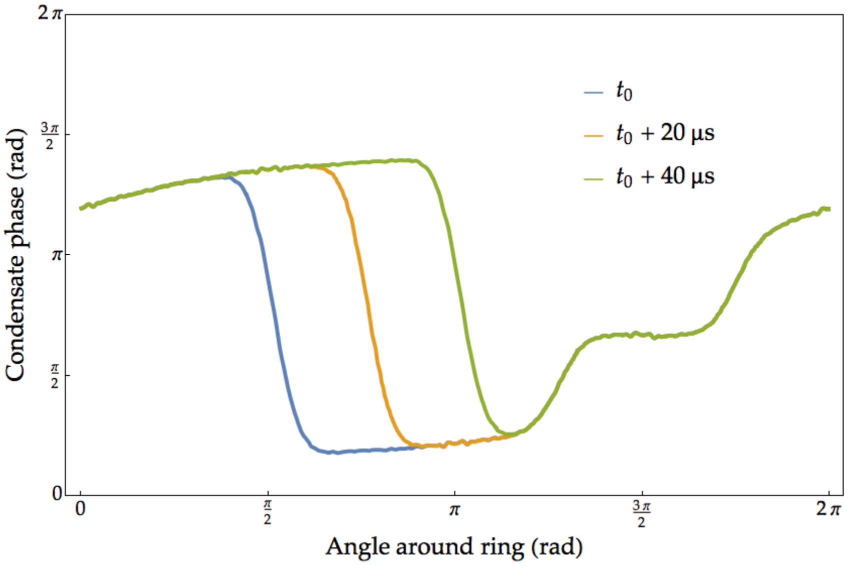

Figure 5.20: Contours of the condensate phase as the scanning beam propagates, extracted from simulations. These curves correspond to an 82 µm radius ring scanned at 6.25 kHz. The drop at $\pi/2$ for the blue curve corresponds to a phase difference of 1.14π at the beam location. The orange and green curves show the phase step propagating around the ring with the beam. The step at $3\pi/2$ marks the first point of the beam's scan, which is ill-defined in the experimental context. This feature is a limitation of the computational method. It does not, however, affect the conclusion regarding the phase drop at the beam's location.

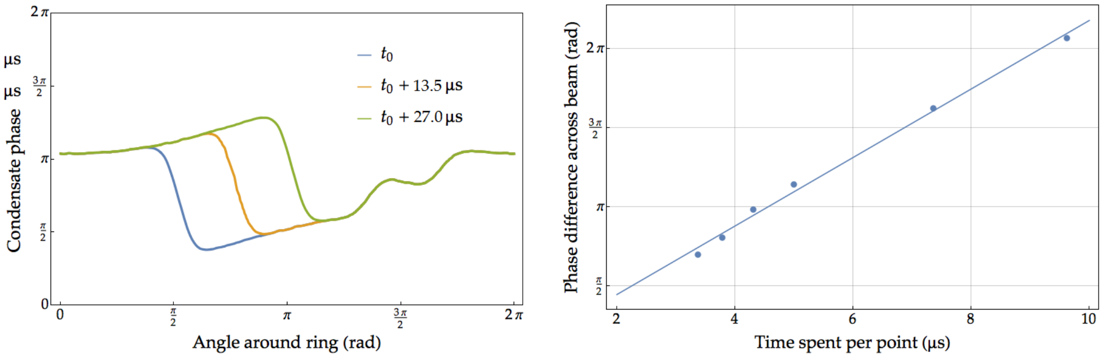

Figure 5.21: *Left*: Phase difference developed across the beam location when scanned at $9.250\,\mathrm{kHz}$, giving a phase difference $\sim 0.70\pi$, c.f. Figure 5.20. *Right*: Phase difference developed across the beam as a function of the time spent at each point around the ring. Simulations were performed for an $82\,\mu\mathrm{m}$ ring with $50\,\mathrm{Hz}$ radial trapping frequency. Our maximum switching speed is currently $5\,\mu\mathrm{s}$, which still results in a significant phase variation of $\sim 1.14\pi$. This is reduced either by using a weaker trap, or by using a faster scan speed. The plotted data are described by the regression fit $\Delta\phi = ((0.68 \pm 0.02)\,\mathrm{rad}\,.\,\mu\mathrm{s}^{-1})t + (0.03 \pm 0.14)\,\mathrm{rad}$, which is consistent with zero phase difference as the scanning speed tends to infinity.

propagation of the phase step as the beam scans around the ring. Phase contours have been taken at a radius of $82\,\mu\mathrm{m}$, and are reminiscent of the SQUID behaviour described, e.g. in [69].

For our experimental parameters, the phase drop across the beam is $\sim 1.14\pi$. This phase difference is considerably reduced for a faster scan speed, with simulations at $9.250\,\mathrm{kHz}$ showing a shift of 0.70π, and yet faster speeds expected to be smaller again. The phase drop is proportional to the time spent at each of the 32 points on the ring circumference, and is plotted in Figure 5.21. It is consistent with the quantity $\zeta N_{\mathrm{pts}} V_{\mathrm{depth}} \tau/\hbar$ to within a numerical prefactor of order unity, where τ is the time the beam spends at each location. Ultimately, in the context of interferometry, we aim to reduce this local phase development. Schemes relying on the interference of the condensate, either with itself, or with a reference BEC, would be affected by such a phase drop. An example using the self-interference of a scanned ring, i.e. the ring being released from trap to expand into itself, such as in [72], is shown in Figure 5.22. The interference rings are discontinuous within the box marked, as a result of the phase difference across the beam developed in trap.

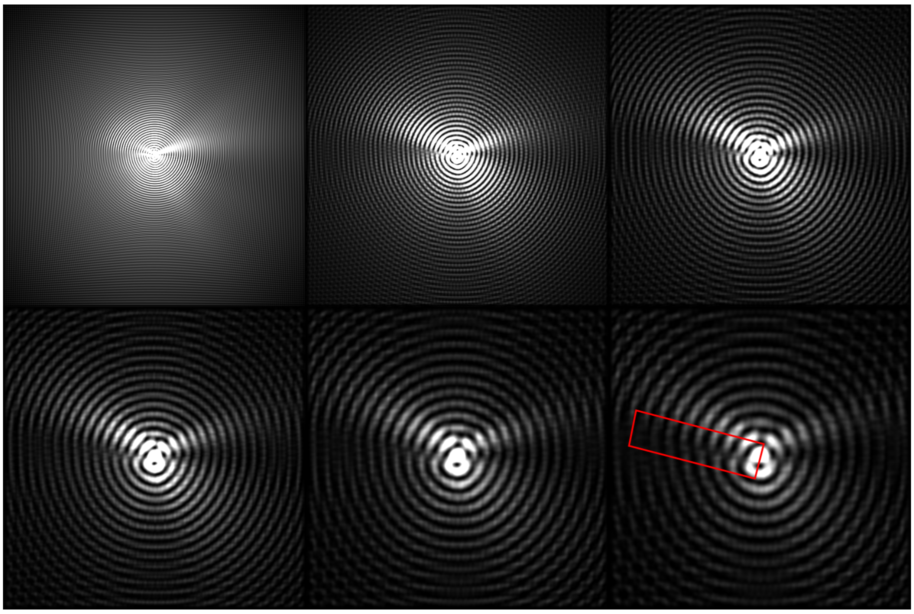

Figure 5.22: 2D-GPE simulations of the self-interference of a scanned ring. From left to right, images are in $80\,\mathrm{ms}$ intervals after release from an $82\,\mu\mathrm{m}$ radius trap scanned at $6.25\,\mathrm{kHz}$. Marked in red is the region in which the phase drop across the beam is visible, as the high-density regions do not match up along this line. Each of the six frames shown is $300\,\mu\mathrm{m}\times300\,\mu\mathrm{m}$.

This beam-tracking behaviour could indeed prove catastrophic for phase sensitivity in the current setup. Using equation (1.2), and taking the Earth's rotation rate of $\sim 10^{-4}\,\mathrm{rad\,.\,s^{-1}}$ as a benchmark, the phase sensitivity required would be of order 10^{-2}. Were the beam-tracking behaviour the limiting factor here, a $100\times$ speedup of the scan would be required. Given the localised nature of the dip, however, and noting the techniques used in [70], the continuous phase variation around the ring introduced by a rotating reference frame should be able to be decoupled. This suggests a more modest tenfold improvement may suffice.

Doppler-like shift

One of the simplest proposals for an atomic Sagnac interferometer is based on the dispersion of atoms into the ring. In this type of interferometer, atoms are pinned at one point on the ring, then subsequently released into the full ring waveguide. They expand into the ring, with the condensate eventually interfering with itself at the opposite side of the ring. The shift in the interference fringes when performed in a rotating reference frame is

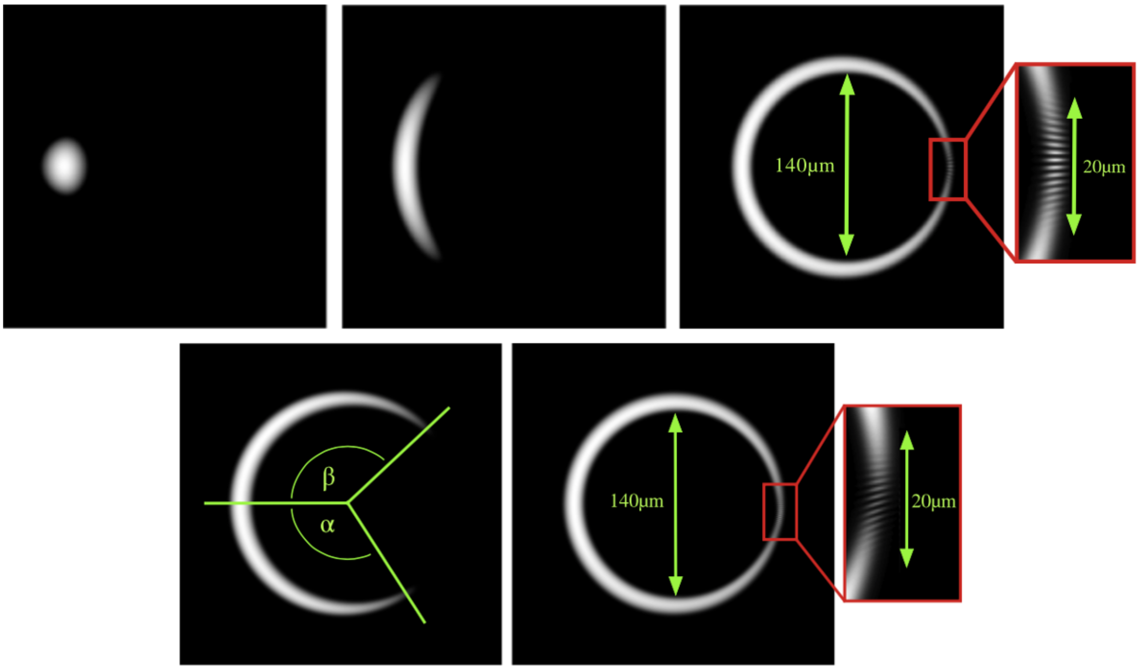

Figure 5.23: Simulation of BEC dispersion into a ring trap. Note the fringe spacing in these simulations is below the imaging resolution we are able to achieve with our system. It does, however, highlight a relevant effect for interferometry purposes. *Above*: Expansion of a BEC into a static trap. *Below*: BEC expanding into a time-averaged optical trap, scanned clockwise at 2 kHz. The arms of the interferometer are no longer symmetric, and the upper arm expands into the ring more quickly than the lower arm, i.e. $\beta > \alpha$. The resultant interference fringes are also rotated, as would be expected when measuring a Sagnac shift. Images adapted from [1].

a measure of the Sagnac phase.

Preliminary simulations show similar behaviour for scanned potentials, seen in Figure 5.23. By virtue of scanning the potential clockwise, the symmetry between the upper and lower arms is broken. Atoms travelling in the upper arm propagate with the scanning beam, while those in the lower arm propagate against the beam. This results in the atoms in the top arm evolving further in terms of phase than those in the lower arm, when propagating over the same distance, akin to a Doppler-like shift. The phase difference is more pronounced at lower scan speeds. The full characteristics of this phase shift, and its effect on measurements of the Sagnac phase remain an avenue for future work. We seek here only to highlight the effect as a guide for future work.

5.3.3 Characteristics of the final rings

Using the loading described in §5.3.1, we load a significantly larger number of atoms into the trap, up to $\sim 3 \times 10^6$. In this section we will cover the temperatures, condensate fractions, and lifetimes achievable with our final experimental parameters.

Ring temperature

The ring temperature is extracted by performing a similar analysis to that used in the feedforward algorithm itself, which we covered in §5.2.4. We extract the optical density in the usual manner. Instead of binning pixels with angle as we did for the feedforward, however, we bin radially, and calculate the mean optical density in each bin. This yields the radial density profile, $|R(\rho)|^2$, to within a normalisation factor. Typical radial profiles are shown in Figure 5.24.

For the condensate, we assume the Thomas-Fermi limit applies. The condensate is in the bottom of a Gaussian-shaped trap, where the potential is well-approximated by a harmonic trap. We therefore have a term

$$|R(\rho)|^2_{\text{cond}} = \max\left[-B(\rho-\rho_0)^2 + k,\ 0\right]^{3/2} \tag{5.10}$$

that contributes to the total density. The index of $\frac{3}{2}$ results from integrating along the y direction to obtain the measured column densities. The non-condensed atoms contribute an additional Gaussian that sits beneath the BEC component, of the form

$$|R(\rho)|^2_{\text{th}} = A\exp(-2(\rho-\rho_0')^2/\sigma_\rho^2) + \text{offset}\,. \tag{5.11}$$

We allow for an offset in the OD to cancel the effects of unequal exposures in images of the beam with, and without, the condensate present. A least squares fit to the sum of (5.10) and (5.11) yields the width of the thermal fraction, σ_ρ.

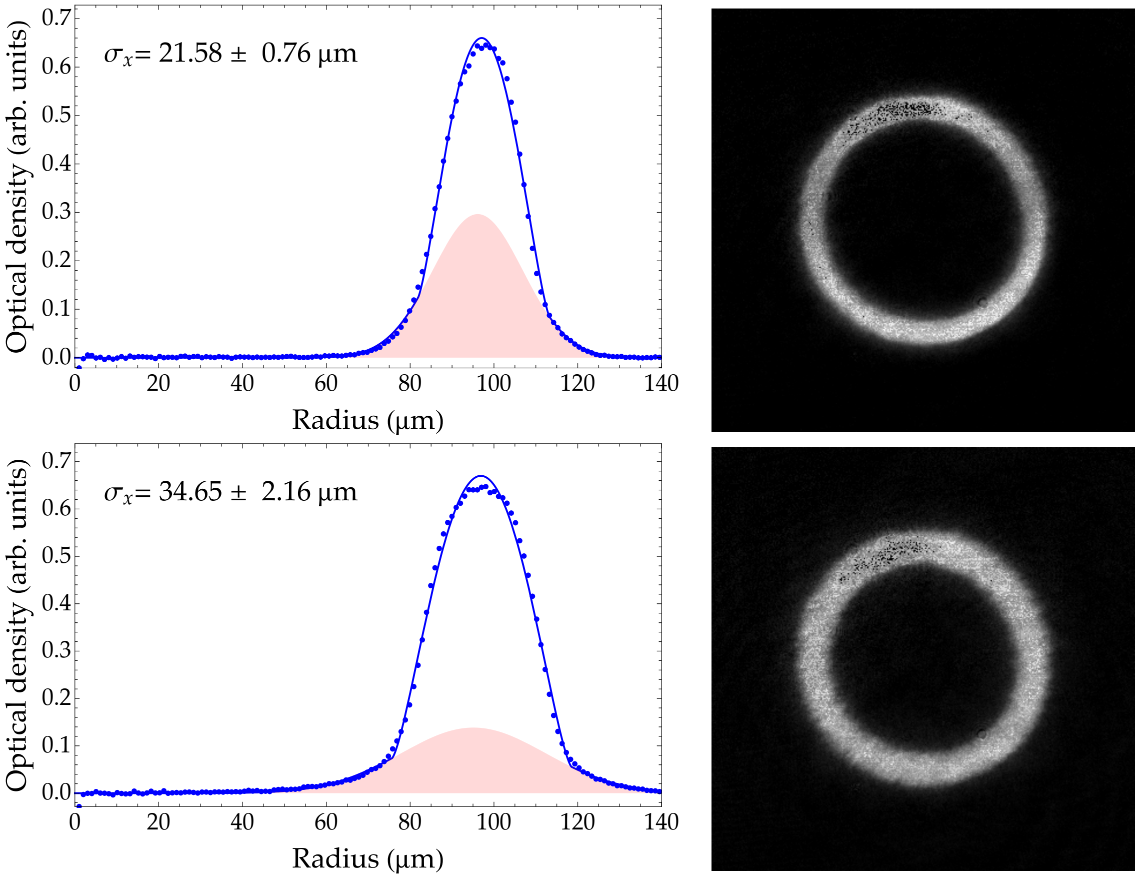

Figure 5.24: Extracted radial profiles for $100\,\mu$m radius ring, with $2\pi \times 55\,$Hz radial trapping frequency. Imaging light is detuned by $5.4\,$MHz from the cooling transition. Profiles are averaged azimuthally. *Above*: Radial profile at $3\,$ms time-of-flight. *Below*: Radial profile at $7\,$ms time-of-flight. The red, shaded areas represent the thermal component, while the remaining area enclosed by the curve is Bose-condensed. Blue points are experimental data, and the solid blue curves are least-squares fits to the theoretical profile. Inset are the $1/e^2$ waists of the two Gaussians comprising the thermal fractions. Both show signs of saturation for higher optical densities (ODs), reducing the height of the condensate peak, and thereby underestimating the condensate fraction. These data give the temperature of the atoms in the trap as $(44 \pm 9)\,$nK.

The thermal fraction expands according to its in-trap momentum distribution as

$$\sigma_\rho^2(t) = \frac{4k_BT}{m\omega_\rho^2}\left(1 + \omega_\rho^2 t_{\mathrm{TOF}}^2\right) , \tag{5.12}$$

and the temperature can therefore be extracted using

$$T = \frac{m}{4k_B}\left(\frac{\sigma_\rho^2(t_2) - \sigma_\rho^2(t_1)}{t_2^2 - t_1^2}\right) . \tag{5.13}$$

This yields a cloud temperature of $T = (44 \pm 9)\,\mathrm{nK}$. This is consistent with the trap depth of $219\,\mathrm{nK}$, estimated using the beam waist and power.

Condensate fraction

There are competing factors influencing the choice of detuning of the imaging light when measuring the ring properties. Using imaging light that is near-resonant with the cooling transition allows for accurate determination of the widths of the thermal component, but the optical depth readily saturates the 256 well-depth resolution of the 8-bit CCD. Additionally, on resonance the light intensity used is close to the saturation intensity, which can inhibit accurate determination of atom number. This means that small detunings tend to underestimate the condensate fraction, and so we use a further detuned beam for this purpose. An image of a $100\,\mu\mathrm{m}$ ring, imaged at $10.8\,\mathrm{MHz}$ detuning after $7\,\mathrm{ms}$ time-of-flight, is shown in Figure 5.25. The typical condensate fractions obtained using our final loading and feedforward techniques are 75–$80\,\%$. The position of the imaging lens has been cross-calibrated against the detuning of the imaging light to ensure the BEC remains in focus for each detuning used.

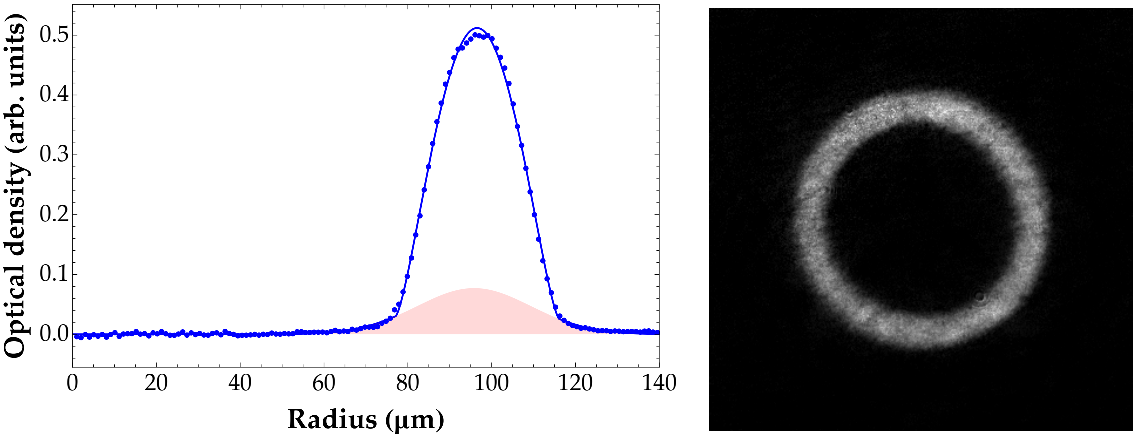

Figure 5.25: Extracted radial profile for $100\,\mu\mathrm{m}$ radius ring, with $2\pi \times 55\,\mathrm{Hz}$ radial trapping frequency. Imaging light is detuned by $10.8\,\mathrm{MHz}$ from the cooling transition. The red, shaded area corresponds to the thermal fraction, while the remaining area enclosed in Bose-condensed. Blue points are experimental data and the solid blue curves are least-squares fits to the theoretical profile. Averaged over this image, and three additional realisations, the condensate fraction is found to be (0.77 ± 0.03) .

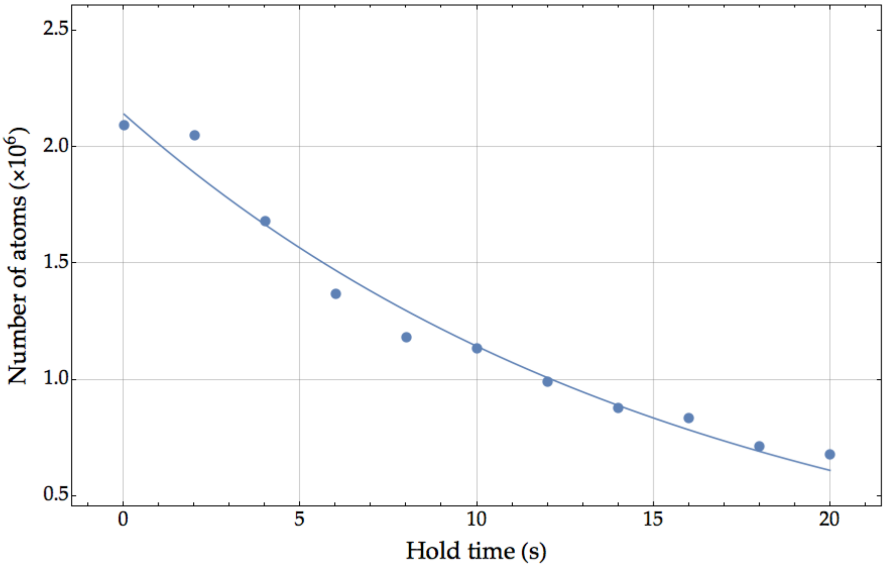

Figure 5.26: Decay of atom number in $100\,\mu$m ring as a function of hold time, for a sheet power of $563\,$mW. The fitted line is an exponential with $1/e$ lifetime $(15.9 \pm 0.9)\,$s.

Lifetime

The lifetime of the ring condensate has also been determined. After evaporation to BEC, the BEC is held in trap for a variable time. It is subsequently released, and imaged from below. The number of atoms is determined using the expression in §2.5, and plotted against the hold time. The results are shown in Figure 5.26, and yield a $1/e$ lifetime of $(15.9 \pm 0.9)\,$s with a sheet beam power of $563\,$mW, and radial trapping frequency $55\,$Hz. This is consistent with the lifetime of the normal hybrid trap condensates, indicating no significant additional heating in the scanned trap potential.

Phase coherence

The condensate's wavefunction can be represented with a hydrodynamic model of the form $\Psi_{N_c}(\mathbf{r}) = \sqrt{n(\mathbf{r})}\exp(i\varphi(\mathbf{r}))$, explicitly identifying the dependence on the density $n(\mathbf{r})$ and the condensate phase $\varphi(\mathbf{r})$. In three-dimensional geometries, i.e. those with spatial extents of comparable magnitude along each of the Cartesian axes, the transition from cold, thermal gas to condensate is straightforward, in the sense that both density and phase fluctuations are suppressed below the temperature T_c for onset of condensation. In lower-dimensional or extended geometries, such as elongated cigars or rings, however, fluctuations in the condensate phase can remain present [118, 119, 129] despite suppression of density fluctuations below T_c. These are linked with the occupation of low-energy Bogoliubov modes, as discussed in §3.4. A second temperature T_φ is then needed to characterise the transition into the regime with suppressed phase fluctuations.

In the ring geometry specifically, the choice of radial and out-of-plane trapping frequencies, ω_ρ and ω_y respectively, governs the relative magnitudes of T_c and T_φ. Using the relevant expressions from §3.2 and §3.5, we find the ratio

$$\frac{T_\varphi}{T_c} = \left(\frac{4\sqrt{2}\Gamma(\frac{5}{2})\zeta(\frac{5}{2})}{3\pi^5}\right)^{2/5} N_c^{3/5} \left(\frac{\hbar}{mR^2\sqrt{\omega_y\omega_\rho}}\right)^{4/5} . \tag{5.14}$$

In particular we note that weaker traps, with smaller ω_y and ω_ρ, tend to result in T_φ being greater than T_c. This means that the phase fluctuating regime is absent in these weaker traps, making weaker traps favourable for interferometric applications. For tighter traps, with larger ω_y and ω_ρ, however, T_c may instead be larger than T_φ, and the ring condensates may exist in the phase fluctuating regime. Under such circumstances, either high atom numbers or colder temperatures are required in order to suppress phase fluctuations.

In [112], Mathey et al. discuss possible experimental signatures of the phase fluctuating regime, citing specifically the self-interference of ring condensates. While we have not yet performed an analysis of this kind, it is educational for the purposes of the conclusions made in this section to examine the suggested protocol here. When released from their traps, ring condensates expand. After long times-of-flight, they collapse in on themselves, as in Figure 5.27. A coherent ring self-interferes [130], and results in a large peak in the density at the centre of the ring. Mathey et al. show analytically that this peak density is directly proportional to the function $F(l_\varphi)$,

$$F(l_\varphi) = \pi\sqrt{\frac{2l_\varphi}{R}} \exp\left(-\frac{\pi R}{2l_\varphi}\right) \mathrm{erf_i}\left(\sqrt{\frac{\pi R}{2l_\varphi}}\right) , \tag{5.15}$$

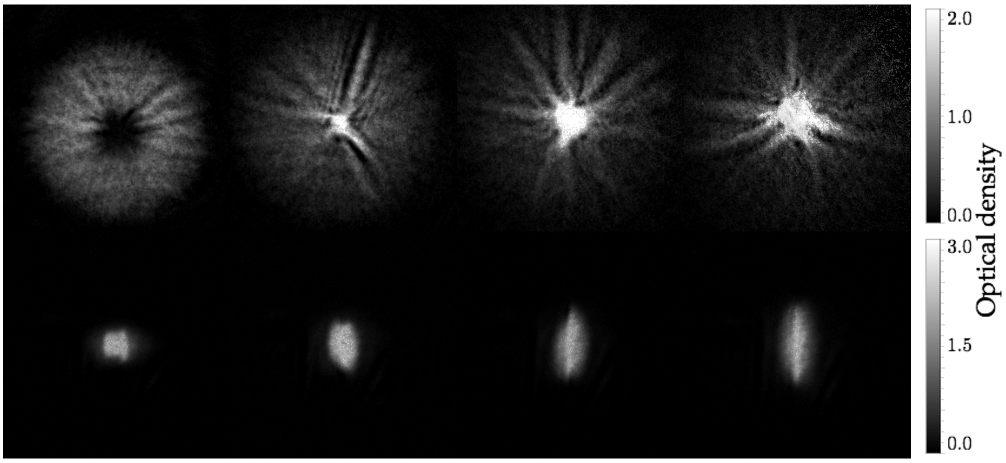

Figure 5.27: Self-interference of a ring condensate expanding in time-of-flight. These data were taken for a 70 µm radius ring, with a radial trapping frequency of 55 Hz. From left to right, images are taken 30 ms, 51 ms, 72 ms, and 93 ms after release from the trap. *Above*: Expansion as seen from underneath the cloud, detuned by 10.8 MHz from the cooling line. Each frame is 260 µm × 260 µm. *Below*: Expansion as seen horizontally, levitating the atoms with the system described in §4.5. Frames are 1660 µm × 1660 µm, and the imaging light is not detuned from resonance. These images show the rapid expansion vertically resulting from the tighter trapping of the sheet. These side images may allow for better detection of the peak density, which causes our detection to saturate when viewed from below, as the cloud is optically thinner when viewed along the horizontal axis.

with l_φ the coherence length, as defined in §3.5 and R the ring radius. The imaginary error function $\mathrm{erf}(iz)/i$ is denoted with $\mathrm{erf_i}(z)$. Specifically, the peak density at the ring centre is expected to vary as

$$n(0,t) \approx \frac{\pi n_{\mathrm{max}}}{2} F(l_\varphi) \left(\frac{m l_\rho R}{\hbar t}\right)^2 \frac{4 l_y}{15} \,, \tag{5.16}$$

in the long-time limit, with n_{max} the peak density in trap, t the time elapsed since release from the trap, and l_ρ and l_y the Thomas-Fermi radii in the radial and vertical directions respectively. These parameters can all be determined from the beam parameters, and directly measurable condensate parameters. This renders $F(l_\varphi)$ experimentally measurable. F is plotted using our trapping frequencies and temperature in Figure 5.28, for a selection of radii accessible with our apparatus, as a function of the number of condensed atoms held in the ring. For further detail on this function and its relation to measures of coherence, the reader is directed to [112].

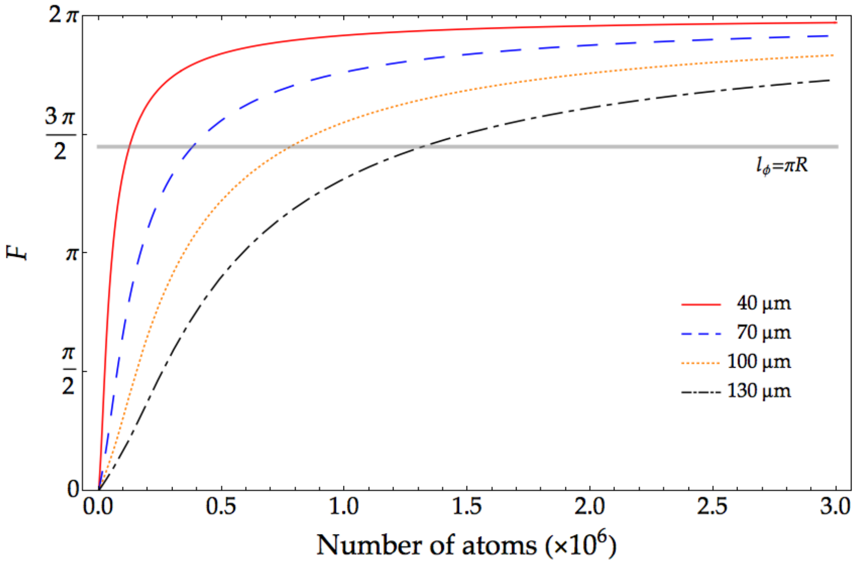

Figure 5.28: The phase coherence of a ring condensate can be described in terms of the F function plotted here, after L. Mathey et al. [112], which describes the peak density in a self-interfering ring condensate. A condensate is considered fully coherent once F exceeds the threshold at $l_\varphi = \pi R$, marked here in grey. F has been evaluated at $T = 44\,\text{nK}$, for trapping frequencies of $(\omega_\rho, \omega_y) = 2\pi \times (55, 140)\,\text{Hz}$.

We obtain condensate numbers $> 1.0 \times 10^6$ in traps of radii below $100\,\mu\text{m}$, and well over 2.0×10^6 atoms in larger traps. For a perfectly time-averaged trap, we would therefore expect to be well within the phase-coherent regime, supported by the central self-interference spikes observed in Figure 5.27, which are equally prevalent at larger detunings of up to $40\,\text{MHz}$. This marks the most significant advance in our experiment since publication of [1]. Future work will probe this coherence more thoroughly by varying R, N and T, following the approaches in [112, 130]. Given the weaker traps now employed, these experiments will require large R and decreased atom numbers. The comprehensive study, however, is beyond the scope of this work, with restricted ability to levitate atoms during expansion preventing the observation of self-interference in very large rings to date. At the time of writing, we were limited to $\sim 80\,\text{ms}$ hold times in the levitating field described in §4.5, due to an uncorrected gradient arising from the ion pump. This has since been corrected, and we expect to be able to access the longer times-of-flight required for self-interference of larger, weakly trapped rings.

We note that measures of the rings' coherence are expected to be affected by the perturbations created by scanning the potential. As shown in Figure 5.17, however, this effect should be largely localised to an angular wedge of size $2\pi/N_{\mathrm{pts}}$ for appropriately fast scanning speeds. Moreover, the beam scanning effect is deterministic, and so is expected to result in repeatable structure in the time-of-flight expansions. For a ring in the phase fluctuating regime, however, we would expect to see shot-to-shot variations between subsequent realisations of the same expansion. We should also expect to see the density variations in time-of-flight extending to larger sectors of the ring than for the beam scanning.

5.4 Driving acoustic modes

Our system is not only capable of producing ring condensates, but also manipulating them dynamically. By modulating the intensity of a single beam location on the ring's circumference by $10\,\%$, we are able to generate acoustic modes. We have used an $82\,\mu\mathrm{m}$ radius ring for the data presented in this section. The beam's intensity was adjusted once every ten cycles of the ring, with a total of twenty-eight intensity values used to map out the driving sine wave. This results in acoustic waves driven at $\frac{1}{280}$ of the ring's scan frequency. The buffer length of the SpinCore cards prevents us from using more points than this.

After loading the ring trap, the modulation is performed for $3\,\mathrm{s}$. The condensate is then imaged in intervals of an eighth of the modulation period, after $20\,\mathrm{ms}$ time-of-flight. An example time sequence is provided in Figure 5.29. The presence of bright bands oriented along the radial direction allows us to track the propagation of the sound wave around the ring, and the distance between the bands gives the wavelength of the mode. These bands are particularly bright when counterpropagating modes interfere constructively, as in the third and seventh frames of the figure.

By varying the scanning frequency, we are able to control the driving frequency for the

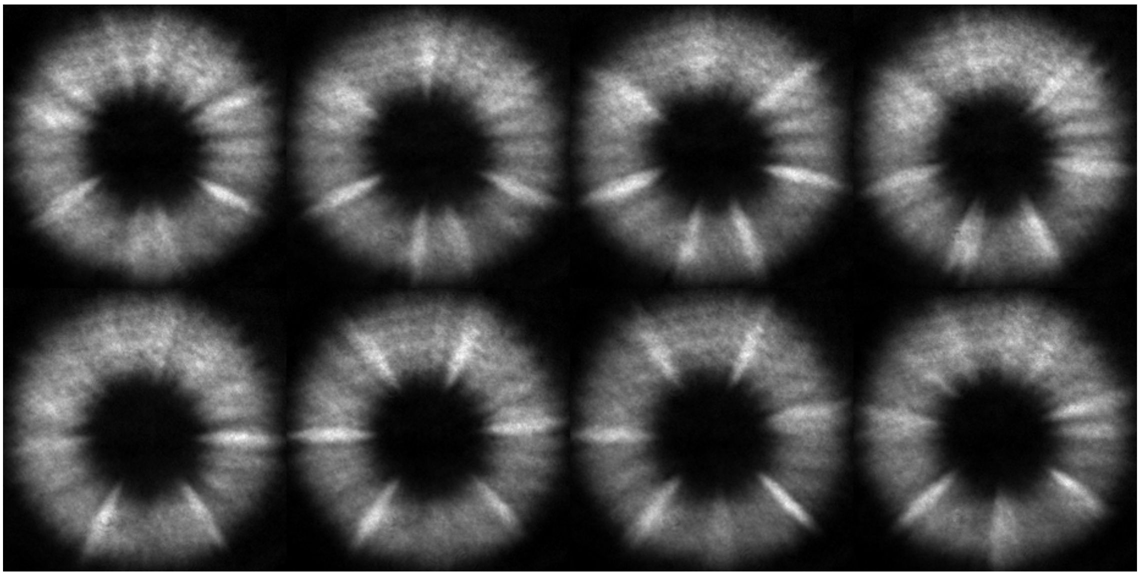

Figure 5.29: The ring shown is modulated at the bottom, and scanned at 5.0 kHz, yielding a modulation frequency of 17.86 Hz. The ring's radius is 82 µm. This frequency is slightly less than that of the $n = 7$ resonant mode of the ring, as evidenced by the presence of seven density peaks around the ring. Images run from left to right, and advance by 7 ms frame to frame, corresponding to an eighth of the modulation period. Images shown are the averages of three subsequent realisations. Densities are normalised to the peak density in each image.

acoustic waves. Unravelling the ring onto a line, we can then identify the positions of the bright bands, and determine the corresponding wavelengths. A sample unravelling is shown in Figure 5.30. This allows us to determine the speed of sound in the condensate, by finding the gradient of a graph of wavenumber against driving frequency. The value obtained here, $(1.34 \pm 0.12)\,\mathrm{mm\,.\,s^{-1}}$, gives a chemical potential of $\mu = k_B \times (18.8 \pm 3.3)\,\mathrm{nK}$ using the expression $c = \sqrt{\mu/m}$ from chapter 3. By enforcing the normalisation of (3.22) in the ring potential, we find a theoretical expression for the chemical potential of

$$\mu = \hbar\sqrt{\frac{2N_c\omega_\rho\omega_z a_s}{\pi R}}\,, \tag{5.17}$$

as given in [1]. Evaluated using the trap parameters $(\omega_\rho, \omega_y) = 2\pi \times (35\,\mathrm{Hz}, 110\,\mathrm{Hz})$ and with $N_c = 1.0 \times 10^6$ atoms condensed atoms, we find a theoretical estimate of $k_B \times 19.9\,\mathrm{nK}$, consistent with the experimental outcome.

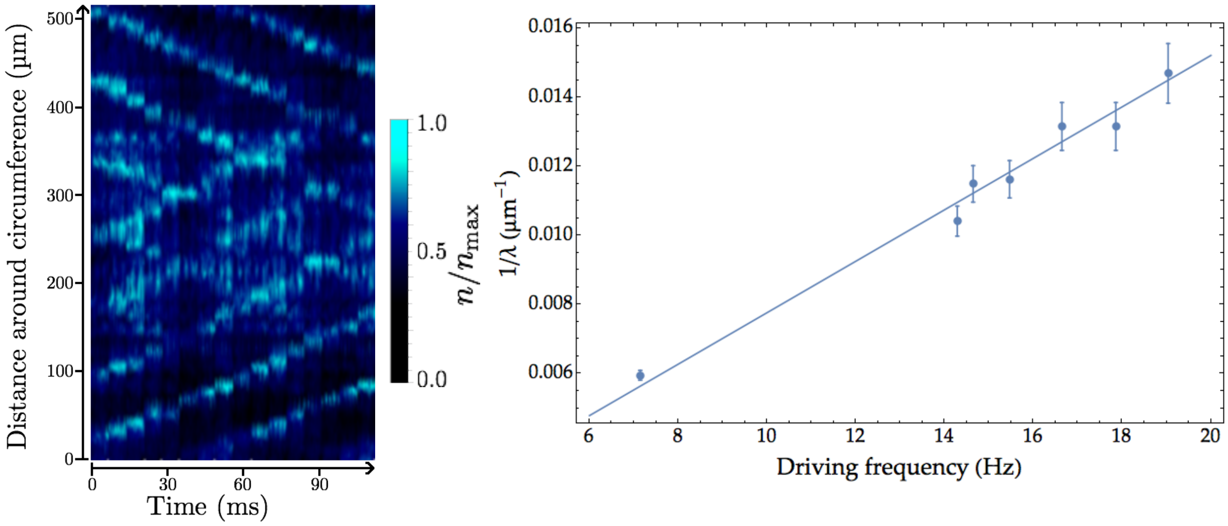

Figure 5.30: *Left*: Representation of acoustic modes propagating around the ring, shown here with images of the ring 'unravelled' into straight, vertical lines. This image corresponds to the eight images in Figure 5.29, as well as the eight subsequent timesteps. Vertically the frame height is the ring circumference, $2\pi \times 82.0\,\mu\mathrm{m}$. Horizontally, the image includes snapshots at $7\,\mathrm{ms}$ intervals over a total of $112\,\mathrm{ms}$, or twice the driving period. *Right*: Variation of the wavenumber of acoustic modes in a ring condensate with driving frequency. Uncertainties arise from the variations in the distance between bright bands for different timesteps. The graph has a gradient of $(745 \pm 66) \times 10^{-6}\,\mu\mathrm{m}^{-1}.\mathrm{s}^{-1}$, which corresponds to a speed of sound of $(1.34 \pm 0.12)\,\mathrm{mm}.\mathrm{s}^{-1}$ in the condensate.

Chapter 6

Outlook and summary

In this thesis, we have demonstrated the first production of Bose-Einstein condensates of rubidium-87 in UQ's hybrid magnetic and optical trap, modelled after [101]. This thesis highlights the main features of the apparatus, with a focus on the final magnetic and optical traps we are able to realise. It is hoped that the versatility of the methods is apparent, as well as the performance aspects.

During my candidacy, the various stages of cooling were optimised, and the typical numbers and temperatures at each stage ascertained. This culminated in the formation of our first condensate at the end of 2014. Further optimisation and adjustment has since taken place, and at the time of submission, we are able to routinely form nearly-pure condensates of 1.5–2.0×10^6 atoms in the hybrid trap. We have shown the hallmark features of asymmetric expansion and bimodality using the hybrid trap.

The optics and control systems for the production of large, all-optical ring traps were designed and implemented. The feedforward technique described in this thesis offers the ability to adjust the trap depth spatially, which permits the creation of larger optical rings than have been previously reported with other techniques [64, 67, 73]. The rings produced in this work are large both in extent, and in the number of condensed atoms. The methods presented here produce smooth rings of radii up to $150\,\mu\text{m}$, with density variations azimuthally of less than $10\,\%$. The optimisation of the technique has led finally to the production of coherent rings up to $100\,\mu\mathrm{m}$ in radius, at temperatures of $(44 \pm 9)\,\mathrm{nK}$, with condensate fractions over $75\,\%$, and with atom numbers $\sim 3.0 \times 10^6$. We have also presented an analysis of the impacts of time-averaged optical potentials on the condensate phase, and shown preliminary data probing acoustic modes, demonstrating the precise control available to us.

There are a broad range of avenues now accessible with our experiment. We shall present here briefly the immediate, and longer-term goals of the experiment.

Firstly, the speed with which we are able to scan patterns using the time-averaged technique is limited by the 2D-AOD's access time. Using our beam parameters, the minimum switching time is $3.2\,\mu\mathrm{s}$, and we have used switching times of $5.0\,\mu\mathrm{s}$ throughout this work to mitigate any beam clipping effects. The laboratory has purchased a new 2D-AOD, which will soon replace the current device. The new 2D-AOD uses the longitudinal mode for sound wave propagation, rather than the shear mode used by our current device. This offers a significant speed up over our current arrangement, and we expect to achieve a eightfold increase in the scanning speed. This will reduce the effects of the local phase drop at the beam's instantaneous location, discussed in §5.3.2. We will also be able to access deeper traps, with correspondingly higher trapping frequencies, as well as being able to scan larger structures.

We plan to directly study the coherence following [112], using the protocol described in section §5.3.3. The studies of ring coherence will be supplemented through use of our Bragg apparatus. With additional PI-feedback locking of the Bragg intensities now in place, and GPIB-based control over the frequency offset, we are well-placed to perform studies of the rings' momentum distribution in both the phase-coherent and phase-fluctuating regimes, as has been demonstrated for linear traps in [119, 129, 131]. These employ the direct self interference of opposite sides of the ring in a Mach-Zehnder style interferometer, as in Figure 1.2. An early example of the Bragg/Mach-Zehnder interference observed in our experiment is shown in Figure 6.1.

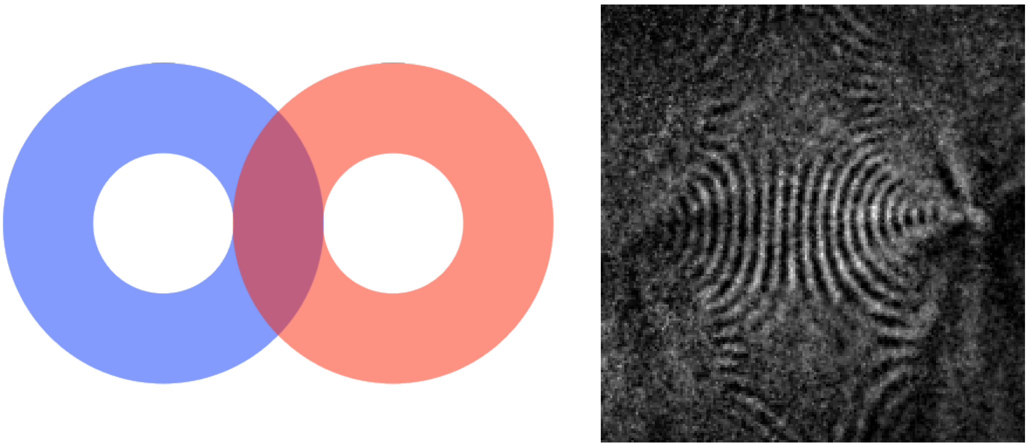

Figure 6.1: Bragg interference fringes observed when overlapping opposite sides of ring condensates. *Left*: Schematic representation of the overlap of two rings, formed by Bragg-splitting and recombining the condensate in time-of-flight. *Right*: Observed interference fringes in the overlap region, which may be used to probe the coherence of the ring.

The time-averaged optical potentials we have presented in this thesis are not restricted to ring geometries, but can in principle be extended to nearly-arbitrary two-dimensional potentials. This versatility of the experiment was a key factor influencing its design and development. Studies of cold-atom thermodynamics are possible by using connected reservoirs [44], as well as the observation of Josephson oscillations [71]. Large, flat potentials permit fundamental studies of the interactions between atoms [132], with the majority of condensate experiments historically having occurred in harmonic traps. We expect each of these geometries to be realisable using our techniques, and are particularly interested in the generation of flat-bottomed, homogeneous reservoirs in future.

One particularly attractive experiment using a large, flat reservoir is the production of Bénard-von Kármán vortex streets [42] in BEC, and the crossover this has with our understanding of superfluidity [43]. Trails of vortices are known to occur in classical, viscous fluids, however their theoretical description relies on the fluid having viscosity, which superfluids by definition do not possess. Vortex dipoles, however, which *are* known to occur in superfluids, have been shown to exhibit similar behaviour. Using the parameter regimes identified in [42, 43], preliminary simulations have been performed using

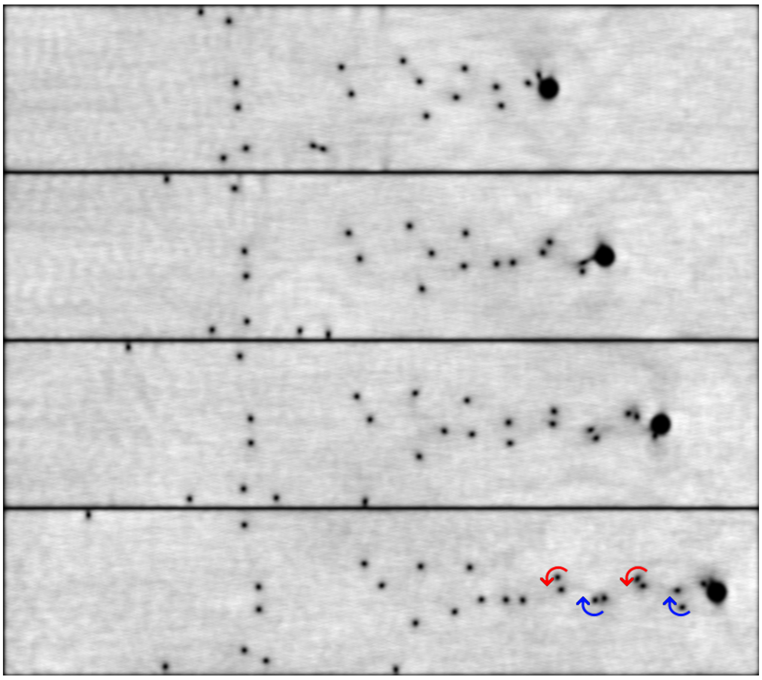

Figure 6.2: Formation of a vortex street in a Bose-Einstein condensate of ^{87}Rb. Simulations are carried out using a phenomenologically damped GPE, as in the previous chapter, and ref. [125]. A $2.03\,\mu\mathrm{m}$ waist blue-detuned beam, shown here as the large, dark circle, is dragged at $0.280\,\mathrm{mm\,.\,s^{-1}}$ through a condensate of 3.2×10^5 atoms. The ensuing trail of vortices begins to form dipole pairs, most clearly identifiable in the final frame. These rotate, but remain aligned along the centre of the reservoir. The full frame in each timestep is $400\,\mu\mathrm{m} \times 100\,\mu\mathrm{m}$. Timesteps are spaced by $95\,\mathrm{ms}$, and a small amount of noise was added to the initial ground state to break the reflection symmetry about the horizontal axis.

length scales and atom numbers accessible with our system. In a large, rectangular reservoir, a blue-detuned beam is dragged through a condensate over a distance of $320\,\mu\mathrm{m}$ at $0.280\,\mathrm{mm\,.\,s^{-1}}$. The results of this simulation are shown in Figure 6.2. The formation of a vortex street is observed at the end of the simulation. While the beam waist used is indeed small, [43] suggests a shallower, but broader beam should also result in the formation of a street, and we believe this should be accessible in our system.

The combination of high-resolution imaging, large trapping volumes, and spatial control over the trap depths in our experiment opens the door for exciting contributions to our understanding of superfluidity, matter-wave coherence, and Bose-Einstein condensation as a phenomenon in its own right. In its current state, and with the incorporation of the features identified here, the apparatus presented in this thesis, in conjunction with the technique of time-averaged optical potentials, promises to serve as an excellent platform for cold-atom experiments in the years to come.

References

[1] T. A. Bell, J. A. P. Glidden, L. Humbert, M. W. J. Bromley, S. A. Haine, M. J. Davis, et al. Bose-Einstein condensation in large time-averaged optical ring potentials. *New Journal of Physics*, 18(3):035003, 2016.

[2] A. A. Michelson and E. W. Morley. On the relative motion of the Earth and the luminiferous ether. *American Journal of Science*, 34(203):333–345, 1887.

[3] A. Abramovici, W. E. Althouse, R. W. P. Drever, Y. Gürsel, S. Kawamura, F. J. Raab, et al. LIGO: The Laser Interferometer Gravitational-Wave Observatory. *Science*, 256(5055):325–333, 1992.

[4] B. P. Abbott, R. Abbott, T. D. Abbott, M. R. Abernathy, F. Acernese, K. Ackley, et al. Observation of gravitational waves from a binary black hole merger. *Physical Review Letters*, 116:061102, 2016.

[5] G. Sagnac. L'éther lumineux démontré par l'effet du vent relatif d'éther dans un interféromètre en rotation uniforme. *Comptes rendus*, 157:708–710, 1913.

[6] L. de Broglie. Recherches sur la théorie des quanta. *Thesis, Annales de Physique*, 3:22, 1925.

[7] A. D. Cronin, J. Schmiedmayer, and D. E. Pritchard. Optics and interferometry with atoms and molecules. *Reviews of Modern Physics*, 81:1051–1129, 2009.

[8] C. Davisson and L. H. Germer. The scattering of electrons by a single crystal of nickel. *Nature*, 119:558, 1927.

[9] O. Carnal and J. Mlynek. Young's double-slit experiment with atoms: A simple atom interferometer. *Physical Review Letters*, 66:2689–2692, 1991.

[10] Y. Torii, Y. Suzuki, M. Kozuma, T. Sugiura, T. Kuga, L. Deng, et al. Mach-Zehnder Bragg interferometer for a Bose-Einstein condensate. *Physical Review A*, 61:041602, 2000.

[11] S. Gupta, K. Dieckmann, Z. Hadzibabic, and D. E. Pritchard. Contrast interferometry using Bose-Einstein condensates to measure h/m and α. *Physical Review Letters*, 89:140401, 2002.

[12] M. Cadoret, E. de Mirandes, P. Cladé, S. Guellati-Khélifa, C. Schwob, F. Nez, et al. Combination of Bloch oscillations with a Ramsey-Bordé interferometer: New determination of the fine structure constant. *Physical Review Letters*, 101:230801, 2008.

[13] J. B. Fixler, G. T. Foster, J. M. McGuirk, and M. A. Kasevich. Atom interferometer measurement of the Newtonian constant of gravity. *Science*, 315(5808):74–77, 2007.

[14] A. Peters, K. Y. Chung, and S. Chu. High-precision gravity measurements using atom interferometry. *Metrologia*, 38(1):25, 2001.

[15] M. Vengalattore, J. M. Higbie, S. R. Leslie, J. Guzman, L. E. Sadler, and D. M. Stamper-Kurn. High-resolution magnetometry with a spinor Bose-Einstein condensate. *Physical Review Letters*, 98:200801, 2007.

[16] C. Jentsch, T. Müller, E. M. Rasel, and W. Ertmer. HYPER: A satellite mission in fundamental physics based on high precision atom interferometry. *General Relativity and Gravitation*, 36(10):2197–2221, 2004.

[17] K.-Y. Chung, S.-W. Chiow, S. Herrmann, S. Chu, and H. Müller. Atom interferometry tests of local Lorentz invariance in gravity and electrodynamics. *Physical Review D*, 80:016002, 2009.

[18] M. Kasevich and S. Chu. Measurement of the gravitational acceleration of an atom with a light-pulse atom interferometer. *Applied Physics B*, 54(5):321–332, 1992.

[19] A. Peters, K. Y. Chung, and S. Chu. Measurement of gravitational acceleration by dropping atoms. *Nature*, 400(6747):849–852, 1999.

[20] M. Kasevich and S. Chu. Atomic interferometry using stimulated Raman transitions. *Physical Review Letters*, 67:181–184, 1991.

[21] S. J. Kim, H. Yu, S. T. Gang, D. Anderson, and J. B. Kim. Controllable asymmetric matter-wave beam splitter and ring potential on an atom chip. *arXiv preprint*, 1506:01013v1, 2015.

[22] D. S. Durfee, Y. K. Shaham, and M. A. Kasevich. Long-term stability of an area-reversible atom-interferometer Sagnac gyroscope. *Physical Review Letters*, 97:240801, 2006.

[23] J. H. T. Burke and C. A. Sackett. Scalable Bose-Einstein-condensate Sagnac interferometer in a linear trap. *Physical Review A*, 80:061603, 2009.

[24] P. L. Halkyard, M. P. A. Jones, and S. A. Gardiner. Rotational response of two-component Bose-Einstein condensates in ring traps. *Physical Review A*, 81:061602, 2010.

[25] G. E. Marti, R. Olf, and D. M. Stamper-Kurn. Collective excitation interferometry with a toroidal Bose-Einstein condensate. *Physical Review A*, 91:013602, 2015.

[26] S. N. Bose. Plancks Gesetz und Lichtquantenhypothese. *Zeitschrift für Physik*, 26:178, 1924.

[27] A. Einstein. Quantentheorie des einatomigen idealen Gases. In *Sitzungsberichte der Preußischen Akademie der Wissenschaften zu Berlin*, volume 22, page 261. 1924.

[28] A. Einstein. Quantentheorie des einatomigen idealen Gases, Zweite Abhandlung. In *Sitzungsberichte der Preußischen Akademie der Wissenschaften zu Berlin*, volume 1, page 3. 1925.

[29] M. H. Anderson, J. R. Ensher, M. R. Matthews, C. E. Wieman, and E. A. Cornell. Observation of Bose-Einstein condensation in a dilute atomic vapor. *Science*, 269(5221):198–201, 1995.

[30] K. B. Davis, M. O. Mewes, M. R. Andrews, N. J. van Druten, D. S. Durfee, D. M. Kurn, et al. Bose-Einstein condensation in a gas of sodium atoms. *Physical Review Letters*, 75:3969–3973, 1995.

[31] D. Comparat, A. Fioretti, G. Stern, E. Dimova, B. L. Tolra, and P. Pillet. Optimized production of large Bose-Einstein condensates. *Physical Review A*, 73:043410, 2006.

[32] C. C. Bradley, C. A. Sackett, J. J. Tollett, and R. G. Hulet. Evidence of Bose-Einstein condensation in an atomic gas with attractive interactions. *Physical Review Letters*, 75:1687–1690, 1995.

[33] M. R. Andrews, C. G. Townsend, H.-J. Miesner, D. S. Durfee, D. M. Kurn, and W. Ketterle. Observation of interference between two Bose condensates. *Science*, 275(5300):637–641, 1997.

[34] Y. Shin, M. Saba, T. A. Pasquini, W. Ketterle, D. E. Pritchard, and A. E. Leanhardt. Atom interferometry with Bose-Einstein condensates in a double-well potential. *Physical Review Letters*, 92:050405, 2004.

[35] T. Schumm, S. Hofferberth, L. M. Andersson, S. Wildermuth, S. Groth, I. Bar-Joseph, et al. Matter-wave interferometry in a double well on an atom chip. *Nature Physics*, 1(1):57–62, 2005.

[36] O. Garcia, B. Deissler, K. J. Hughes, J. M. Reeves, and C. A. Sackett. Bose-Einstein condensate interferometer with macroscopic arm separation. *Physical Review A*, 74:031601, 2006.

[37] S. A. Haine and A. J. Ferris. Surpassing the standard quantum limit in an atom interferometer with four-mode entanglement produced from four-wave mixing. *Physical Review A*, 84:043624, 2011.

[38] S. A. Haine, S. S. Szigeti, M. D. Lang, and C. M. Caves. Heisenberg-limited metrology with information recycling. *Physical Review A*, 91:041802, 2015.

[39] W. Muessel, H. Strobel, D. Linnemann, D. B. Hume, and M. K. Oberthaler. Scalable spin squeezing for quantum-enhanced magnetometry with Bose-Einstein condensates. *Physical Review Letters*, 113:103004, 2014.

[40] V. Ahufinger, M. Lewenstein, and A. Sanpera. *Ultracold atoms in optical lattices: Simulating quantum many-body systems*. Oxford University Press, 2012.

[41] E. J. Meier, F. A. An, and B. Gadway. Atom-optics simulator of lattice transport phenomena. *Physical Review A*, 93:051602, 2016.

[42] K. Sasaki, N. Suzuki, and H. Saito. Bénard–von Kármán vortex street in a Bose-Einstein condensate. *Physical Review Letters*, 104:150404, 2010.

[43] M. T. Reeves, T. P. Billam, B. P. Anderson, and A. S. Bradley. Identifying a superfluid Reynolds number via dynamical similarity. *Physical Review Letters*, 114:155302, 2015.

[44] T. Karpiuk, B. Grémaud, C. Miniatura, and M. Gajda. Superfluid fountain effect in a Bose-Einstein condensate. *Physical Review A*, 86:033619, 2012.

[45] R. Zhang, S. R. Garner, and L. V. Hau. Creation of long-term coherent optical memory via controlled nonlinear interactions in Bose-Einstein condensates. *Physical Review Letters*, 103:233602, 2009.

[46] M. F. Riedel, P. Böhi, Y. Li, T. W. Hänsch, A. Sinatra, and P. Treutlein. Atom-chip-based generation of entanglement for quantum metrology. *Nature*, 464(7292):1170–1173, 2010.

[47] T. Byrnes, K. Wen, and Y. Yamamoto. Macroscopic quantum computation using Bose-Einstein condensates. *Physical Review A*, 85:040306, 2012.

[48] L. Amico, D. Aghamalyan, F. Auksztol, H. Crepaz, R. Dumke, and L. C. Kwek. Superfluid qubit systems with ring shaped optical lattices. *Scientific Reports*, 4:4298, 2014.

[49] P. B. Wigley, P. J. Everitt, A. van den Hengel, J. W. Bastian, M. A. Sooriyabandara, G. D. McDonald, et al. Fast machine-learning online optimization of ultra-cold-atom experiments. *Scientific Reports*, 6:25890, 2016.

[50] R. Wynands and S. Weyers. Atomic fountain clocks. *Metrologia*, 42(3):S64, 2005.

[51] A. Görlitz, T. L. Gustavson, A. E. Leanhardt, R. Löw, A. P. Chikkatur, S. Gupta, et al. Sodium Bose-Einstein condensates in the $F = 2$ state in a large-volume optical trap. *Physical Review Letters*, 90:090401, 2003.

[52] B. T. Seaman, M. Krämer, D. Z. Anderson, and M. J. Holland. Atomtronics: Ultracold-atom analogs of electronic devices. *Physical Review A*, 75:023615, 2007.

[53] M. Gajdacz, T. Opatrnỳ, and K. K. Das. An atomtronics transistor for quantum gates. *arXiv preprint*, 1207:3108, 2012.

[54] Y.-H. Wang, A. Kumar, F. Jendrzejewski, R. M. Wilson, M. Edwards, S. Eckel, et al. Resonant wavepackets and shock waves in an atomtronic SQUID. *New Journal of Physics*, 17(12):125012, 2015.

[55] S. Eckel, J. G. Lee, F. Jendrzejewski, N. Murray, C. W. Clark, C. J. Lobb, et al. Hysteresis in a quantized superfluid 'atomtronic' circuit. *Nature*, 506(7487):200–203, 2014.

[56] A. Kumar, N. Anderson, W. D. Phillips, S. Eckel, G. K. Campbell, and S. Stringari. Minimally destructive, Doppler measurement of a quantized flow in a ring-shaped Bose–Einstein condensate. *New Journal of Physics*, 18(2):025001, 2016.

[57] J. A. Sauer, M. D. Barrett, and M. S. Chapman. Storage ring for neutral atoms. *Physical Review Letters*, 87:270401, 2001.

[58] W. H. Heathcote, E. Nugent, B. T. Sheard, and C. J. Foot. A ring trap for ultracold atoms in an RF-dressed state. *New Journal of Physics*, 10(4):043012, 2008.

[59] A. S. Arnold, C. S. Garvie, and E. Riis. Large magnetic storage ring for Bose-Einstein condensates. *Physical Review A*, 73:041606, 2006.

[60] O. Morizot, Y. Colombe, V. Lorent, H. Perrin, and B. M. Garraway. Ring trap for ultracold atoms. *Physical Review A*, 74:023617, 2006.

[61] S. Wu, W. Rooijakkers, P. Striehl, and M. Prentiss. Bidirectional propagation of cold atoms in a "stadium"-shaped magnetic guide. *Physical Review A*, 70:013409, 2004.

[62] S. Gupta, K. W. Murch, K. L. Moore, T. P. Purdy, and D. M. Stamper-Kurn. Bose-Einstein condensation in a circular waveguide. *Physical Review Letters*, 95:143201, 2005.

[63] C. Ryu, M. F. Andersen, P. Cladé, V. Natarajan, K. Helmerson, and W. D. Phillips. Observation of persistent flow of a Bose-Einstein condensate in a toroidal trap. *Physical Review Letters*, 99:260401, 2007.

[64] A. Ramanathan, K. C. Wright, S. R. Muniz, M. Zelan, W. T. Hill, C. J. Lobb, et al. Superflow in a toroidal Bose-Einstein condensate: An atom circuit with a tunable weak link. *Physical Review Letters*, 106:130401, 2011.

[65] E. M. Wright, J. Arlt, and K. Dholakia. Toroidal optical dipole traps for atomic Bose-Einstein condensates using Laguerre-Gaussian beams. *Physical Review A*, 63:013608, 2000.

[66] S. Thanvanthri, K. T. Kapale, and J. P. Dowling. Arbitrary coherent superpositions of quantized vortices in Bose-Einstein condensates via orbital angular momentum of light. *Physical Review A*, 77:053825, 2008.

[67] S. Beattie, S. Moulder, R. J. Fletcher, and Z. Hadzibabic. Persistent currents in spinor condensates. *Physical Review Letters*, 110:025301, 2013.

[68] F. Jendrzejewski, S. Eckel, N. Murray, C. Lanier, M. Edwards, C. J. Lobb, et al. Resistive flow in a weakly interacting Bose-Einstein condensate. *Physical Review Letters*, 113:045305, 2014.

[69] A. C. Mathey and L. Mathey. Realizing and optimizing an atomtronic SQUID. *New Journal of Physics*, 18(5):055016, 2016.

[70] R. Mathew, A. Kumar, S. Eckel, F. Jendrzejewski, G. K. Campbell, M. Edwards, et al. Self-heterodyne detection of the *in situ* phase of an atomic superconducting quantum interference device. *Physical Review A*, 92:033602, 2015.

[71] C. Ryu, P. W. Blackburn, A. A. Blinova, and M. G. Boshier. Experimental realization of Josephson junctions for an atom SQUID. *Physical Review Letters*, 111:205301, 2013.

[72] S. Eckel, F. Jendrzejewski, A. Kumar, C. J. Lobb, and G. K. Campbell. Interferometric measurement of the current-phase relationship of a superfluid weak link. *Physical Review X*, 4:031052, 2014.

[73] K. Henderson, C. Ryu, C. MacCormick, and M. G. Boshier. Experimental demonstration of painting arbitrary and dynamic potentials for Bose-Einstein condensates. *New Journal of Physics*, 11(4):043030, 2009.

[74] S. K. Schnelle, E. D. van Ooijen, M. J. Davis, N. R. Heckenberg, and H. Rubinsztein-Dunlop. Versatile two-dimensional potentials for ultra-cold atoms. *Optics Express*, 16(3):1405–1412, 2008.

[75] T. A. Bell. Design, construction and characterisation of a versatile, high atom number BEC apparatus, Honours thesis, University of Queensland, 2014.

[76] K. O. Roberts, T. McKellar, J. Fekete, A. Rakonjac, A. B. Deb, and N. Kjærgaard. Steerable optical tweezers for ultracold atom studies. *Optics Letters*, 39(7):2012–2015, 2014.

[77] O. Morsch and M. Oberthaler. Dynamics of Bose-Einstein condensates in optical lattices. *Reviews of Modern Physics*, 78:179–215, 2006.

[78] L. Amico, A. Osterloh, and F. Cataliotti. Quantum many particle systems in ring-shaped optical lattices. *Physical Review Letters*, 95:063201, 2005.

[79] S. Moulder. Persistent currents in Bose-Einstein condensates. Ph.D. thesis, University of Cambridge, 2013.

[80] H. J. Metcalf and P. van der Straten. *Laser cooling and trapping*. Springer, 1999.

[81] R. Grimm, M. Weidemüller, and Y. B. Ovchinnikov. Optical dipole traps for neutral atoms. *Advances in Atomic, Molecular and Optical Physics*, 42:95–170, 2000.

[82] O. Wille. Manipulation of Bose-Einstein condensates in optical dipole potentials. Ph.D. thesis, Technische Universität Darmstadt, 2010.

[83] T. Hänsch and A. Schawlow. Cooling of gases by laser radiation. *Optics Communications*, 13(1):68 – 69, 1975.

[84] W. D. Phillips and H. Metcalf. Laser deceleration of an atomic beam. *Physical Review Letters*, 48:596–599, 1982.

[85] J. P. Gordon and A. Ashkin. Motion of atoms in a radiation trap. *Physical Review A*, 21:1606–1617, 1980.

[86] S. Chu, L. Hollberg, J. E. Bjorkholm, A. Cable, and A. Ashkin. Three-dimensional viscous confinement and cooling of atoms by resonance radiation pressure. *Physical Review Letters*, 55:48–51, 1985.

[87] D. E. Pritchard, E. L. Raab, V. Bagnato, C. E. Wieman, and R. N. Watts. Light Traps Using Spontaneous Forces. *Physical Review Letters*, 57:310–313, 1986.

[88] S. Chu, J. E. Bjorkholm, A. Ashkin, and A. Cable. Experimental observation of optically trapped atoms. *Physical Review Letters*, 57:314–317, 1986.

[89] E. L. Raab, M. Prentiss, A. Cable, S. Chu, and D. E. Pritchard. Trapping of Neutral Sodium Atoms with Radiation Pressure. *Physical Review Letters*, 59:2631–2634, 1987.

[90] C. J. Foot. Laser cooling and trapping of atoms. *Contemporary Physics*, 32(6):369–381, 1991.

[91] J. Dalibard and C. Cohen-Tannoudji. Laser cooling below the Doppler limit by polarization gradients: simple theoretical models. *Journal of the Optical Society of America B*, 6(11):2023–2045, 1989.

[92] D. A. Steck. *Rubidium 87 D-line data.* URL: http://steck.us/alkalidata, 2003.

[93] N. McKay Parry. Design, construction and performance towards a versatile, ^{87}Rb & ^{41}K BEC apparatus, MPhil thesis, University of Queensland, 2015.

[94] J. Schoser, A. Batär, R. Löw, V. Schweikhard, A. Grabowski, Y. B. Ovchinnikov, et al. Intense source of cold Rb atoms from a pure two-dimensional magneto-optical trap. *Physical Review A*, 66:023410, 2002.

[95] W. Petrich, M. H. Anderson, J. R. Ensher, and E. A. Cornell. Stable, tightly confining magnetic trap for evaporative cooling of neutral atoms. *Physical Review Letters*, 74:3352–3355, 1995.

[96] E. Majorana. Atomi orientati in campo magnetico variabile. *Il nuovo cimento*, 9(2):43–50, 1923.

[97] U. Ernst, A. Marte, F. Schreck, J. Schuster, and G. Rempe. Bose-Einstein condensation in a pure Ioffe-Pritchard field configuration. *Europhysics Letters*, 41(1):1, 1998.

[98] D. J. Han, R. H. Wynar, P. Courteille, and D. J. Heinzen. Bose-Einstein condensation of large numbers of atoms in a magnetic time-averaged orbiting potential trap. *Physical Review A*, 57:R4114–R4117, 1998.

[99] M. D. Barrett, J. A. Sauer, and M. S. Chapman. All-optical formation of an atomic Bose-Einstein condensate. *Physical Review Letters*, 87:010404, 2001.

[100] C. S. Adams, H. J. Lee, N. Davidson, M. Kasevich, and S. Chu. Evaporative cooling in a crossed dipole trap. *Physical Review Letters*, 74:3577–3580, 1995.

[101] Y.-J. Lin, A. R. Perry, R. L. Compton, I. B. Spielman, and J. V. Porto. Rapid production of ^{87}Rb Bose-Einstein condensates in a combined magnetic and optical potential. *Physical Review A*, 79:063631, 2009.

[102] D. M. Stamper-Kurn, M. R. Andrews, A. P. Chikkatur, S. Inouye, H.-J. Miesner, J. Stenger, et al. Optical confinement of a Bose-Einstein condensate. *Physical Review Letters*, 80:2027–2030, 1998.

[103] D. M. Stamper-Kurn and M. Ueda. Spinor Bose gases: Symmetries, magnetism, and quantum dynamics. *Reviews of Modern Physics*, 85:1191–1244, 2013.

[104] I. Lesanovsky and W. von Klitzing. Time-averaged adiabatic potentials: Versatile matter-wave guides and atom traps. *Physical Review Letters*, 99:083001, 2007.

[105] E. Tiesinga, A. J. Moerdijk, B. J. Verhaar, and H. T. C. Stoof. Conditions for Bose-Einstein condensation in magnetically trapped atomic cesium. *Physical Review A*, 46:R1167–R1170, 1992.

[106] H. F. Hess. Evaporative cooling of magnetically trapped and compressed spin-polarized hydrogen. *Physical Review B*, 34:3476–3479, 1986.

[107] T. A. Savard, K. M. O'Hara, and J. E. Thomas. Laser-noise-induced heating in far-off resonance optical traps. *Physical Review A*, 56:R1095–R1098, 1997.

[108] N. Poli, R. J. Brecha, G. Roati, and G. Modugno. Cooling atoms in an optical trap by selective parametric excitation. *Physical Review A*, 65:021401, 2002.

[109] W. Muessel, H. Strobel, M. Joos, E. Nicklas, I. Stroescu, J. Tomkovič, et al. Optimized absorption imaging of mesoscopic atomic clouds. *Applied Physics B*, 113(1):69–73, 2013.

[110] W. Ketterle, D. S. Durfee, and D. M. Stamper-Kurn. Making, probing and understanding Bose-Einstein condensates. *arXiv preprint*, cond-mat:9904034v2, 1999.

[111] C. J. Pethick and H. Smith. *Bose-Einstein condensation in dilute gases*. Cambridge University Press, 2nd edition, 2008.

[112] L. Mathey, A. Ramanathan, K. C. Wright, S. R. Muniz, W. D. Phillips, and C. W. Clark. Phase fluctuations in anisotropic Bose-Einstein condensates: From cigars to rings. *Physical Review A*, 82:033607, 2010.

[113] V. Bagnato, D. E. Pritchard, and D. Kleppner. Bose-Einstein condensation in an external potential. *Physical Review A*, 35:4354–4358, 1987.

[114] D. J. Griffiths. *Introduction to Quantum Mechanics*. Pearson Prentice Hall, 2nd edition, 2004.

[115] N. Bogoliubov. On the theory of superfluidity. *Journal of Physics (USSR)*, 11:23, 1947.

[116] M. C. Garrett, T. M. Wright, and M. J. Davis. Condensation and quasicondensation in an elongated three-dimensional Bose gas. *Physical Review A*, 87:063611, 2013.

[117] D. S. Petrov, G. V. Shlyapnikov, and J. T. M. Walraven. Phase-fluctuating 3D Bose-Einstein condensates in elongated traps. *Physical Review Letters*, 87:050404, 2001.

[118] S. Dettmer, D. Hellweg, P. Ryytty, J. J. Arlt, W. Ertmer, K. Sengstock, et al. Observation of phase fluctuations in elongated Bose-Einstein condensates. *Physical Review Letters*, 87:160406, 2001.

[119] S. Richard, F. Gerbier, J. H. Thywissen, M. Hugbart, P. Bouyer, and A. Aspect. Momentum spectroscopy of 1D phase fluctuations in Bose-Einstein condensates. *Physical Review Letters*, 91:010405, 2003.

[120] I. Shvarchuck, C. Buggle, D. S. Petrov, K. Dieckmann, M. Zielonkowski, M. Kemmann, et al. Bose-Einstein condensation into nonequilibrium states studied by condensate focusing. *Physical Review Letters*, 89:270404, 2002.

[121] L. M. Bennie, P. T. Starkey, M. Jasperse, C. J. Billington, R. P. Anderson, and L. D. Turner. A versatile high resolution objective for imaging quantum gases. *Optics Express*, 21(7):9011–9016, 2013.

[122] J. Küber. Dynamics of Bose-Einstein condensates in novel optical potentials. Ph.D. thesis, Technische Universität Darmstadt, 2014.

[123] A. Pritchard. Bose–Einstein condensates in novel optical potentials, probed using Bragg spectroscopy, Honours thesis, University of Queensland, 2016.

[124] G. R. Dennis, J. J. Hope, and M. T. Johnsson. XMDS2: Fast, scalable simulation of coupled stochastic partial differential equations. *Computer Physics Communications*, 184(1):201 – 208, 2013.

[125] E. C. Samson, K. E. Wilson, Z. L. Newman, and B. P. Anderson. Deterministic creation, pinning, and manipulation of quantized vortices in a Bose-Einstein condensate. *Physical Review A*, 93:023603, 2016.

[126] D. Yan, R. Carretero-González, D. J. Frantzeskakis, P. G. Kevrekidis, N. P. Proukakis, and D. Spirn. Exploring vortex dynamics in the presence of dissipation: Analytical and numerical results. *Physical Review A*, 89:043613, 2014.

[127] S. P. Cockburn, H. E. Nistazakis, T. P. Horikis, P. G. Kevrekidis, N. P. Proukakis, and D. J. Frantzeskakis. Fluctuating and dissipative dynamics of dark solitons in quasicondensates. *Physical Review A*, 84:043640, 2011.

[128] A. S. Bradley, C. W. Gardiner, and M. J. Davis. Bose-Einstein condensation from a rotating thermal cloud: Vortex nucleation and lattice formation. *Physical Review A*, 77:033616, 2008.

[129] D. Hellweg, L. Cacciapuoti, M. Kottke, T. Schulte, K. Sengstock, W. Ertmer, et al. Measurement of the spatial correlation function of phase fluctuating Bose-Einstein condensates. *Physical Review Letters*, 91:010406, 2003.

[130] L. A. Toikka. Self-interference of a toroidal Bose–Einstein condensate. *New Journal of Physics*, 16(4):043011, 2014.

[131] Hugbart, M., Retter, J. A., Gerbier, F., Varón, A. F., Richard, S., Thywissen, J. H., et al. Coherence length of an elongated condensate. *Eur Phys J D*, 35(1):155–163, 2005.

[132] A. L. Gaunt, T. F. Schmidutz, I. Gotlibovych, R. P. Smith, and Z. Hadzibabic. Bose-Einstein condensation of atoms in a uniform potential. *Physical Review Letters*, 110:200406, 2013.

[133] T.-L. Ho. Spinor Bose condensates in optical traps. *Physical Review Letters*, 81:742–745, 1998.

Appendix A

^{87}Rb line data

The data presented here are collated from [92].

Table A.1: Rubidium 87 atomic properties

Atomic mass	m_{Rb}	$(1.443\,160\,648 \pm 0.000\,000\,072) \times 10^{-25}$ kg
Nuclear spin	I	3/2
Vapour pressure at 25 °C	P_v	$(3.92 \pm 0.20) \times 10^{-7}$ torr
s-wave scattering length	a_s	$(110 \pm 4)\ a_B$ [133]

Table A.2: Rubidium 87 D1 transition properties

Vacuum wavelength	λ_1	$(794.978\,851\,156 \pm 0.000\,000\,023)$ nm
Transition frequency	ω_1	$2\pi \times 377.107463380(11)$ THz
Natural linewidth (FWHM)	Γ_1	$2\pi \times 5.7500(56)$ MHz
Recoil temperature	T_{recoil}	348.66 nK

Table A.3: Rubidium 87 D2 transition properties

Vacuum wavelength	λ_2	$(780.241\,209\,686 \pm 0.000\,000\,013)$ nm
Transition frequency	ω_2	$2\pi \times 384.2304844685(62)$ THz
Natural linewidth (FWHM)	Γ_2	$2\pi \times 6.0666(18)$ MHz
Doppler temperature	T_{Doppler}	145.57 μK
Recoil temperature	T_{recoil}	361.96 nK
Saturation intensity ($F = 2 \rightarrow F' = 3$)	I_{sat}	$(3.577\,13 \pm 0.000\,74)$ mW . cm^{-2}

Appendix B

PI intensity stabilisation

The following circuit is used for locking the intensities of each of our $1064\,$nm beams. Switches allow either manual or external control, at either fixed output, or locked levels. The reference locking signal is connected across ‘EREF’, and the sampling photodiode is connected to ‘PD IN’. The signal across ‘OUT’ is amplified, and drives the AOMs from which each beam is derived. Three separate instances of this circuit are required, one for each of the beams.

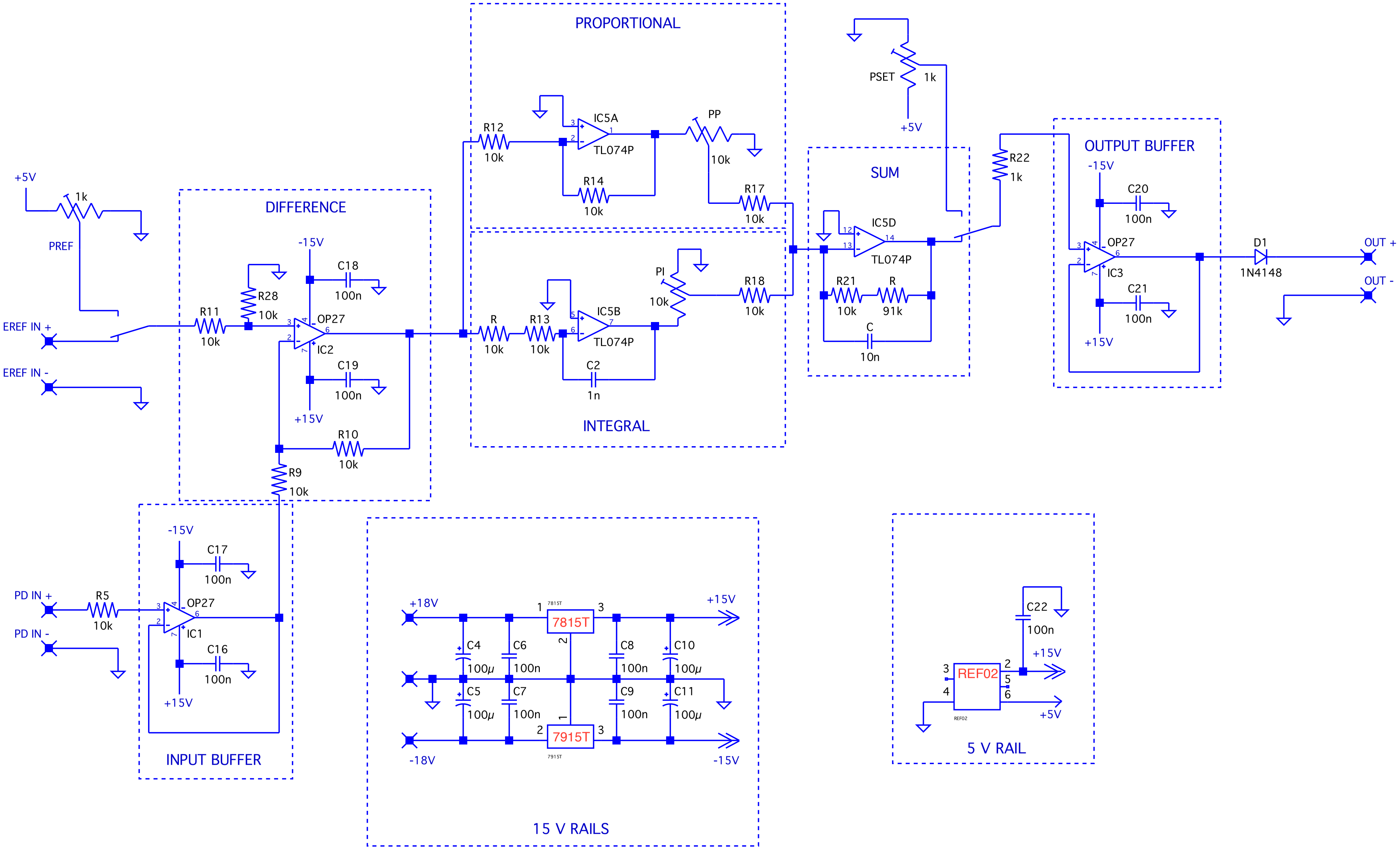
PROPORTIONAL
INTEGRAL
DIFFERENCE
SUM
OUTPUT BUFFER
INPUT BUFFER
15 V RAILS
5 V RAIL
+5V
1k
PREF
EREF IN +
EREF IN -
PD IN +
PD IN -
R5
10k
R11
10k
R28
10k
R9
10k
R10
10k
-15V
+15V
C18
100n
C19
100n
OP27
IC2
C17
100n
C16
100n
IC1
R12
10k
IC5A
TL074P
R14
10k
PP
10k
R17
10k
R
10k
R13
10k
IC5B
TL074P
C2
1n
PI
10k
R18
10k
PSET
1k
IC5D
TL074P
R21
10k
R
91k
C
10n
R22
1k
C20
100n
C21
100n
IC3
D1
1N4148
OUT +
OUT -
+18V
-18V
7815T
7915T
C4
100µ
C5
100µ
C6
100n
C7
100n
C8
100n
C9
100n
C10
100µ
C11
100µ
C22
100n
REF02